

**EVALUATION OF CR-COATED ZR-ALLOY CLADDINGS DURING A  
LOSS OF COOLANT ACCIDENT SCENARIO IN LIGHT WATER  
REACTORS**

by

Tera Benda

A thesis submitted in partial fulfillment of  
the requirements for the degree of

Master of Science  
(Nuclear Engineering)

at the

UNIVERSITY OF WISCONSIN – MADISON

2025

## **Acknowledgements**

Thank you to Kumar Sridharan and Dr. Woo Hyun Jung for your guidance on this project. It means the world that you took the time to help me grow as a scientist and a person.

Thank you to my partner, Griffin, for your support through every late night, every breakthrough, and all the areas in between.

Thank you to Dr. Frank Pfefferkorn and Dr. Hwasung Yeom for standing in my thesis defense committee.

Thank you to my colleagues in the Nuclear and Applied Materials Research Group for their help with this project. Thank you to Nicolas Fox, Thomas Demo, and Cole Dunbar for your support through all stages of my degree. Thank you to Evan Willing, Dongil Shim, and Carson Lukas for your good vibes and fun times.

A special thank you to transgender scientists across all research fields. From rocket science to microbiology, nuclear engineering to meteorology, you've carved a community in the face of adversity. Without your support and inspiration, this would never have been possible. I dedicate my work and the work in this thesis to you, and to those who perished on the climb.

The funding for this research was provided mainly by the U.S. Department of Energy Award Number DE-NE0009139. In addition, I also gratefully acknowledge the support provided by the University of Wisconsin, Madison's Grainger Professorship (for Prof. Kumar Sridharan) grant number GF000022364.

I am also grateful for the use of instrumentation and assistance from the UW-Madison Wisconsin Centers for Nanoscale Technology, partially supported by the National Science Foundation through the University of Wisconsin Materials Research Science and Engineering Center (DMR-1720415).

## Abstract

Zirconium-alloys (Zr-alloys) have been used successfully as the materials for fuel cladding (tubes that contain the uranium-dioxide pellets) in light water reactors (LWR) on account of their good hydrothermal corrosion resistance and strength, and high neutron transparency. While Zr-alloys have performed well under normal operating conditions, loss of coolant accidents (LOCA) where temperatures can exceed 1000 °C can lead to profuse oxidation of the cladding in reaction with steam. The oxidation reaction can consume a significant fraction of the cladding wall thickness and generate hydrogen. A near-term solution to address this challenge is to coat the outer surface of the Zr-alloy cladding with an oxidation-resistant material such as chromium (Cr) that can provide additional coping time in the event of a LOCA. While there are numerous avenues for research on Cr-coated Zr-alloy accident tolerant fuel (ATF) cladding, this study focuses on two aspects: post-quench ductility and the ballooning and burst behavior of cladding.

Two Cr-coating deposition methods are used in this research: cold-spray (CS) deposition and physical vapor deposition (PVD). In the cold spray process, powder particles of the coating material are propelled at supersonic velocities on to the surface of a substrate where upon impact they plastically deform to form a coating. CS deposition was performed using the 4000-30 KINETIK commercial cold spray system at the University of Wisconsin-Madison (UW), using two different carrier gases, helium (CS-He) and nitrogen (CS-N<sub>2</sub>). Helium imparts higher particle velocities and greater plastic deformation during impact. PVD process involves deposition of atoms of the coating material sputtered from a target using energetic argon ions. An advanced version of PVD, HiPIMS (High Power Impulse Magnetron Sputtering) which provides for superior coating microstructure and greater interfacial adhesion, was used. The PVD coating was performed in collaboration with an external company.

Reflood tests were performed in a specialized single rod test facility designed and built at the UW. Here, a 16" cladding section was heated to temperatures in the range of 600 °C to 1200 °C with a thermal radiation furnace followed by flowing pre-heated RO (reverse osmosis) water through a quartz tube and around the cladding. Following the tests, ring-shaped samples were sectioned from the cladding and subjected to ring compression tests (RCT), where load-displacement plots are also generated as the ring sample is vertically deformed in the radial direction to maximum displacement of 2mm. Cross-sectional scanning electron microscopy (SEM) in conjunction with energy dispersive spectroscopy (EDS) was performed after the reflood tests to examine changes in the microstructure, thickness of stoichiometric outer oxide layer, and diffusion depth of oxygen into the Zr-alloy cladding which can embrittle the cladding. Microhardness tests were also performed along the cross-section of the entire wall thickness and were found to replicate the oxygen diffusion profile. The beneficial effect of Cr coating became evident at higher reflood test temperatures. At 1200°C, the CS-He Cr coating showed a significantly thinner oxide layer thickness, and dramatically reduced oxygen ingress into the cladding. This resulted in better post-quench ductility of CS Cr-coated cladding. The presence of the strongly

adhered cold spray Cr-coating also mechanically reinforced cladding section as evidenced by the higher maximum load for untested claddings during RCT compared to the uncoated Zr-alloy. PVD Cr-coated Zr-alloy mitigated oxygen diffusion into the cladding but to a lesser extent than the cold spray Cr coating, due to diffusion likely having occurred along the intercolumnar boundaries of the PVD Cr coating. Similarly, the level of improvement in mechanical reinforcement provided by the PVD Cr coating was notably lower than that provided by the cold spray Cr coating.

Cladding ballooning and burst tests were performed at initial internal pressures of 6, 8, and 10 MPa by introducing argon gas into the cladding. Argon gas was flown along the outer surface of the cladding to minimize oxidation during tests. All Cr-coated claddings exhibited an increase in burst temperature relative to uncoated Zr-alloy, with CS (He) providing for the highest burst temperature, but a relatively brittle coating failure. Burst dimensions between each coating type largely varied with no discernable pattern. CS (N<sub>2</sub>) exhibited a repeatable, anomalous reduction in burst size at 8 MPa which could be a result of micro-fracturing along the interparticle boundaries which relieved stress. Post-test characterization of ruptured cladding also involved image analysis to measure the burst area dimensions and to measure the diametric strain profile axially, and to measure the post-test wall thickness of the ruptured cross-section. While uncoated and PVD Cr-coated cladding experienced plastic deformation along the entire axial length of the cladding similarly, CS (He) and CS (N<sub>2</sub>) constrained the Zr-alloy substrate with CS (He) constraining all deformation to only within 4 cm of the burst site. The presence of a Cr-coating mitigates the severity of oxygen embrittlement, ballooning, and burst size compared to uncoated Zr-alloy.

## Contents

Acknowledgements.....	i
Abstract .....	ii
List of Figures.....	vi
List of Tables.....	ix
List of Acronyms .....	x
1 Introduction and Motivation .....	1
1.1 Light Water Reactor (LWR).....	1
1.2 Zr-alloy Fuel Cladding.....	3
1.3 Fuel Burnup.....	7
1.4 Accident Tolerant Fuel Concepts.....	9
1.5 Fuel Fragmentation, Relocation, and Dispersal (FFRD).....	12
1.6 Ballooning and Burst Behavior of Cladding.....	15
1.7 Objective .....	17
2 Experimental Methodology .....	19
2.1 Reflood Testing to Simulate LOCA .....	19
2.1.1 Reflood Test Facility .....	19
2.1.2 Sample Preparation.....	20
2.1.3 Cold spray Cr-coating deposition.....	21
2.1.4 PVD Cr-coating deposition .....	23
2.1.5 Single Rod Reflood Test Matrix .....	24
2.1.6 Ring Compression Testing (RCT).....	25
2.2 Characterization of Post-quench Ductility .....	28
2.2.1 Micro Indentation Testing .....	28
2.2.2 Scanning Electron Microscopy – Energy Dispersive Spectroscopy (SEM-EDS).....	30
2.3 Single Rod Burst Test .....	32
2.3.1 Single Rod Burst Test Facility.....	32

2.3.2	Cladding Tube Preparation .....	35
2.3.3	Pre-test Assembly .....	36
2.3.4	Surrogate Fuel Pellet.....	37
2.3.5	Temperature and Pressure Measurement .....	37
2.3.6	Test Procedure.....	40
2.3.7	Test Matrix .....	43
3	Results and Discussion.....	45
3.1	Post-quench Ductility.....	45
3.1.1	Ring Compression Testing .....	45
3.2	Burst Behavior of the Cr-coated Zr-alloy Cladding .....	56
3.2.1	Burst Temperature and Pressure .....	56
3.2.2	Burst Temperature.....	61
3.3	Cr-coating Deformation and Rupture Behavior .....	64
3.3.1	Burst Opening and Ballooning Behavior .....	67
3.3.2	Wall Thickness Measurement after Burst Tests.....	69
3.3.3	Benefits of Cr-coating in the Context of Ballooning and Burst Behavior.....	71
4	Concluding Remarks.....	73
	References.....	77

## List of Figures

Figure 1. A schematic diagram of a pressurized water reactor (PWR) two-loop system [1].....	2
Figure 2. A schematic diagram of a boiling water reactor (BWR) one loop system [1].....	2
Figure 3. Comparisons of evaluated achievable burnup and macroscopic thermal absorption cross sections for current and proposed cladding materials [3]. .....	4
Figure 4. Cross-sectional SEM images showing (a) circumferential and (b) radial hydride structures in Zr-alloy [5]. .....	7
Figure 5. U.S Energy Information Administration annual average discharge bumup data [14].....	8
Figure 6. Cross-sectional SEM images showing the formation of spinel and aluminum oxide of FeCrAl cladding [18]. .....	10
Figure 7. Cross-sectional SEM image of a Cr-coating deposited onto a Zr-alloy substrate [23].....	11
Figure 8. Simulated LOCA cladding rupture by Kane et al [22]. (a) Zry-4 cladding (b) Cr-coated Zry-4 (c) FeCrAl (d) SiC ceramic matrix composite (CMC).....	12
Figure 9. Post-test characterization for fuel claddings at increasing burnups performed at the Halden reactor [24].....	13
Figure 10. Mass fraction of fuel fragments smaller than 1 mm and 2 mm in high fuel burnup level [26]..	15
Figure 11. Ballooning and burst openings of a Zr-alloy subjected to two heating rates, 14 °C/s and 28 °C/s at various initial internal pressures of the cladding [29]. .....	16
Figure 12. Schematic illustration of (a) single rod reflood facility, (b) configuration of surrogate pellet and thermocouples(indicated as TC 1, TC 2, TC 3, TC 4, TC 5) inside the cladding, and (c) axial installation of thermocouples [31]. .....	20
Figure 13. Pre-test and pre-coating surface roughness of an uncoated Zr-alloy cladding.....	21
Figure 14. Photographs of (a) cold spray coating system during the Cr coating process and (b) example of Zr-alloy samples before coating, after the coating deposition but before the polishing, and after the polishing. ....	23
Figure 15. Material characterization and mechanical testing of post-quench uncoated and Cr-coated Zr-alloy cladding. Shown on the left are the reflood test temperatures. ....	25
Figure 16. Drawing showing the sectioning for cross-sectional imaging and RCT of Zr-alloy tubes after the reflood tests. Sections 1-4 are numbered for. ....	26
Figure 17. Ring compression testing of post-quench Zr-alloy cladding. (a) MTS Criterion Model 42 Electromechanical Universal Test System. (b) photo of ring compression test being performed for an as-received, uncoated Zr-alloy cladding section.....	27
Figure 18. Pre-test and post-test shape of ring compression samples. (a) untested, uncoated Zr-alloy pre-RCT (circular), (b) untested, uncoated Zr-alloy post-RCT (elliptical). ....	27

Figure 19. RCT load-displacement plot of an uncoated Zr-alloy after post-quench test from 600 °C sample. An example of offset strain calculation is shown.....	28
Figure 20. Buehler Micromet II Digital Microhardness Tester used in this study. ....	30
Figure 21. Optical microscopy images showing indents from microhardness tests of an untested, uncoated Zr-alloy sample with five micro-indents along the cross-sectional depth of the cladding wall.....	30
Figure 22. Cross-sectional SEM image showing the line trace (yellow lines) for EDS line-scan compositional analysis performed across the cladding wall thickness for the 1200 °C post-quench uncoated Zr-alloy sample. Line-scan compositional analysis was performed from the top of the oxide layer to the inner diameter of the cladding.....	31
Figure 23. Single rod burst test facility used in this research. ....	33
Figure 24. Schematic illustration of the single rod burst test facility showing the positioning of the cladding, quartz tube, furnaces, and argon gas supply. ....	34
Figure 25. Cladding mount apparatus (a) spacer anchor that fits the bottom spacer of the cladding, (b) bottom spacer, (c) top spacer above the cladding that attaches to the top end cap, and (d) top end cap with apertures for gas line connections.....	35
Figure 26. Photograph showing fixturing used the ballooning and burst tests for an uncoated Zr-alloy cladding tube (a) attached to two 316 stainless steel bulkhead unions with flow spacers on each end and (b) the end cap connecting the mounted cladding to gas lines and a thermocouple. ....	36
Figure 27. An uncoated Zr-alloy cladding next to the spacers and alumina pellets that are loaded into the cladding to conduct ballooning and burst tests. ....	37
Figure 28. Position of the thermocouple inside the single rod test facility, (a) diagram of the cladding mounted inside the test facility and (b) photograph of the relative placement of the thermocouple without cladding.....	38
Figure 29. Pressure transducer in the test facility along with other neighboring components.....	39
Figure 30. Images of cladding spacers and spacer mounts. (a) anchor for the bottom spacer (b) bottom spacer fitted to bulkhead (c) top spacer with end cap (d) top end cap. ....	41
Figure 31. Potential leak points on the cladding assembly that were tested with Snoop fluid. ....	42
Figure 32. Intensity of cracking behavior of 1200 °C post-quench PVD Cr-coated Zr-alloy. (a) Section 3, thin closed hairline fracture across entire wall (b) section 2, open fracture (c) section 4, split fracture.....	45
Figure 33. Cross-sectional SEM image of a post-RCT through-wall fracture in an uncoated Zr-alloy cladding that was quenched during the reflow test from a temperature of 1200 °C. ....	46
Figure 34. Load-displacement curves for (a) uncoated (b) CS (He) Cr-coated and (c) PVD Cr-coated ZIRLO. Each plot contains five loading curves for temperatures between 600-1200 °C.....	49
Figure 35. Cross-sectional optical microscopy image of an uncoated ZIRLO cladding sample quenched at 1200 °C. A thick stoichiometric Zr oxide layer is observed.....	49

Figure 36. Cross-sectional SEM images and EDS line scans of samples after quenching from reflow tests at 1200 °C (a) uncoated Zr-alloy, (b) CS Cr-coated Zr-alloy, and (c) PVD Cr coated Zr-alloy. ....	51
Figure 37. Load-displacement curve of uncoated and Cr-coated ZIRLO quenched in the reflow tests from a temperature of 1200 °C. ....	52
Figure 38. Vickers microhardness measurements across the cross-section of the cladding wall thickness: (a) uncoated, (b) Cr cold spray coated, (c) Cr PVD coated, (d) compilation of data for the 1200°C quench samples for the three types of cladding samples. ....	56
Figure 39. Pressure and temperature curves of an 8 MPa uncoated Zr-alloy burst test. ....	57
Figure 40. Rupture temperature as a function of engineering hoop stress for Zircaloy cladding taken from various sources: Oak Ridge National Laboratory, Battelle Columbus Laboratories, Kernforschungszentrum Karlsruhe (Germany), and the Japan Atomic Energy Research Institute [6].....	59
Figure 41. Burst temperatures of all four cladding types: uncoated Zr-alloy, CS (He), CS (N <sub>2</sub> ), and PVD Cr coated Zr-alloy. The burst pressures of each cladding were converted into hoop engineering stress. ....	61
Figure 42. Burst temperature of uncoated and Cr-coated cladding as a function of the engineering hoop stress. ....	62
Figure 43. Cross sectional SEM of (a) CS (He) and (b) PVD Cr-coated Zr-alloy cladding.....	64
Figure 44. Cladding ruptured with an initial pressure of 6, 8, and 10 MPa of Cr-coated and uncoated Zr-alloy. ....	65
Figure 45. SEM plan-view images of (a) uncoated (b) PVD (c) CS (He) (d) CS (N <sub>2</sub> ) .....	66
Figure 46. Method used to calculate the burst length, width, and area using ImageJ.....	67
Figure 47. Burst area of uncoated and Cr-coated Zr-alloy. ....	68
Figure 48. Diametric strain measurements from the 8MPa cladding rupture to the end of the cladding. Strain measurements started at the maximal strain directly in the center of the burst.....	69
Figure 49. Optical microscopy of a cross section of an uncoated Zr-alloy sample tested at 8 MPa.....	70
Figure 50. Optical microscopy of a cross section of a CS (He) Cr-coated Zr-alloy sample tested at 8 MPa. ....	71

**List of Tables**

Table 1. Nominal composition of nuclear-grade Zr-alloys (in weight %) [8] [9]. .....	5
Table 2. Reflood testing matrix. (*: Number of reproducibility tests).....	24
Table 3. Test matrix of the single rod (7.6” length) burst test facility for burst testing of Zr-alloy. * denotes a reproducibility test. ....	43
Table 4. Measured burst temperature and engineering hoop stress of the four types of claddings tested: uncoated, CS (He), CS (N <sub>2</sub> ), and PVD Cr-coated Zr-alloy. ....	62

## **List of Acronyms**

ATF – Accident Tolerant Fuel  
BDDBA – Beyond Design Basis Accident  
BWR – Boiling Water Reactor  
CS – Cold Spray  
DBA – Design Basis Accident  
DI: Deionized  
ECCS: Emergency Core Coolant System  
EDS – Energy Dispersive Spectroscopy  
FFRD – Fuel Fragmentation, Relocation, and Dispersal  
HBS: High Burnup Structure  
HiPIMS – High Power Impulse Magnetron Sputtering  
LOCA – Loss of Coolant Accident  
LWR – Light Water Reactor  
NRC – Nuclear Regulatory Commission  
PVD – Physical Vapor Deposition  
PWR – Pressurized Water Reactor  
RCT – Ring Compression Testing  
RO – Reverse Osmosis  
RTT – Ring Tensile Testing  
SEM – Scanning Electron Microscopy

# 1 Introduction and Motivation

## 1.1 Light Water Reactor (LWR)

Currently most of the civilian nuclear energy world-wide comes from light water reactors (LWRs). In the United States, 20% of civilian energy is generated by LWRs. The development of commercial nuclear reactors in the 1950s and 1960s provided the world with a major source of baseload, clean, and affordable energy. A rapid nuclear industrialization soon followed in the 1970s and 1980s as major powers around the world (the US, Russia, China, and European nations) began building their own fleet of nuclear power plants. Currently, the energy capacity produced globally by nuclear power plants is 376 GWe with US producing 110 GWe [1]. Pressurized Water Reactor (PWR) and Boiling Water Reactor (BWR) comprise the majority of global nuclear power production.

PWRs typically utilize a two-loop coolant system. The primary loop forces the flow of light water coolant through the vertical fuel assemblies in the core, where it is heated by the fission of nuclear fuel (typically  $\text{UO}_2$ ). This water is pressurized to approximately 15 MPa [1] and reaches temperatures higher than 300 °C. Heated water is circulated into a heat exchanger to transfer the heat to a secondary water coolant loop where the water is turned into steam to spin turbines, generating electricity. The two-loop design of the PWR ensures that the water in contact with the core is contained away from the external power generating turbines. A schematic illustration of typical PWR two-loop system is shown in Figure 1.

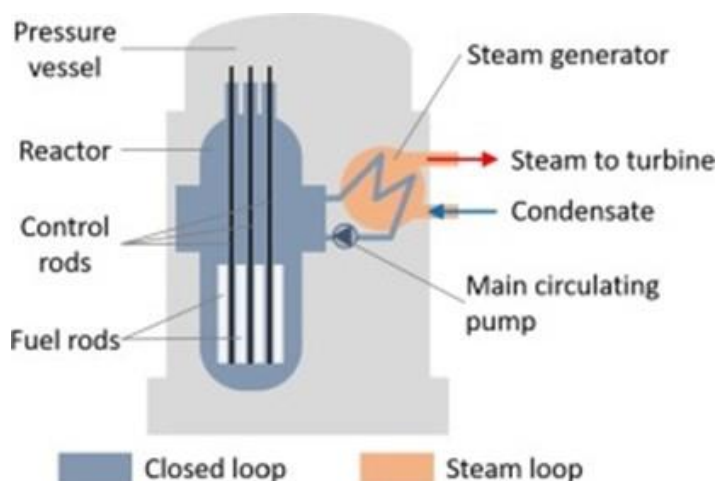


Figure 1. A schematic diagram of a pressurized water reactor (PWR) two-loop system [1].

BWRs operate with the same fuel and coolant as PWRs but differ in heat transfer mechanism at the core. Unlike PWRs which have a two-loop system, BWRs operate with a single coolant loop. Water in the core is not as pressurized as PWRs and heats to a saturation temperature boiling to steam. The two-phase flow of liquid water and steam is separated at the top of the vessel and sent to turbines before circulating back to the bottom of the vessel as condensed water. Figure 2 shows a schematic illustration of the BWR. BWRs comprise a much smaller portion of the global nuclear power supply and PWRs have been adopted as a more widely used means of power generation [1].

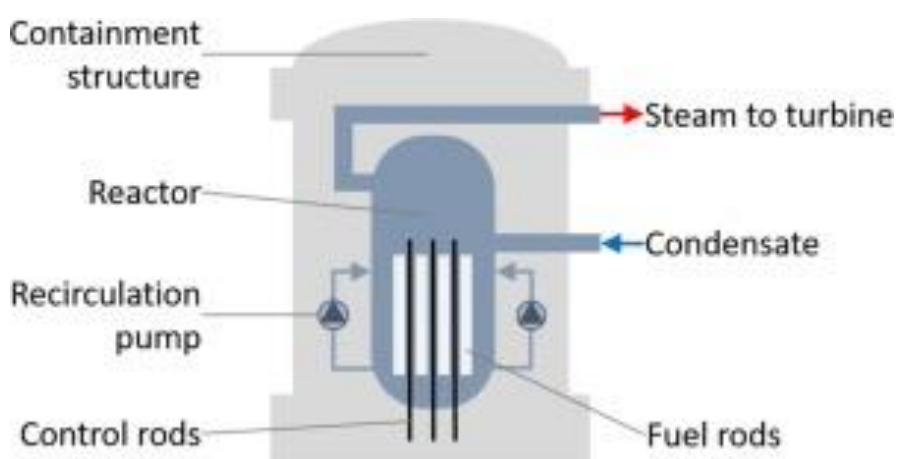


Figure 2. A schematic diagram of a boiling water reactor (BWR) one loop system [1].

## 1.2 Zr-alloy Fuel Cladding

The most critical structural component in the LWR is the fuel cladding, which is a protective tube containing the  $\text{UO}_2$  fuel pellets. There are 200-300 cladding tubes in a fuel assembly and ~200 fuel assemblies in the reactor core. During normal operation, the fuel cladding is subjected to high temperature and high-pressure water coolant, high radiation flux leading to radiation damage effects, hydriding effects leading to embrittlement, and fission gas buildup. To withstand these conditions, fuel cladding material must have: a low neutron cross section, a high allowable maximum service temperature, good creep resistance, and resistance to irradiation damage effects. In addition, they should have good heat transfer properties and must be a chemically compatible material with the fuel, coolant, and moderator [2]. However, no single material fulfills all these requirements. Thus, an alloy must be chosen with the best possible corrosion, irradiation damage resistance, and creep strength while minimizing its limitations. Stainless steel was used as cladding material in the very early LWRs, but for over the last five decades, Zr-alloys have been used as cladding material on account of their high neutron transparency, corrosion resistance, and good creep performance.

Neutronic absorption of the cladding material is critical to neutron economy and hence the economics of the reactor. Neutron absorption is determined by a materials cross section in the energy range of neutron emission. Low neutron absorption will allow for more neutrons to reach the uranium fuel, leading to higher reactivity. The alloying elements in the Zr-alloy will have different absorption cross sections, and even small elemental additions can change neutron absorption behavior. Neutron absorption leads to the creation of various defects within the alloy that degrade its strength, ductility, corrosion resistance, and can lead to irradiation induced creep and dimensional growth. Figure 3 shows the thermal absorption cross-section of multiple alloys and alloying elements at specific burnup levels [3]. As mentioned earlier, the major reason for selecting Zr-alloy as cladding material for PWRs is its low thermal neutron absorption cross section compared to Fe and Ni-based alloys.

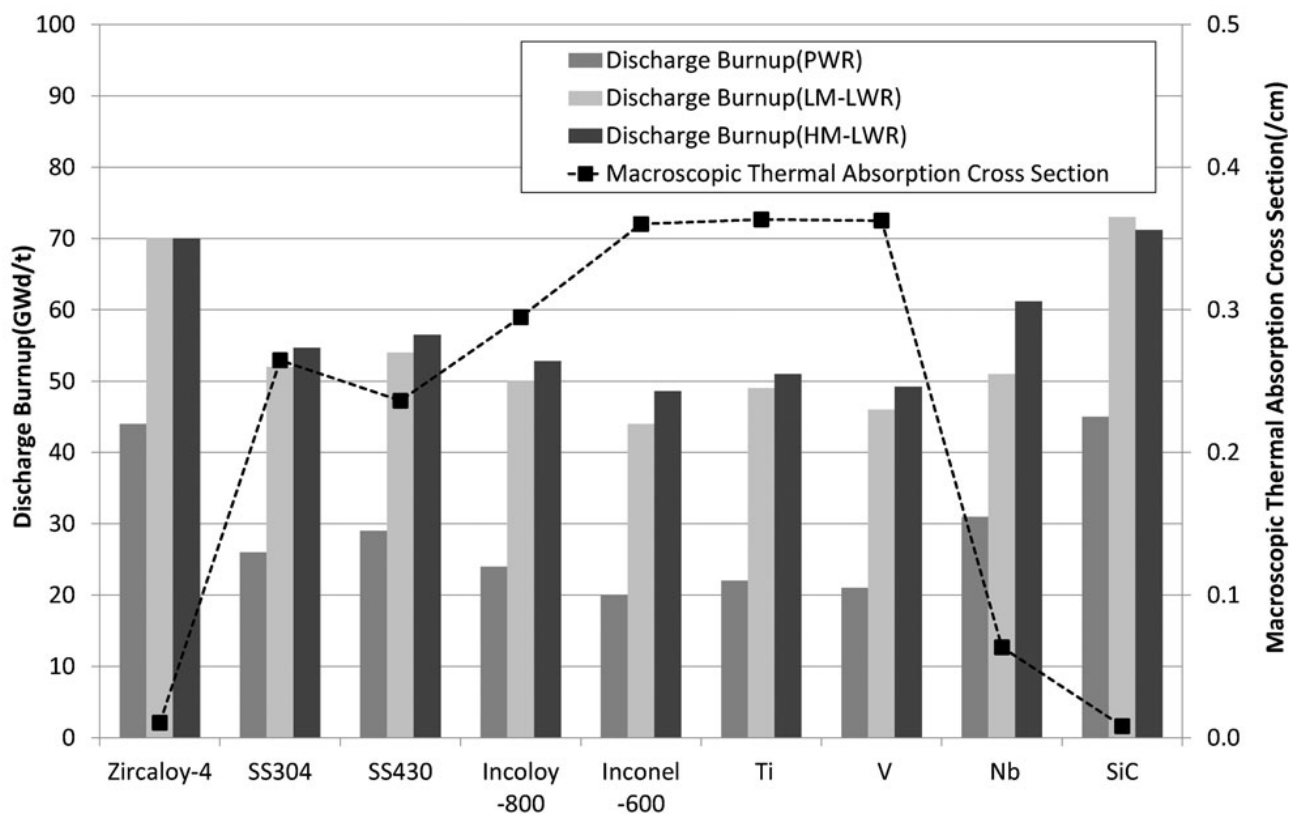


Figure 3. Comparisons of evaluated achievable burnup and macroscopic thermal absorption cross sections for current and proposed cladding materials [3].

In addition to neutron absorption, radiation damage in cladding metal can lead to microstructural changes that can in turn lead to embrittlement, radiation-induced segregation (RIS), creep, and void swelling. While Zr-alloy is mostly transparent to thermal neutrons, it is still susceptible to radiation damage. No material is immune to radiation damage, and designing an alloy to mitigate radiation damage requires considerable research.

Corrosion of Zr-alloy in the hydrothermal conditions of water coolant (with added chemicals) is an important degradation mechanism. This corrosion occurs in the form of oxidation which consumes the Zr-alloy and reduces the effective wall thickness of the cladding, which already is quite thin (0.5mm to 0.7mm). This oxidation process can lead to production of hydrogen which can diffuse into the cladding and cause embrittlement due to the formation of brittle Zr-hydride phases. In the corrosion-oxidation process, oxygen diffuses into the Zr-alloy interstitially forming a solid solution of oxygen in Zr lattice.

After the oxygen concentration of ~4 wt% [4] is reached, a stoichiometric oxide layer begins to form at the environment/Zr-alloy interface. Initially, the oxide layer is protective and mitigates further diffusion of oxygen into Zr-alloy cladding [5]. Oxide layer growth slows as the layer thickens over time. ZrO<sub>2</sub> forms in different morphologies depending on the thickness of the oxide. Close to the oxide-metal interface the oxide layer is dense, while further oxide growth leads to a transition into a porous layer that may spall off at thicknesses exceeding ~ 50 μm [6]. There are several environmental factors that contribute to oxide layer growth over time such as temperature, water chemistry, and the nominal composition of the Zr-alloy [7].

The first application of zirconium in a nuclear reactor was in the Mark I PWR prototype that led to the Mark II PWR that powered the world's first nuclear submarine, the Nautilus [8]. Spatial constraints in the Nautilus required a compact, pressurized vessel design with long work-lifetime structural materials. While stainless steels and aluminum were considered as fuel cladding, a pure Zr metal was selected for its low neutron capture cross-section and ideal corrosion resistance at the PWR nominal operating temperature (~300 °C) and water chemistries. The high corrosion resistance of Zr stems from its ability to form a protective passive oxide layer on the surface over a wide pH range in hydrothermal environments. To further improve corrosion behavior, elements such as tin, tantalum, niobium, iron, and chromium have been investigated as potential alloying elements [8]. The first Zr-alloys in use in reactors were called Zircaloy, and later iterations would further adjust the alloying element concentration to optimize corrosion resistance and creep strength while not affecting Zr's excellent neutronics characteristics. The two popular Zr-alloys used in modern BWRs and PWRs were Zircaloy-2 and Zircaloy-4, respectively [6]. More advanced Zr-alloys such as ZIRLO® and M-5® are also currently in use in PWRs. Table 1 shows the composition of Zircaloy-2, Zircaloy-4, and ZIRLO alloys as examples of commercial Zr-alloys.

Table 1. Nominal composition of nuclear-grade Zr-alloys (in weight %) [8] [9].

<b>Alloy</b>	<b>Sn</b>	<b>Fe</b>	<b>Cr</b>	<b>Ni</b>	<b>Nb</b>	<b>Zr</b>
Zircaloy - 2	1.5	0.12	0.10	0.05	-	balance

Zircaloy - 4	1.5	0.22	0.1	-	-	balance
ZIRLO	1.0	0.1	-	-	1.0	balance

Zr-alloy is not without its drawbacks. In the aqueous environment of a reactor, the Zr-alloys can react with the environment to produce hydrogen ions, as shown in Eq. 1.



Hydrogen can either diffuse into the Zr-metal or combine to form hydrogen gas. Zr-metal has a low solubility for H and therefore it will precipitate out a zirconium-hydride phase when that solubility limit is reached [6]. The above reaction is detrimental for three reasons: (i) it is an exothermic reaction that can release significant heat especially during a LOCA, (ii) it can lead to the formation of zirconium-hydride which embrittles the Zr alloys, and (iii) the formation of ZrO<sub>2</sub> leads to consumption of Zr metal, leading to a reduction in wall thickness. Figure 4 shows the formation of zirconium-hydride phase in the cladding. The hydride phase originally forms circumferentially but under irradiation and stress can reorient themselves in the radial direction, making them conducive to cracking under hoop stress. Under normal operating conditions, the formation of the zirconium-hydride phase can be a limiting factor in the burnup levels of fuel that can be reached.

In a LOCA scenario, the increase in heat in the reactor from oxidation can lead to dangerous hydrogen gas buildup and the embrittled cladding can fracture leading to fuel dispersal into the environment. In 2011, Japan's Fukushima Daiichi nuclear power plant experienced a loss of coolant accident caused by an earthquake and the ensuing tsunami. Without water coolant, the Zr-alloy fuel cladding began rapidly heating and oxidizing in the steam environment. The subsequent buildup of hydrogen gas eventually led to hydrogen explosions in reactors 1, 3, and 4 [10]. While Zr-alloys are some of the best currently available fuel cladding materials, they require more tolerance under accident conditions to ensure safety in currently operating reactors.

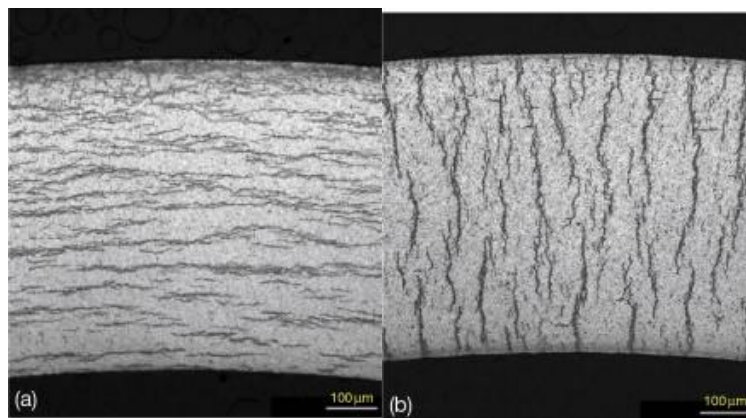


Figure 4. Cross-sectional SEM images showing (a) circumferential and (b) radial hydride structures in Zr-alloy [5].

### 1.3 Fuel Burnup

Nuclear fuel is by far the most energy dense source of electricity generation. For uranium fuel, the average extracted energy is 24 million kWh/kg, while an equivalent weight in coal's energy density is 8 kWh/kg [11]. While the means of extracting energy differs between the two sources, nuclear power offers a far more effective return on energy investment [11]. Further increasing the available energy per unit mass of nuclear fuel (referred to as fuel burnup) by increasing the enrichment of the fuel can allow for less fuel to be present in the reactor core while maintaining power production, decrease the risk of nuclear proliferation, and increase the time between refueling cycles. Using fuels to higher burnups would significantly improve the economics of nuclear energy production by LWRs.

A common metric to measure fuel burnup is gigawatt days per metric ton of uranium (GWd/MTU). It serves as an indicator of fuel activity and indirectly the irradiation damage of materials in the reactor core, such as the fuel cladding. In the early 1960s and 1970s, the regulatory limit for burnup was set at 40 GWd/MTU after economic analysis of fuel cycling determined it was optimal for 12 month fueling cycles [12]. Further burnup studies showed that after 40 GWd/MTU, the microstructure of  $\text{UO}_2$  fuel pellets began to change, and there is a higher rate of cladding corrosion and hydriding [13]. The majority of reactors in the U.S. have maintained a slightly higher average burnup maximum of around 46 GWd/MTU since 2006, as shown in Figure 5 [11].

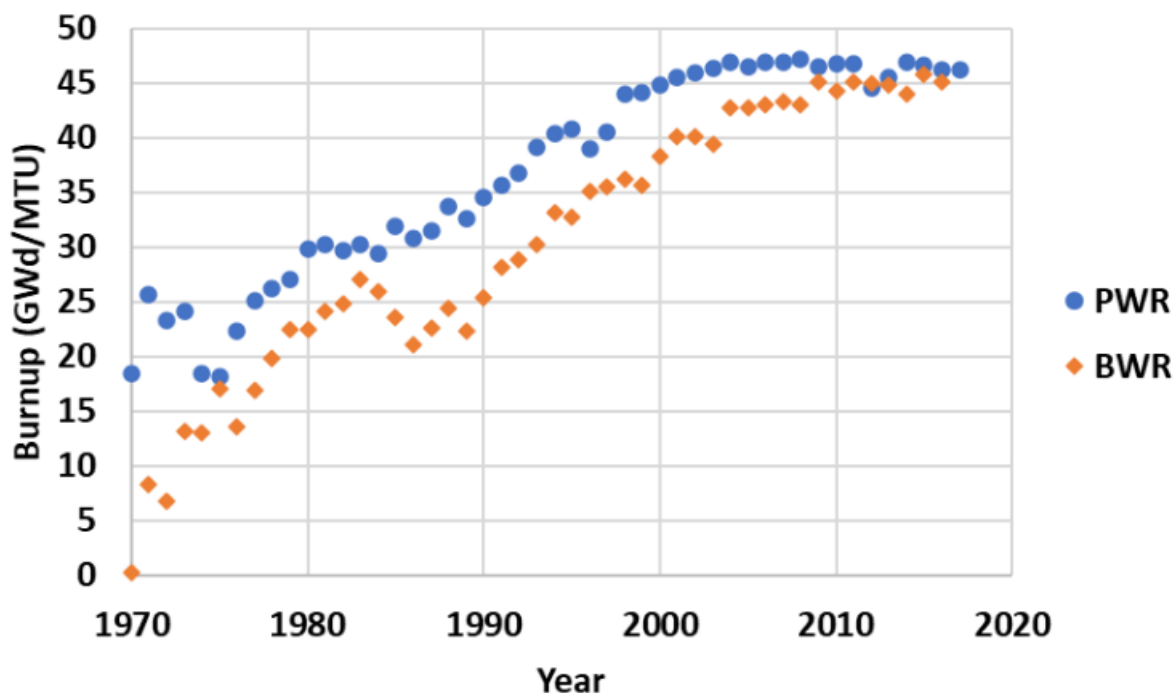


Figure 5. U.S Energy Information Administration annual average discharge burnup data [14].

In the pursuit of better economics by using longer periods between fuel cycles, fuel burnup was increased to the current regulatory limit of 62 GWd/MTU. Fuel pellets, cladding microstructure, and properties were improved to allow for the new higher burn-up regime [15]. Burnup at 62 GWd/MTU and below did yield some fuel pellet fracturing and relocation under accident conditions, but was not considered significant enough of an issue, thus reinforcing the promise of high burnup fuel and warranting further research efforts towards reaching higher fuel burnup [16]. It is noted here that a single rod LOCA testing study in the Halden Reactor Project with a fuel burnup of 92.3 GWd/MTU revealed significant fuel pellet fragmentation and dispersal at these high burnup levels [16]. During LOCA scenarios, there are concerns that the current fuel pellet and cladding technology may not guarantee a proper level of radioactive material release to the containment structure and environment through fuel fragmentation, relocation, and dispersal (FFRD) [17]. To safely obtain higher burnup, accident tolerant technologies need to be developed to safeguard against accident scenarios.

## 1.4 Accident Tolerant Fuel Concepts

Zr-alloys are prone to rapid steam oxidation above 1100 °C, lowering the mechanical integrity of the cladding in addition to producing excessive amounts of heat and hydrogen gas accelerating cladding heat up, which can lead to cladding failure. In reaction to the Fukushima-Daiichi accident, there has been a concerted effort by industry, national laboratories, the Department of Energy, and academia to develop the so-called Accident Tolerant Fuel (ATF) [18]. ATF designs have focused mostly on cladding development, but there has been an effort to enhance the mechanical integrity of the fuel aimed at resisting its fragmentation, by for example, introducing chromia particulates that pin the interfacial boundaries within the fuel. This discussion focuses on ATF cladding development, where both near-term and long-term strategies have been considered. The long-term strategy is to entirely replace the Zr-alloy as the cladding material with more high temperature oxidation-resistant materials such as SiC-SiC<sub>f</sub> composites or a FeCrAl alloy. Such a replacement will warrant changes in the reactor design given, among other factors, the vastly different neutronic properties of these materials compared to Zr-alloy. The near-term strategy for accelerated deployment of ATF on the current fleet is to deposit a coating of oxidation-resistant materials such as Cr on the current Zr-alloy cladding to increase the coping time in the event of an accident.

As long-term ATF material concepts, Cr- and Al-containing alloys (FeCrAl alloy) have been shown to provide enhanced corrosion resistance in high temperature steam environments due to the formation of passive oxides layers of Cr<sub>2</sub>O<sub>3</sub> and Al<sub>2</sub>O<sub>3</sub> on the alloy surface, as shown in Figure 6 [19]. Fe promotes the growth of spinel oxide during nominal reactor operating conditions, which is very resistant to oxygen diffusion. FeCrAl is progressing towards commercial readiness but there are concerns about the irradiation accelerated formation of a sigma-phase which can induce brittleness in the cladding. Additionally, the presence of Cr and Al make the alloy susceptible to weld-induced cracking and to radiation hardening and embrittlement near end-of-life irradiation [19].

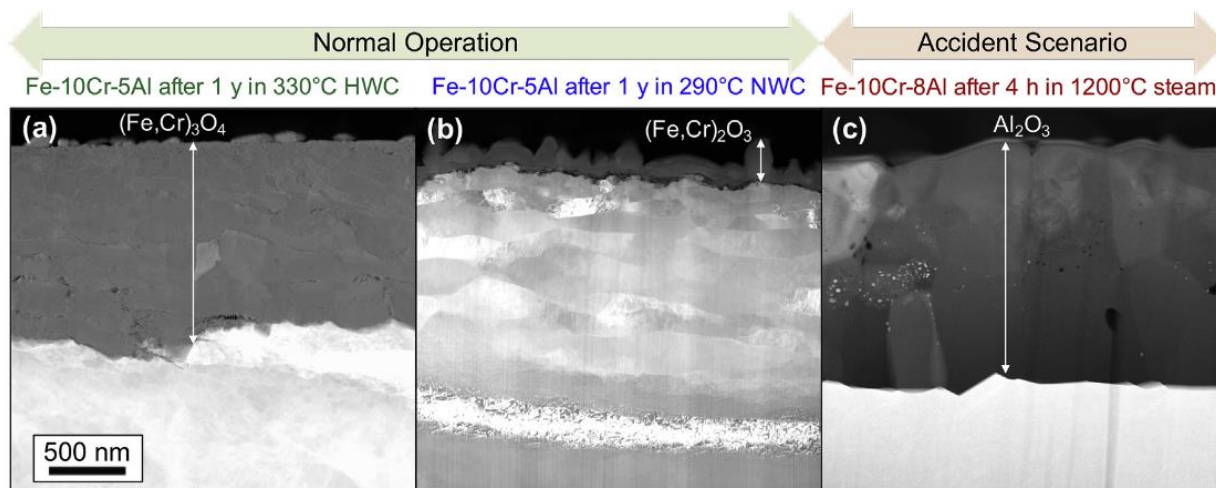


Figure 6. Cross-sectional SEM images showing the formation of spinel and aluminum oxide of FeCrAl cladding [18].

SiC-SiC<sub>f</sub> composites have been extensively studied in high temperature dry and wet environments outside of nuclear applications. This composite has been shown to have strong structural integrity at high temperatures, good thermal neutron economy, and favorable thermo-mechanical behavior [20]. The SiC-SiC<sub>f</sub> composite architecture maintains a high degree of resistance to cladding deformation during LOCA scenarios. While the SiC-SiC<sub>f</sub> composite shows very promising properties for ATF, it also has issues related to fission gas release during irradiation and corrosion in beyond-DBA scenarios with PWR water chemistry. Additionally, the manufacturing cost is still quite high. Thorough testing is still required to certify SiC-SiC<sub>f</sub> composite for use in LWRs.

Cr-coated Zr-alloy is a promising near-term option for ATF cladding. Chromium is used as an alloying element in Fe- and Ni-based alloys for use in many industrial applications as it imparts excellent corrosion resistance via the formation of a protective oxide layer, chromia, on the alloy surface. When alloyed, Cr will spontaneously form an oxide layer due to the higher thermodynamic stability of chromia. Chromia is passivating and forms a thin oxide layer that acts as a barrier to further oxygen diffusion into the alloy. For near-term and current reactor operations, application of a pure Cr coating with a thickness between ~5-30 μm (Figure 7) provides improved corrosion resistance over bare Zr-alloy while minimally impacting neutronics [21]. In addition, Cr-coatings have been shown to reduce

ballooning and burst sizes in LOCA scenarios [22]. Of the proposed ATF concepts, Cr-coatings show the highest level of technological readiness [18].

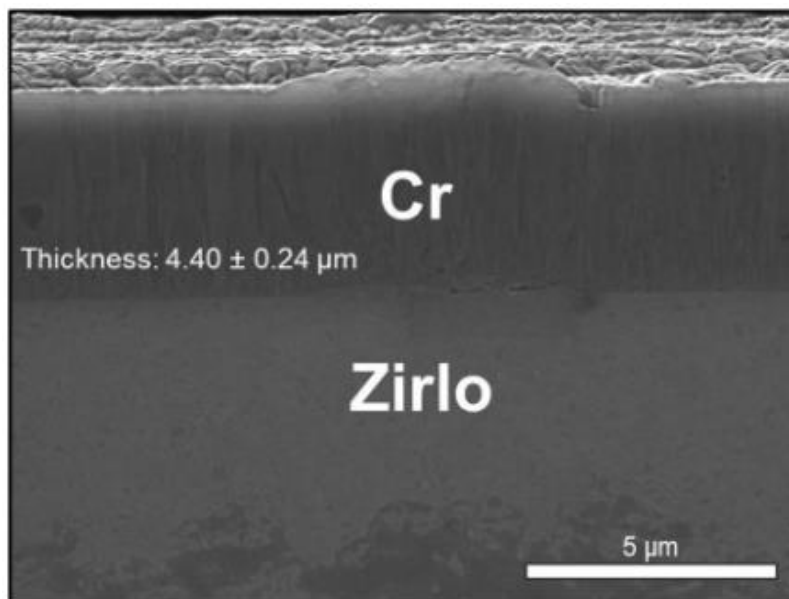


Figure 7. Cross-sectional SEM image of a Cr-coating deposited onto a Zr-alloy substrate [23].

Kane et al [22] performed simulated single rod burst testing by internally pressurizing closed cladding and heating until rupture on the leading ATF concepts (Cr-coating, FeCrAl, SiC). Results of this study are shown in Figure 8.

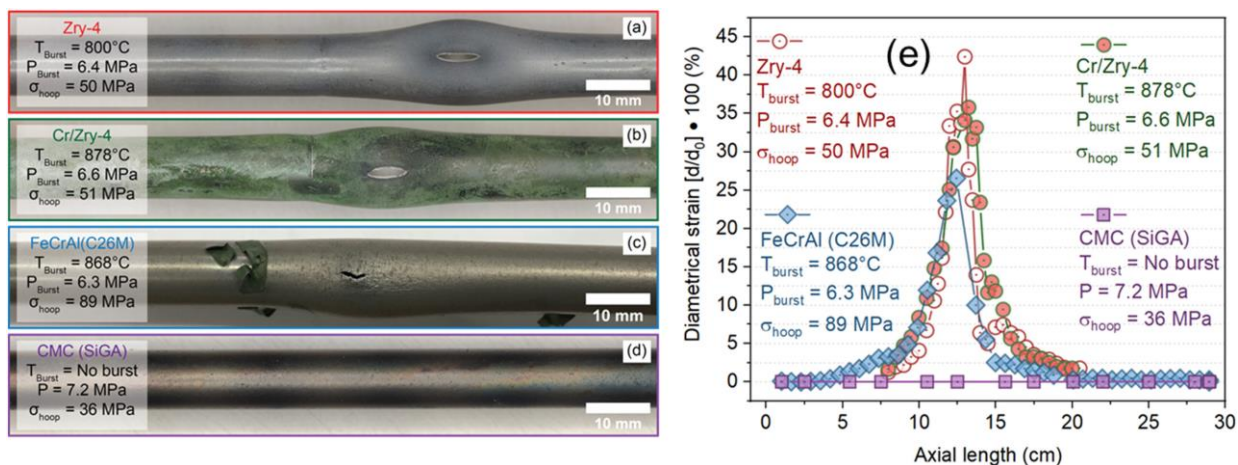


Figure 8. Simulated LOCA cladding rupture by Kane et al [22]. (a) Zry-4 cladding (b) Cr-coated Zry-4 (c) FeCrAl (d) SiC ceramic matrix composite (CMC).

## 1.5 Fuel Fragmentation, Relocation, and Dispersal (FFRD)

FFRD is a fuel rod destruction phenomenon which can occur under LOCA conditions and is of particular concern at high fuel burnup. Here, the uranium-dioxide pellets can undergo fragmentation and the fragmented fuel particulates can relocate radially or axially in the cladding due to the cladding ballooning. In the event of a cladding burst, the fuel particulates can be expelled out of cladding and disperse in the surrounding water coolant.

The current burnup regulatory limit is 62 GWD/MTU, but there are plans to increase burnup to 75 GWD/MTU [24]. Extensive safety reviews are necessary for the new higher burnup regulatory limit to ensure minimum impact to the environment under accident scenarios. FFRD has been observed in LOCA testing for <62 GWD/MTU fuel burnup but was not a high priority for investigation by the NRC [24]. During LOCA scenarios, fuel cladding temperature rapidly increases in the core causing an increase in internal cladding pressure. Fuel pellet integrity begins to degrade leading to fracturing. The increase in temperature can result in plastic deformation of the cladding wall leading to ballooning, and eventually bursting. Cladding rupture can release fractured fuel pellets of sufficiently small size into the coolant. At higher burnups >62 GWD/MTU, FFRD becomes more pronounced as fuel pellets can be pulverized into finer particles than in the current burnup limit. As shown in Figure 9, finer fuel

fragments were present in higher burnups which axially relocate to form hotspots which become sites for cladding rupture. The extent of fuel fragmentation depends on the fuel pellet characteristics, but the fuel relocation and dispersal depend strongly on the characteristics of cladding.

test #	2	7	6	11	10	12	13	14	3	5	9	4
burnup, MWd/kg	0	44.3	55.5	56	60	72.3	74.1	71.1	81.9	83	90	92
balloon strain, %	54	23	49	25	15	40	45	55	8	15	61	62
radiography												
ceramography							fragment size distribution only	fragment size distribution only				
fragment size	coarse	coarse	coarse	coarse	coarse & some fine	coarse & fine	coarse (& fine?)	coarse (& fine?)	medium & fine	medium & fine	medium & fine	medium & fine
gamma scan												
flask bottom →												
HBS width												
dispersal (qualitative)	none	none	none	none	some	some more	nearly none	did not fail	n/a	much	much more	much more

Figure 9. Post-test characterization for fuel claddings at increasing burnups performed at the Halden reactor

[24].

While the process of fuel fragmentation is widely recognized, the actual mechanism causing fuel fracturing is still being studied [25]. It is well known that higher fuel burnups cause a decrease in fractured pellet sizes. In addition, a porous and fine-grained structure forms on the edges of a fuel pellet called a high-burnup structure (HBS) which increases in prominence at higher burnups. The HBS alone does not cause fuel fragmentation. However, as the microstructure is weakened and porous regions become more prevalent at higher burnups, the overpressure fission gas bubbles can exert more

strain on the degraded pellet structure. As fission gas is released during cladding depressurization in a LOCA scenario, the trapped fission gas bubbles are released from the pellet matrix, fracturing the fuel. Fracturing can be mitigated by several factors: (i) hydrostatic pressure inside the cladding can restrain the release of fission gases and therefore reduce fractures, (ii) fuel cladding can constrain pellet fracturing, and (iii) reducing the heating rate of the cladding can mitigate the propensity for fracture [25].

Two prerequisites for fuel relocation are fuel fragmentation and radial cladding distension [26]. Fuel pellets are stacked with a narrow gap between the pellets and the cladding wall. During normal operation, expansion of pellets from both thermal expansion and irradiation swelling reduces the gap to the wall. The ratio of the volume of the pellets and the total volume inside the cladding is called the packing fraction. Pellets fracturing in this configuration reduce the packing fraction depending on the size of the fragmented pellets, but they are ultimately constrained from radial and axial relocation by the cladding. If the cladding were to deform radially, i.e. balloon, the added volume would allow fragmented pellets to migrate to the ballooned region. High burnups typically produce finer grained fuel fragments which can yield a higher packing fraction than low burnup fuel, allowing for more fragments to relocate in ballooned regions.

Cladding ballooning eventually leads to rupture and subsequent dispersal of fuel particles [24]. The amount of pellet mass dispersed depends strongly on two factors: the fuel burnup and the cladding rupture size. Fuel burnup higher than 72 GWD/MTU produces fine fuel fragments which can relocate axially upon fuel pellet column collapse and with minimal hoop strain, as shown in Figure 10. During rupture, fuel fragments can be swept up from below the rupture site and get dispersed into the reactor core [26]. This behavior is not always present as there are many factors that contribute to upward pellet relocation like internal differential pressure, fragment size, how freely gas flows through the pellet matrix, and the burst size. While there are stochastic differences in burst size between different burnups, the cladding that has large burst sizes has higher fuel dispersal than their smaller burst opening counterparts. Large burst openings allow for a larger range of fuel fragment sizes to be dispersed.

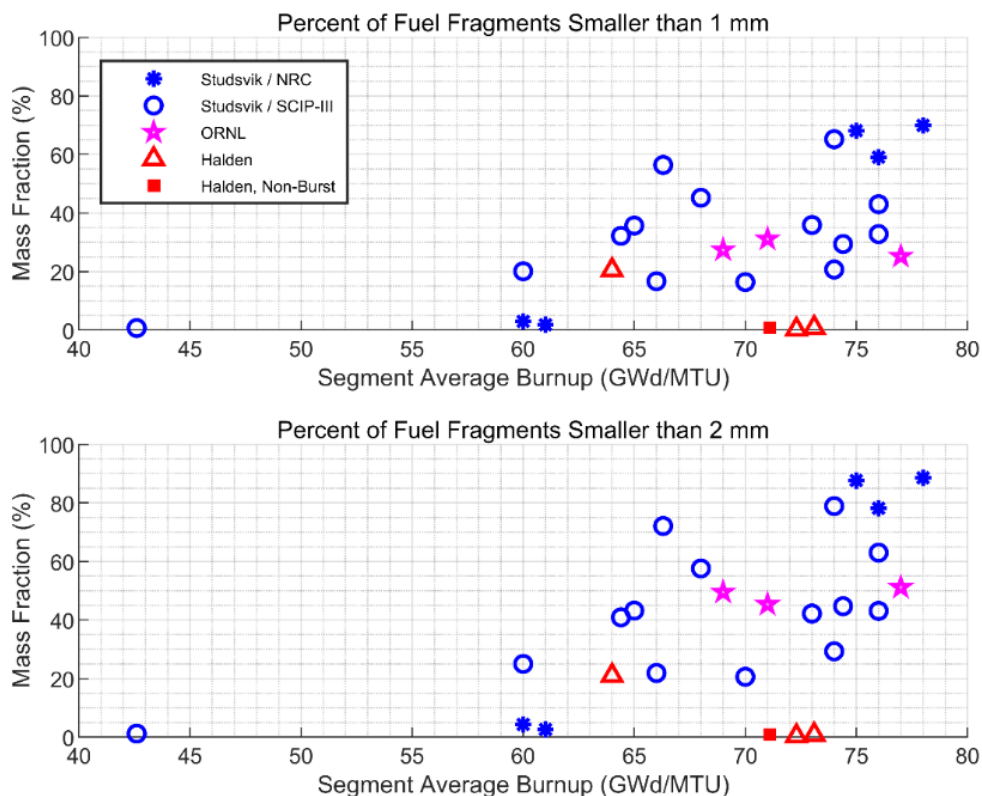


Figure 10. Mass fraction of fuel fragments smaller than 1 mm and 2 mm in high fuel burnup level [26].

## 1.6 Ballooning and Burst Behavior of Cladding

Ballooning is caused by a pressure differential in the cladding where the internal pressure far exceeds the external pressure in the case of the loss of the pressure boundary in the core. Under normal operating conditions in PWRs, Zr-alloy fuel cladding is internally pre-pressurized to 1.7-2.5 MPa for <65 GWd/MTU burnup [27]. Fission gas buildup throughout the lifetime of a fuel cladding results in a typical end of life internal pressure of PWR fuel of 4.0-5.5 MPa. Under normal operating conditions, the cladding can withstand this internal pressure without deforming due to the pressure boundary of the primary loop. However, under LOCA conditions where the fuel temperature rapidly increases with higher fuel burnup >65 GWd/MTU, cladding internal pressure can reach >6.5 MPa with the loss of external pressure boundary. At the same time, the cladding experiences a decrease in strength with increasing temperature. Cladding mechanical strength is also tied closely to its thermal distribution as

temperature-dependent  $\alpha$  to  $\beta$  at  $\sim 870$  °C phase transition can cause the Zr to become more ductile [28], facilitating softening and plastic deformation. Local cladding hotspots deform plastically more than the surrounding regions and will accumulate more localized deformation, becoming potential sites for ballooning to initiate. Cladding rupture or burst occurs when the weakened ballooned regions can no longer sustain the internal pressure. Figure 11 shows photographs of ballooned and burst regions of a Zr-alloy cladding as a function of the initial internal pressure and the heating rate [14].

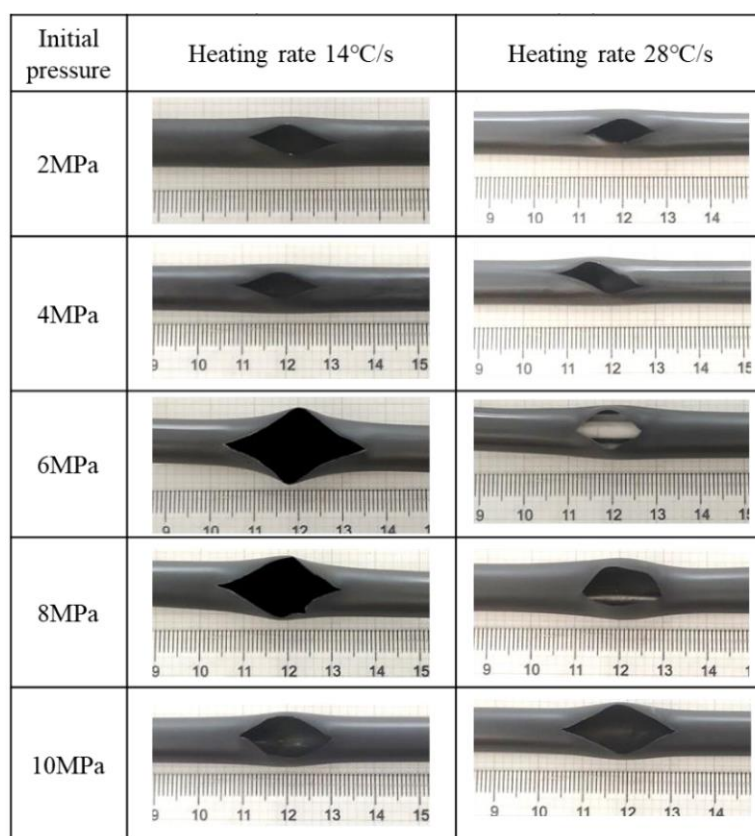


Figure 11. Ballooning and burst openings of a Zr-alloy subjected to two heating rates, 14 °C/s and 28 °C/s at various initial internal pressures of the cladding [29].

Burst opening size is related to heating rate, internal pressure, and ductility of the cladding. A typical LOCA scenario can cause a cladding heating rate as high as 25 °C/s at its peak, to around 1 °C/s at its minimum before being resolved [30]. High heating rates do not allow sufficient time for the alloy to appreciably deform before the internal hoop stress overcomes the tensile strength of the cladding.

Conversely, a slow heating rate will give the alloy sufficient time to balloon before rupture. Typically, for this reason, the more time given to the cladding to deform, the higher will be the burst temperature and pressure. An increase in initial pressure typically results in larger burst openings, however as shown earlier in Figure 11, this is not always the case as other environmental factors can impact how the cladding ruptures. It is worth noting in the context of the results presented in Figure 11 that the burst size levels off or even decreases at initial internal pressures exceeding 8MPa.

Conditions inside of PWRs can drastically change ballooning behavior in Zr-alloys through oxidation, hydrogen uptake, and irradiation. In an aqueous hydrothermal environment, small amounts of oxygen can diffuse into the Zr-alloy cladding before a stable  $ZrO_2$  layer forms on the surface [5]. The formation of  $ZrO_2$  layer reduces the load bearing wall thickness. In addition, the formation of oxygen-stabilized  $\alpha$ -Zr can embrittle the Zr-alloy. Finally, hydrogen ingress into the cladding can lead to embrittlement. Hydrogen could form as a fission gas, through radiolysis of coolant water in the reactor, and as a byproduct of Zr-alloy oxidation in water, among other sources. Hydrogen diffusion into the cladding can lead to the formation of embrittling hydride phases in the cladding. A reduction in ductility paired with the lower fracture threshold of a thinner cladding wall can result in a through-wall fracture before the cladding can deform enough to delay a rupture. Thus, oxidation and hydriding are important considerations not only in LOCA scenarios, but also for the use of high burnup fuel with its associated effect of enhancing internal pressure by way of increased fission product gases and possibly radiation-induced fuel swelling.

## 1.7 Objective

There is need from industry to extend the operational lifetime and fuel cycle period of nuclear fuel through the higher burnup fuel. Increasing fuel burnup would achieve better fuel economy but comes at the increased risk of potentially worse cladding performance in LOCA scenarios. Of the currently studied ATF claddings, Cr-coatings stand out as the best near-term option in terms of performance and technological readiness. The objective of this study is to evaluate the performance of Cr-coated Zr-alloy

in simulated LOCA conditions to better understand how to mitigate potential cladding failure. This was achieved by exposing uncoated and Cr-coated Zr-alloy to reflood and burst conditions experimentally and studying (i) the post-quench ductility of the Zr substrate through ring compression testing, scanning electron microscopy energy dispersive spectroscopy, and microhardness testing; (ii) image analysis and burst characterization of ruptured cladding.

## 2 Experimental Methodology

### 2.1 Reflood Testing to Simulate LOCA

#### 2.1.1 Reflood Test Facility

A single rod reflood facility was designed and built at the University of Wisconsin-Madison for the purpose of studying the thermomechanical performance of ATF cladding candidate materials and coatings under simulated LOCA conditions [31]. Figure 12 shows a schematic illustration of this facility. The test section consists of tube flanges, quartz tube, cladding specimen, configuration of surrogate fuel pellets, thermocouples, and the heating furnace. The water coolant is heated in an external tank by two 5 kW immersion heating coils located at the bottom of the tank. Reverse-Osmosis (RO) water is used to avoid deposition of solid contaminants onto the water contacting surfaces in test facility and the cladding. A thermowell measures the water temperature during the heating phase. A Grundfos CRE vertical, multistage centrifugal pump is used to direct water into the test facility. An OMEGA Liquid Turbine flow meter measures the flow rate inside the water line. Two 3-way valves are used before and after the flow meter to direct water from the tank bypass line and to isolate the water line from the steam/gas line. A drain is placed at the end of the water line to allow for pipe pre-heating immediately before a quench test.

The testing procedure was divided into three distinct stages: pre-heating, feed line heating, and reflooding. RO water was heated and boiled in the water tank for two hours to degas. During the degassing, the furnace was heated to the target temperature with the cladding inserted for the reflood test. In addition, argon gas was flowed through the quartz tube to mitigate oxidation on the outer surface of the cladding during heating. After two hours, the RO water was flowed through the pump and preheated pipes underneath the test section to minimize heat loss during reflood. The water was drained before filling the quartz tube. Whence the pipes were heated, the reflood test was initiated. The pump is engaged to drive water up through the quartz tube at a flow rate of 4.5 cm/s. The temperature of the four internal thermocouples was recorded during reflood and when each point reached quench temperature the test was terminated.

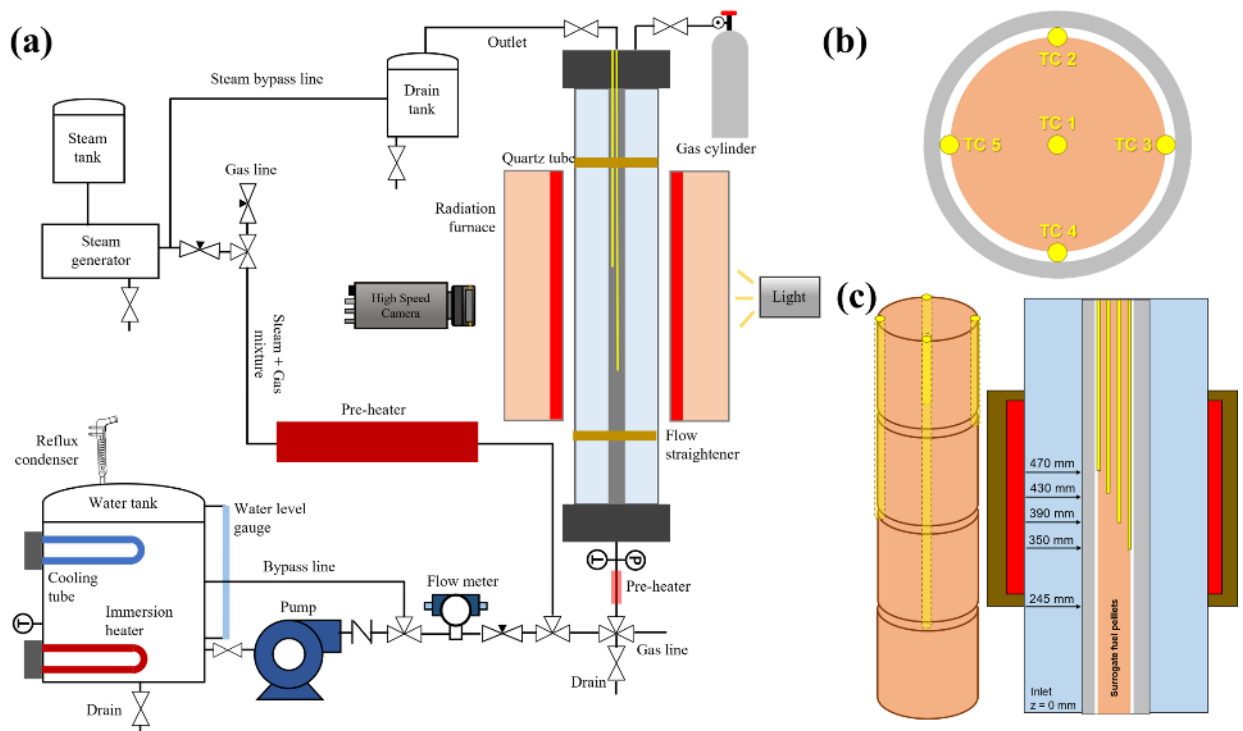


Figure 12. Schematic illustration of (a) single rod reflood facility, (b) configuration of surrogate pellet and thermocouples (indicated as TC 1, TC 2, TC 3, TC 4, TC 5) inside the cladding, and (c) axial installation of thermocouples [31].

### 2.1.2 Sample Preparation

ZIRLO® (henceforth referred to as Zr-alloy) cladding, procured from Westinghouse, was used throughout this research. 16” long sections of the cladding were cut from the longer cladding tube for all uncoated and Cr-coated research work. All uncoated and Cr-coated Zr-alloy tubes underwent polishing for a consistent surface condition and for promoting adhesion of Cr coating. For effective and uniform polishing, each as-received Zr-alloy tube section was mounted on a lathe set to a rotational speed of 600 RPM. SiC carbide paper (600 and 800 grit) cut to a width of 2” and a length of 8” was used for polishing medium (this procedure is often referred to as grinding in metallography literature, but the term polishing is used here to better communicate the purpose of this step). For polishing, the SiC paper was tensioned against the rotating cladding such that a uniform, thin line of the paper was always in contact with the cladding surface. During the polishing procedure, the SiC paper was slowly

moved laterally across the cladding from end-to-end. A maximum of 3-4 passes of 600 grit and 2-4 passes of 800 grit were used to complete the polishing procedure for the Zr-alloy tubes. Profilometry of the cladding surface was performed with a Zygo New View 9000 instrument to ensure quality and consistency between pre-test sample polishing. Two metrics were used to measure the quality of the polishing; the arithmetic mean roughness and the peak-to-valley roughness. Primarily, the mean roughness was used as the determining factor for quality of the polish, with lower roughness numbers implying a smoother surface with minimal scratches. Figure 13 shows that the mean roughness (Sa) for uncoated Zr-alloy tube was  $0.18 \mu\text{m}$ . The maximum allowable roughness was chosen to be  $0.20 \mu\text{m}$ .

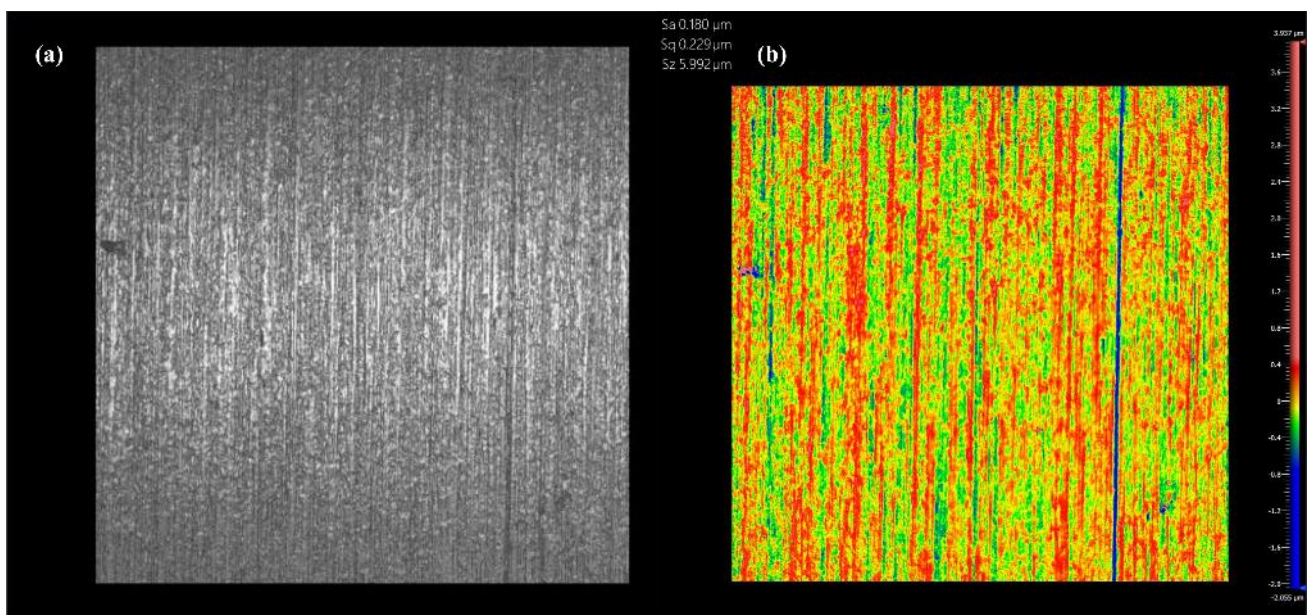


Figure 13. Pre-test and pre-coating surface roughness of an uncoated Zr-alloy cladding.

### 2.1.3 Cold spray Cr-coating deposition

Cr coatings were deposited on Zr-alloy cladding tubes by the cold spray materials deposition process using an industrial system at the Nuclear and Applied Materials Research Group (NAMRG, the author's group) at the University of Wisconsin, Madison. The facility is a CGT Kinetiks 4000-34 system. A Type 24 tungsten carbide de Laval nozzle was used to deposit the feedstock Cr powder. Prior to the cold spray process, the cladding surfaces were lightly polished using 600 grit SiC abrasive paper to

remove the native oxide layer followed by cleaning with ethanol and deionized (DI) water. Two carrier gas mixtures were used to deposit Cr-coatings in the current study: a mixture of nitrogen (5%) and helium (95%), and pure nitrogen (100%). Carrier gases (which propel the particles) were heated to 500 °C and 750 °C, for the nitrogen/helium mixture and pure nitrogen, respectively, to accelerate the powder particles in the converging-diverging nozzle system. All cold spray processes were performed using a pressure of 3.8 MPa with the nozzle stand-off distance 26 mm from the substrate. The traverse speed of the cold spray gun and rotational speed of the tube section in a lathe was 3.4 mm/s and 600 rpm, respectively. The pitch (i.e., distance between paths along the helix) was maintained at 0.5 mm. The cold spray parameters were chosen to produce 50-60  $\mu\text{m}$  thick Cr coating on the cladding surfaces. Figure 14 (a) shows the photograph of cold spray deposition system during the Cr coating deposition. The cold spray nozzle system controlled by a robot arm sprays the feedstock powder while moving from one end of the cladding tube to the other end at a constant traverse speed. Figure 14 (b) shows photographs of the uncoated cladding, the as-deposited Cr-coated cladding, and the polished Cr-coated cladding. The as-deposited surface showed grey, non-reflective color due to the inherent surface roughness of the top layer of cold spray coating. Then, the coated tubes were polished with 600-grit SiC abrasive paper to reduce the coating thickness down to 30  $\mu\text{m}$  and to reduce the roughness of surface. The claddings were then cleaned with DI water, acetone, and ethanol to remove any possible residual deposits from the polishing process.

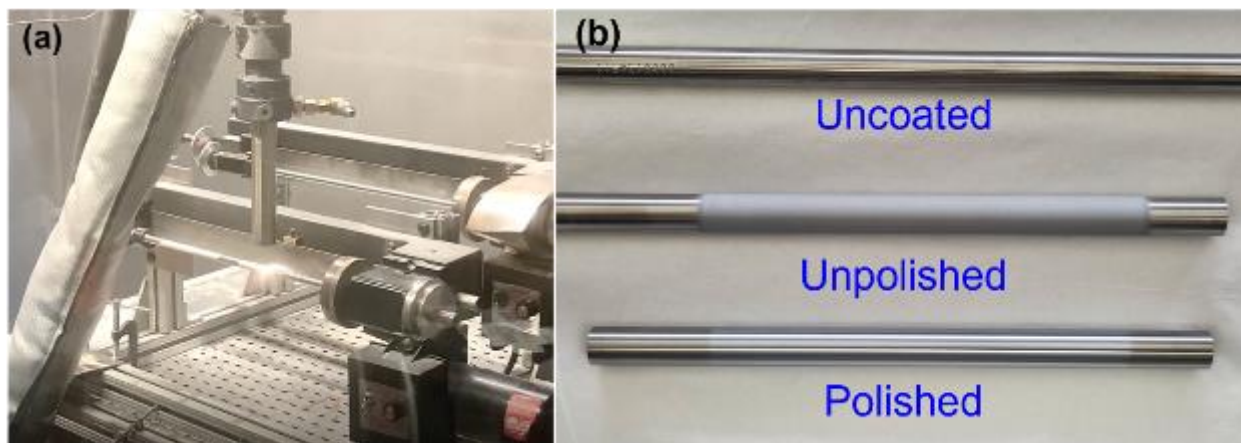


Figure 14. Photographs of (a) cold spray coating system during the Cr coating process and (b) example of Zr-alloy samples before coating, after the coating deposition but before the polishing, and after the polishing.

#### 2.1.4 PVD Cr-coating deposition

Zr-alloy cladding tubes deposited with Cr using physical vapor deposition (PVD) process were also investigated in this study to understand the effect of the coating deposition method and microstructure. The PVD Cr-coating deposition was performed in collaboration with the company Acree Technologies Incorporated. An advanced PVD process referred to as high-power impulse magnetron sputtering (HiPIMS) was used. HiPIMS is a relatively recent advanced sputter deposition technique, in which very short high-power pulses are applied to the sputter target. The pulse frequency is typically between 50–5000 Hz and resulting duty cycles are only 1–3%. The peak power densities are on the order of kW/cm<sup>2</sup>. These high-power pulses induce much greater ionization fractions (up to 70%) compared to conventional PVD processes. To accelerate the ions produced during a HiPIMS pulse toward the substrate, a negative bias is usually applied to the substrates. The mixing imparted by high energy ions HiPIMS process provides greater coating-substrate interfacial adhesion and a denser coating microstructure. Uniform coating thickness was achieved by rotating the cladding during deposition in the PVD chamber. No grinding or polishing was done for the PVD coated cladding, as the coating was a uniform and smooth surface with a thickness of 8 microns.

### 2.1.5 Single Rod Reflood Test Matrix

A total of 21 claddings were subjected to reflood tests including uncoated, CS Cr-coated, and PVD Cr-coated Zr-alloy claddings. The list of cladding types along with the reflood test furnace temperature used in this study are summarized in Table 2. Figure 15 shows the cladding sections after being tested at various reflood test temperatures (i.e., the temperatures to which the cladding tubes were heated prior to quenching).

Table 2. Reflood testing matrix. (\*: Number of reproducibility tests)

Cladding Type	Reflood Test Furnace Temperature [°C]				
	600	800	1000	1100	1200
Uncoated ZIRLO	O**	O	O**	O*	O
CS (He) ZIRLO	O	O	O	O	O
PVD ZIRLO	O	O	O	O	O

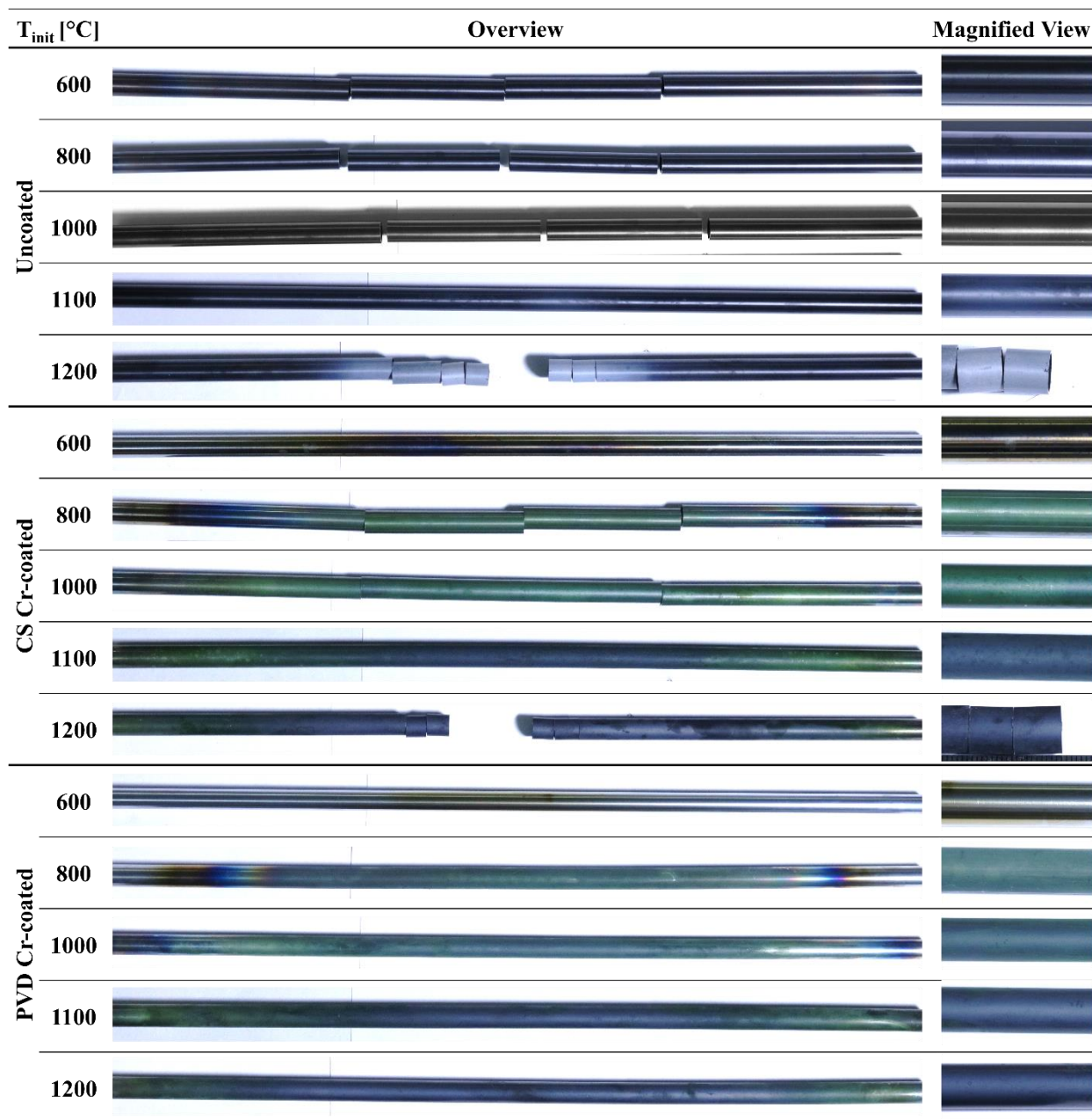


Figure 15. Material characterization and mechanical testing of post-quench uncoated and Cr-coated Zr-alloy cladding. Shown on the left are the reflood test temperatures.

### 2.1.6 Ring Compression Testing (RCT)

After the reflood tests, the ductility of the claddings was evaluated by performing ring compression tests (RCT). The central 10 mm section of each tube was used for cross-sectional SEM imaging. The

four nearest 8 mm sections were cut with a low speed saw to perform RCT. Figure 16 shows a drawing of how the post-test cladding was sectioned into four samples for RCT.



Figure 16. Drawing showing the sectioning for cross-sectional imaging and RCT of Zr-alloy tubes after the reflood tests. Sections 1-4 are numbered for.

RCT was performed using an MTS Criterion Model 42 Electromechanical Universal Test System, as shown in Figure 17 (a). By applying a force onto the surface of a Zr-alloy tube section sample (in the radial direction), and measuring the displacement from an initial preloaded position, the ductility of the sample could be assessed by the offset displacement strain. To ensure proper contact of the loading plate with the sample, the tube section was initially preloaded to approximately  $\sim 10$  N. After the preload the RCT plate was impressed upon the cladding followed by a gradual vertical translation of the plate at a rate of 2 mm/min. The sample was loaded to a maximum displacement of 2 mm from the preloading position. As the sample is loaded, it plastically deforms from a circular geometry to an elliptical shape (Figure 17 (b)), which subsequently flattens at the points of contact. Figure 18 shows an example of pre- and post-test sample image with 2 mm displacement.

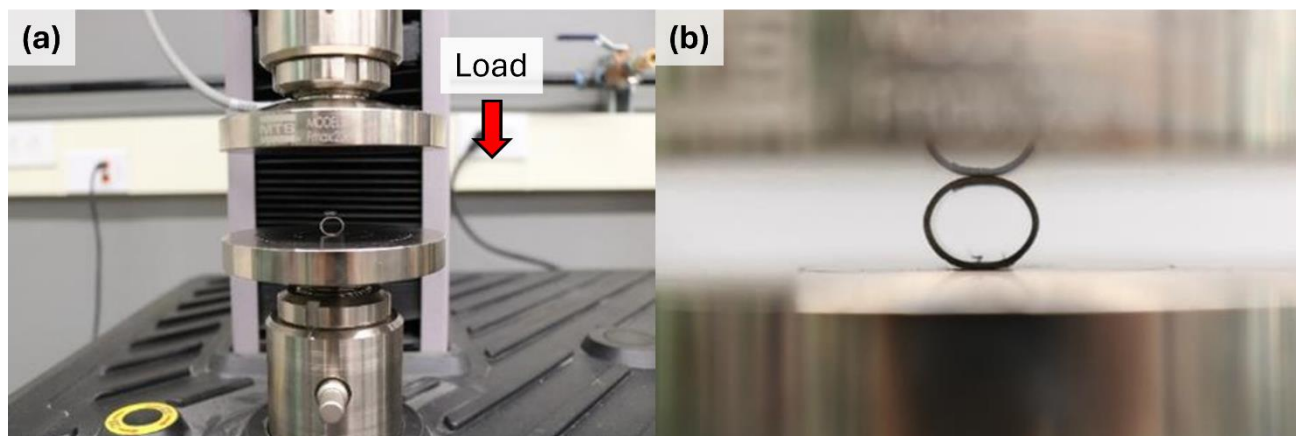


Figure 17. Ring compression testing of post-quench Zr-alloy cladding. (a) MTS Criterion Model 42 Electromechanical Universal Test System. (b) photo of ring compression test being performed for an as-received, uncoated Zr-alloy cladding section.

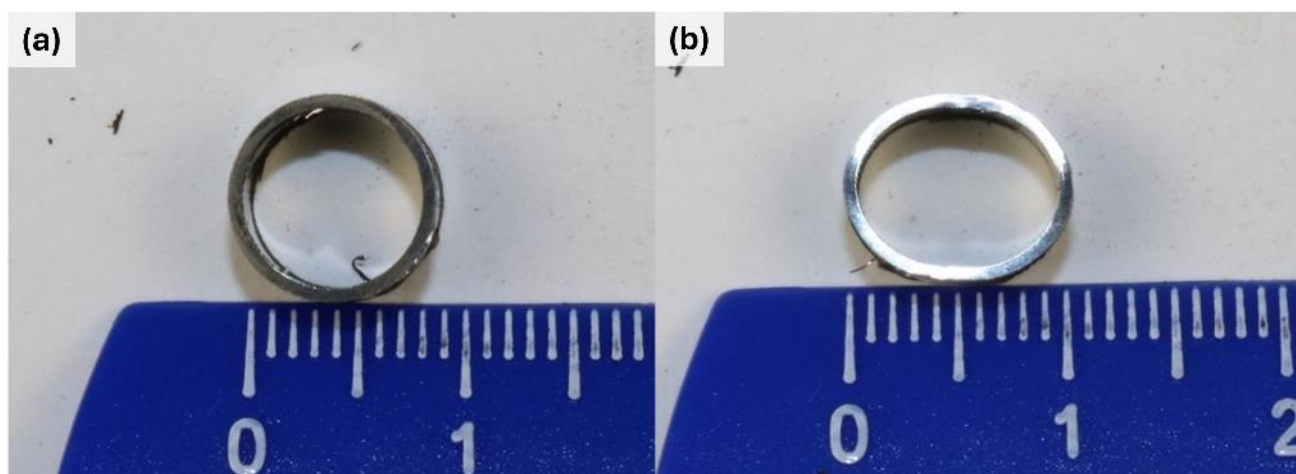


Figure 18. Pre-test and post-test shape of ring compression samples. (a) untested, uncoated Zr-alloy pre-RCT (circular), (b) untested, uncoated Zr-alloy post-RCT (elliptical).

The test was terminated when one of two conditions was met: 1) the sample reaches the full displacement of 2 mm and is subsequently unloaded at a rate of 2 mm/min, or 2) the sample experiences a sudden load drop of approximately  $\sim 25\%$  of the current load, because it is indicative of notable cracking of the cladding wall across its thickness. For samples that reached 2 mm without a significant drop in load, the offset strain was calculated by fitting the loading slope to intersect with the maximum load of the sample and comparing the difference in the loading and unloading slopes at zero load, as

shown in Figure 19. For cracked samples, offset strain could not be calculated, instead, a qualitative analysis by cross-sectional SEM imaging and load-displacement plotting was performed.

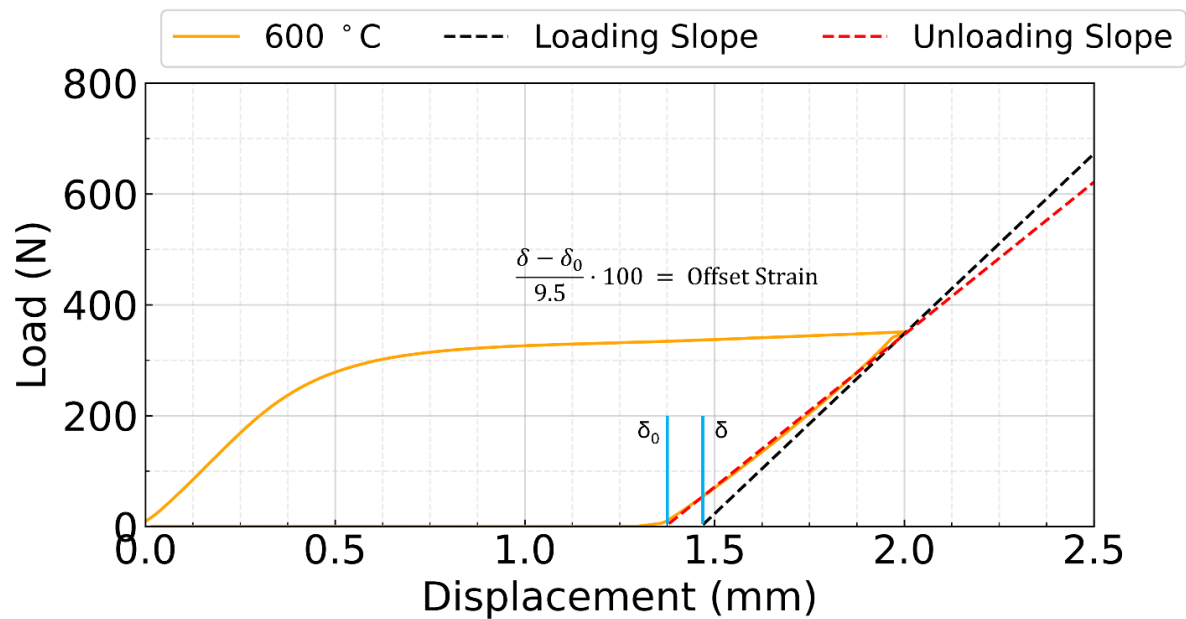


Figure 19. RCT load-displacement plot of an uncoated Zr-alloy after post-quench test from 600 °C sample. An example of offset strain calculation is shown.

## 2.2 Characterization of Post-quench Ductility

### 2.2.1 Micro Indentation Testing

Microhardness testing of the cladding sections mounted and polished in cross-section were performed with a Vickers indenter using a load of 50 grams, using a Buehler Micromet II Digital Microhardness Tester (Figure 20). To ensure accuracy, the microhardness tester was calibrated by measuring the hardness of standard steel sample of known hardness provided by the company, Buehler. While, this test provides a measure of the strength of the alloy, in this study it was used as an indicator of oxygen ingress into Zr-alloy cladding during the reflood tests. Initially, oxygen diffuses into the Zr-alloy cladding substrate rather than forming a discrete layer of stoichiometric  $\text{ZrO}_2$ . The oxygen-stabilized  $\alpha$ -phase of Zr that forms due to this oxygen diffusion is expected to have a higher hardness due to solid solution strengthening, with the hardness correlating to the concentration of the dissolved

oxygen at that particular point in the concentration-depth profile. Thus, the depth of oxygen diffusion into the Zr-alloy may be inferred from the hardness profile. Thus, microhardness testing, in addition to measuring hardening (and associated embrittlement), was also performed as a supplementary characterization to establish the oxygen penetration depth of post-quench claddings.

Microhardness testing was performed on the sections of post-quench samples tested at 800 °C and 1200 °C, as well as untested samples for both uncoated and Cr-coated Zr-alloy. In total, nine samples were subjected to microhardness testing including, uncoated Zr-alloy, and CS (He) and PVD Cr-coated Zr-alloy. Samples were prepared by mounting in cross-section in KonductMet mounting compound and polishing to a mirror finish. Five indents were made along the depth of the cladding wall, as shown in Figure 21. Each indent was separated at minimum 70  $\mu\text{m}$  to ensure that deformation regions around the indents do not overlap and affect hardness measurements of the subsequent indents.

The location of the indent on the cladding cross section was chosen using a 100x and 1000x optical lenses, then the indenter is pressed into the sample. Hardness was measured by comparing the cardinal dimensions of the indentation created by impressing the Vickers indenter on the sample surface. A large length of either dimension infers a lower hardness which is typically representative of higher ductility.

The distance of each indent from the inner diameter of the cladding was used to eliminate substantial length differences between unoxidized and oxidized samples, as the oxide layer of the inner diameter is very small (<10  $\mu\text{m}$ ) relative to the oxide layer formed on the outer diameter.

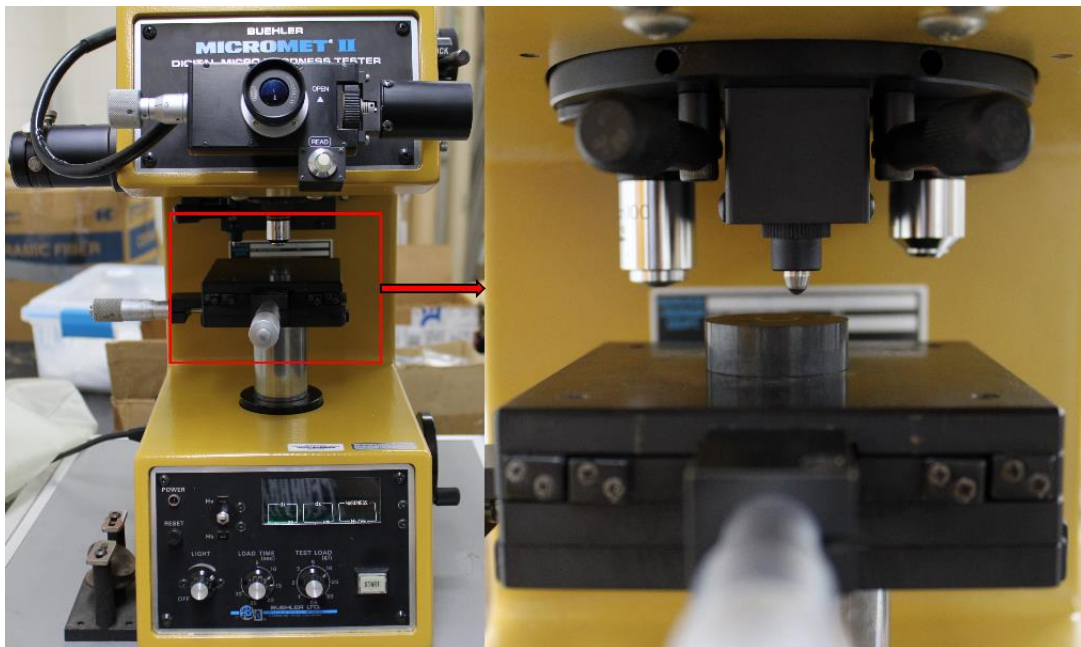


Figure 20. Buehler Micromet II Digital Microhardness Tester used in this study.

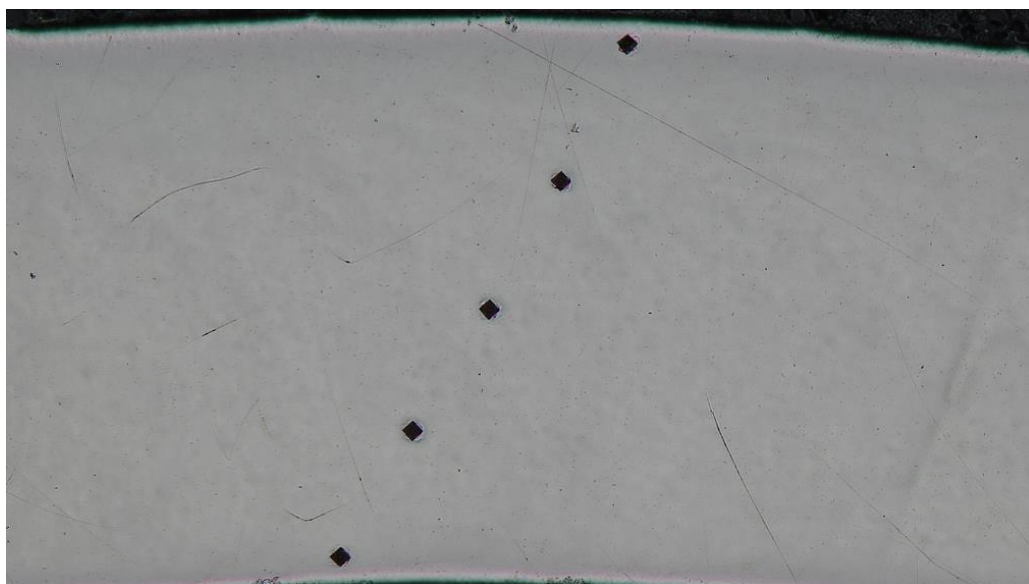


Figure 21. Optical microscopy images showing indents from microhardness tests of an untested, uncoated Zr-alloy sample with five micro-indents along the cross-sectional depth of the cladding wall.

### 2.2.2 Scanning Electron Microscopy – Energy Dispersive Spectroscopy (SEM-EDS)

A Zeiss Gemini 450 SEM was used for imaging and energy dispersive spectroscopy (EDS) in the line-scan mode was used to determine the atomic concentration of Zr, Cr, and oxygen in the Zr-alloy

substrate. The Zr-alloy samples used for microhardness testing were also used for SEM-EDS line-scan analysis. An example of the line-scan path across the cladding wall thickness is shown in Figure 22. EDS was performed with a bias voltage of 10 kV at a magnification of 1000x for all three of the 1200 °C and 800 °C post-quench samples. A total of 50 data points were collected across the cladding wall thickness with a dwell time of 65 seconds per point. A long dwell time is necessary to provide good counting statistics. For uncoated Zr-alloy, only Zr and oxygen are measured while for Cr-coated Zr-alloy Cr was also included in the analysis.

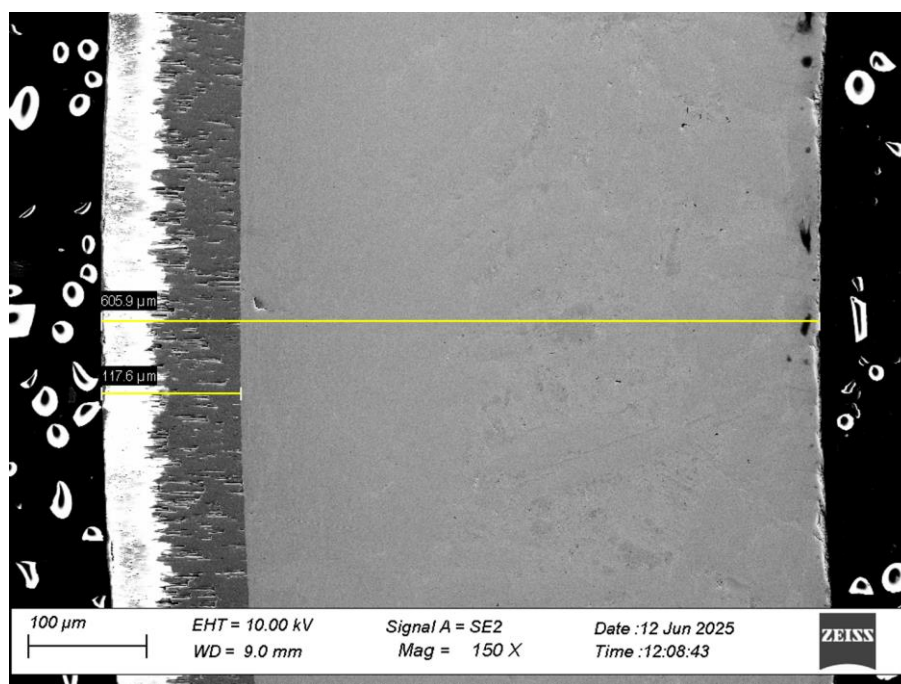


Figure 22. Cross-sectional SEM image showing the line trace (yellow lines) for EDS line-scan compositional analysis performed across the cladding wall thickness for the 1200 °C post-quench uncoated Zr-alloy sample. Line-scan compositional analysis was performed from the top of the oxide layer to the inner diameter of the cladding.

## 2.3 Single Rod Burst Test

### 2.3.1 Single Rod Burst Test Facility

The single rod burst test facility was constructed to investigate the effect of Cr coatings on ballooning and burst behavior of Zr-alloy cladding. This facility is designed to simulate a loss of coolant accident (LOCA) scenario where the internal pressure of the fuel cladding exceeds its mechanical strength, which can lead to plastic deformation (ballooning) and subsequently, burst (rupture). The test facility consists of four main components: the furnace, the gas pressurization system, the cladding fixturing systems, and shielding. Figure 23 and Figure 24 show the photograph and a schematic illustration of the facility. Heating is imparted by an external Mellen Microtherm Split radiant furnace capable of reaching a maximum temperature of 1200 °C with a linear heating ramp rate of 10°C/second. The cladding is housed concentrically in a quartz tube which also serves as shielding. Four mounting fixtures are responsible for holding the cladding in place inside the quartz tube. As shown in Figure 25, the cladding tube is affixed to a top and bottom spacer rod to locate the cladding at the center of the furnace. The top spacer rod (c) attaches to an end cap (d) by a threaded nut, while the bottom spacer (b) hangs freely inside the spacer anchor (a) to allow for free axial thermal expansion. The furnace can be opened away from the quartz tube and closed around it, and it also has an internal temperature sensor that outputs to a built-in LCD screen. There is roughly 10 to 20 mm gap between the furnace heating coils and the quartz tube. Fiberglass insulation is applied to the top and bottom openings of the furnace to prevent radiation heat leakage between the quartz tube and the furnace. Argon gas flows both inside and outside of the cladding and serves two purposes: (i) to pressurize the cladding internally and (ii) to mitigate oxidation of the outer surface of the cladding. Two gas cylinders supply the argon gas separately for these purposes, as shown in Figure 23. The primary cladding argon tank is rated to a maximum of 24 MPa while the atmospheric argon tank is rated for ~8 MPa. A series of regulator valves serve the function of isolating the gas tank from the facility when performing the burst test and for the precise control for the supplied pressure input. The primary shield of the cladding is comprised of a 750 mm L x 46 mm ID x 50 mm OD quartz tube that encloses the test assembly.

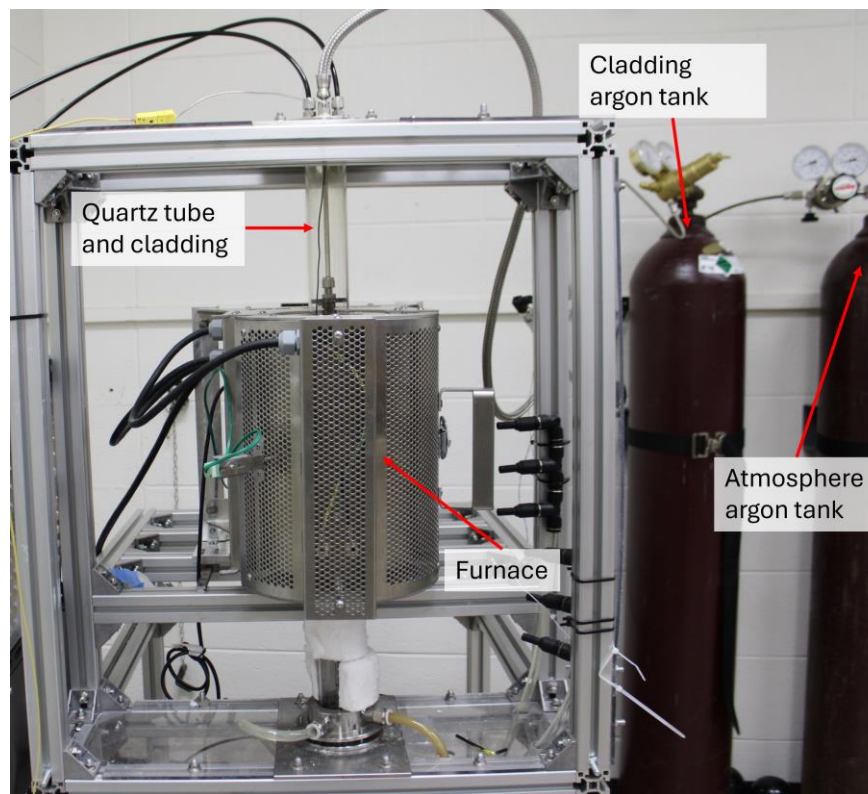


Figure 23. Single rod burst test facility used in this research.

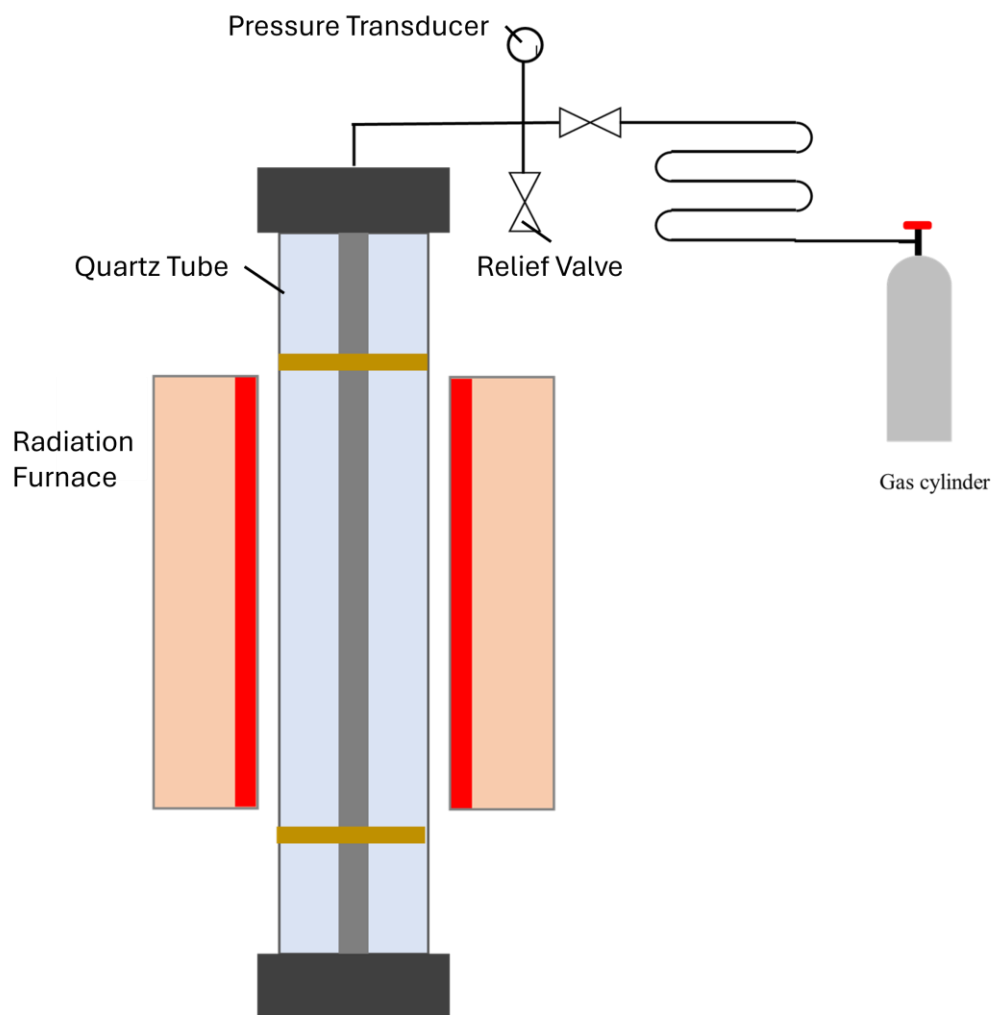


Figure 24. Schematic illustration of the single rod burst test facility showing the positioning of the cladding, quartz tube, furnaces, and argon gas supply.

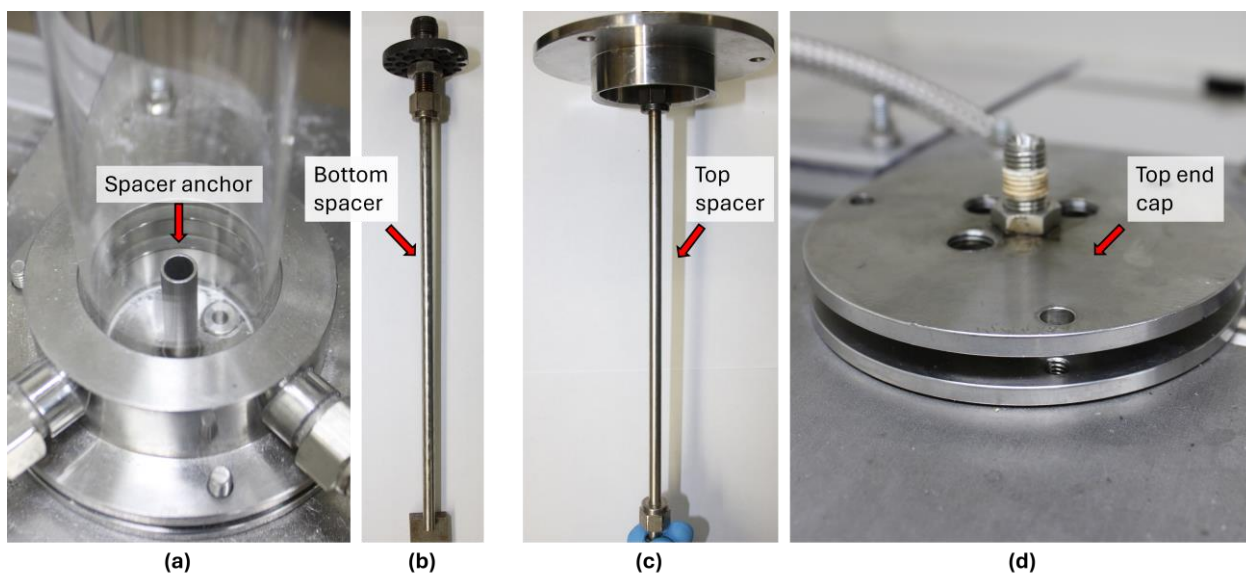


Figure 25. Cladding mount apparatus (a) spacer anchor that fits the bottom spacer of the cladding, (b) bottom spacer, (c) top spacer above the cladding that attaches to the top end cap, and (d) top end cap with apertures for gas line connections.

### 2.3.2 Cladding Tube Preparation

The as-received 38-inch long Zr-alloy cladding was cut into 7.6-inch-long sections to maximize cladding material utilization. The heating furnace in the test facility has a total height of 12 inches, with an internal uniform heating zone in the center of 6 inches. Accounting for the attachment of bulkhead fittings, the 7.6-inch size of the cladding allowed the rod's surface to be entirely contained within the uniform heating zone of the furnace. The outer surface of the as-received Zr-alloy tube was polished using 600- and 800-grit SiC abrasive paper to achieve an average surface roughness under  $\sim 0.2 \mu\text{m}$  as shown in Figure 13. Surface roughness does not substantially affect the mechanical integrity of the cladding during burst testing but was polished to preserve consistency with previous reflood testing [31].

### 2.3.3 Pre-test Assembly

Zr-alloy cladding was installed in the test facility using two main components, the bulkhead fittings and the metal end cap. The 7.6-inch length cladding was set into 316 stainless steel Swagelok bulkhead unions on each end and then is sealed air-tight using 316 stainless steel ferrules. Two attached flow spacers mitigated radial movement of the cladding during heating. The bulkhead unions were attached to two 316 stainless steel spacer rods that position the cladding directly at the center of the furnace axially. Argon gas for pressurizing the cladding and for flowing through the quartz tube to mitigate oxidation was supplied through the top and bottom of the mounted cladding by two gas tanks, respectively. Figure 26 shows the bulkhead fixtures and flow spacer on the cladding rod, as well as the gas and thermocouple connection points on the top end cap.

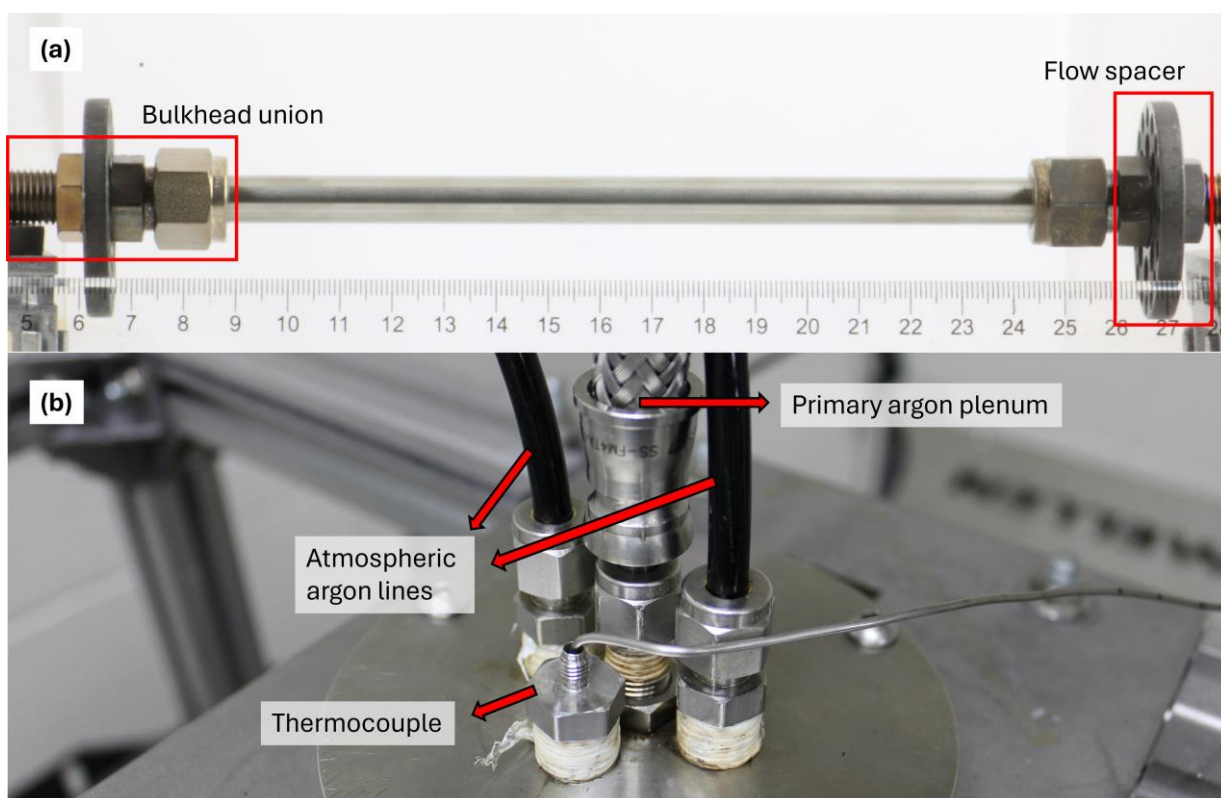


Figure 26. Photograph showing fixturing used the ballooning and burst tests for an uncoated Zr-alloy cladding tube (a) attached to two 316 stainless steel bulkhead unions with flow spacers on each end and (b) the end cap connecting the mounted cladding to gas lines and a thermocouple.

### 2.3.4 Surrogate Fuel Pellet

Aluminum oxide (alumina,  $\text{Al}_2\text{O}_3$ ) fuel pellets were used as surrogate to the uranium-dioxide fuel pellet for burst test experiments in this research. The alumina pellets were cut to an outer diameter of 7.625 mm and an axial length of 20 mm. A  $\sim 0.35\text{mm}$  gap is left between the pellets and the ID of the cladding wall to allow for gas movement and thermal expansion during heating. Alumina was selected as surrogate fuel material because it simulates the thermal behavior of  $\text{UO}_2$  without the challenges of using uranium-bearing materials in the tests. Seven to eight pellets are loaded inside of tested cladding, along with two 316 stainless steel rod internal spacers to prevent axial pellet movement and ensure the pellets are not damaged if the cladding needs to be cut post-test. An example configuration is shown in Figure 27.

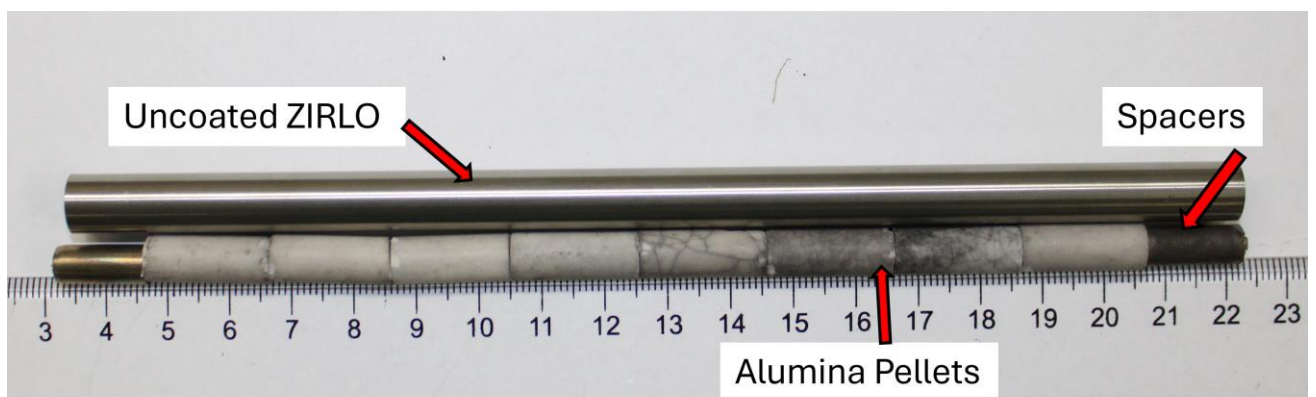


Figure 27. An uncoated Zr-alloy cladding next to the spacers and alumina pellets that are loaded into the cladding to conduct ballooning and burst tests.

### 2.3.5 Temperature and Pressure Measurement

During single rod burst testing, the outer gas temperature and internal cladding pressure were measured with a type-K thermocouple and an inline Omega Engineering PX-319I pressure transducer, respectively. The thermocouple was positioned between the quartz tube wall and the outer diameter of the cladding. Positioning the thermocouple in the gap ensured that it did not interact with the cladding, so it does not interfere with the ballooning and burst behavior. Directly welding a thermocouple onto the surface of the cladding would have introduced a confounding factor on the burst location as reported

in the literature [32]. As there were no pre-existing defects on the surface of the cladding which could cause wall strengthening/weakening and the presence of a measurement tool bonded to the cladding surface could potentially affect the rupture characteristics.

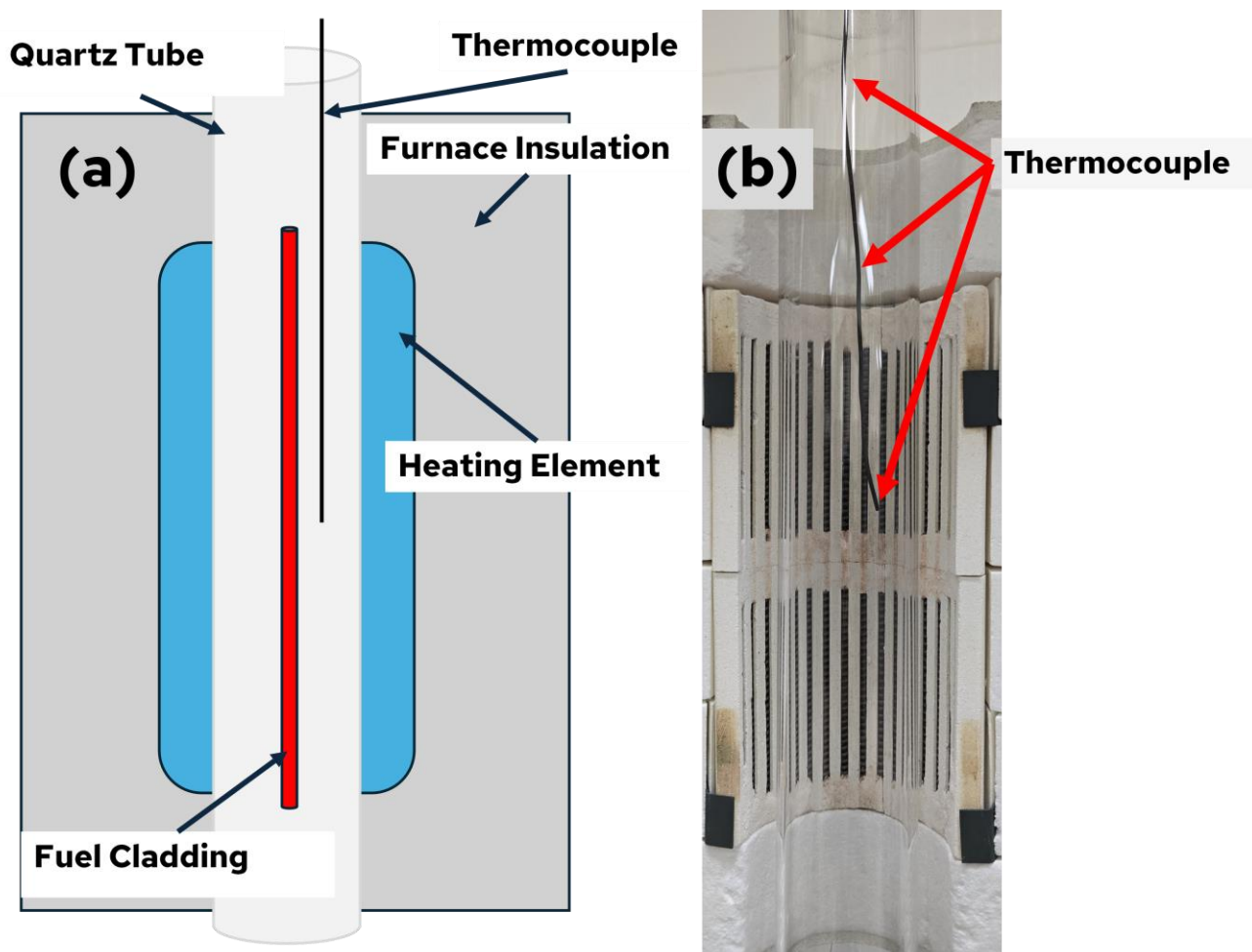


Figure 28. Position of the thermocouple inside the single rod test facility, (a) diagram of the cladding mounted inside the test facility and (b) photograph of the relative placement of the thermocouple without cladding

Cladding rupture occurred at thermal hotspots where the cladding wall is the weakest. Without the presence of argon gas flowing up through the quartz tube, the hottest temperature in the furnace would be directly in its center. However, introducing flowing argon gas could cool the bottom section of the cladding, thereby shifting the hottest temperature zone higher up on the cladding rod by a few tens of millimeters. The temperature difference from the bottom section of the cladding to the center at the start of the test is in the range of 20-40 °C but rises to a maximum of 120 °C difference ~1.25 hours later at

rupture. To account for this temperature gradient, the thermocouple was placed 60mm higher than the center of the cladding to measure the temperature in the location where burst was generally observed in our tests. This allowed us to better correlate the burst behavior to the temperature at which the burst occurred.

An Omega Engineering PX-319I pressure transducer was used to measure internal pressure, seen in Figure 29. A pressure measurement was taken at a frequency of 1 Hz. While this measurement speed cannot capture the rupture in detail, it does adequately measure the overall pressure curve during the heating process.

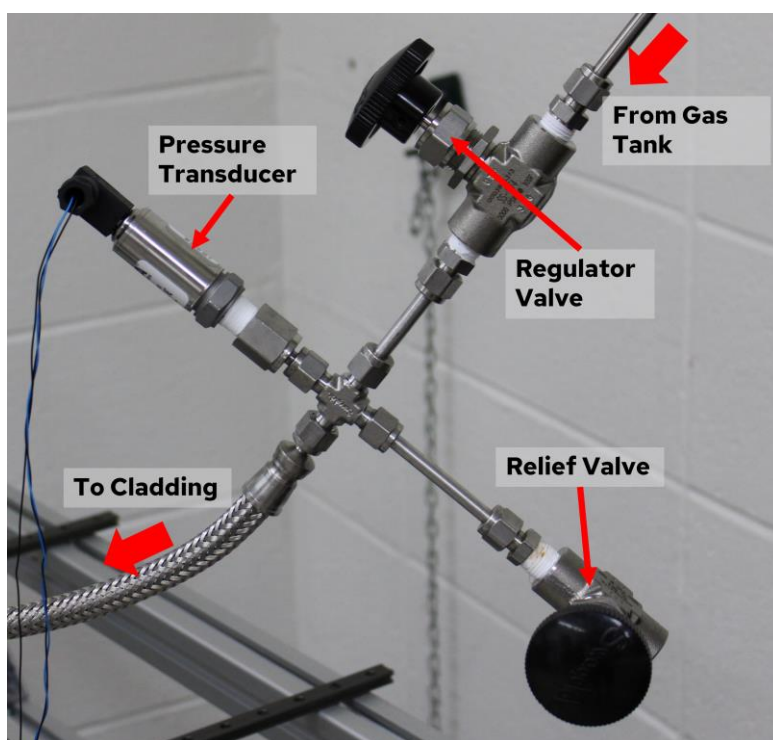


Figure 29. Pressure transducer in the test facility along with other neighboring components.

Initial internal cladding pressure was controlled to within 0.025 MPa uncertainty of the 6, 8, and 10 MPa targeted values. The regulator valve in Figure 29, in conjunction with the relief valve, was used to manually set the pressure.

### 2.3.6 Test Procedure

Performing a burst test consisted of four major stages: cladding mount assembly, leak testing, burst experiment, and post-test disassembly. Cladding mount assembly involved connecting the cut 7.6-inch-long cladding section to the bulkhead fittings. For this, a 3/8-inch 316 stainless steel nut was placed on one end of the rod along with a 316 stainless steel ferrule. The nut was hand tightened onto the bulkhead fitting, then fully tightened 1.25 rotations with a wrench. A flow separator was loosely fitted to the 1/4-inch side of the bulkhead and secured with a nut. Then, a 316 stainless steel spacer was threaded ahead of the flow separator and tightened 1.25 rotations. Surrogate fuel pellets were then loaded into the cladding, and the open end was sealed with a bulkhead fitting in the same manner as described for the other end. A top spacer attached to the end cap was threaded onto the topmost bulkhead fitting and tightened 1.25 rotations. The cladding assembly was then complete, and the end cap was screwed into the top of the facility. The length of the spacers was chosen such that when the assembly is screwed into the facility mount, the bottom spacer will rest slightly inside the spacer anchor shown in Figure 30. While the cladding is not expected to appreciably axially expand under heating, the extra space ensures that whatever expansion occurs is not restrained.

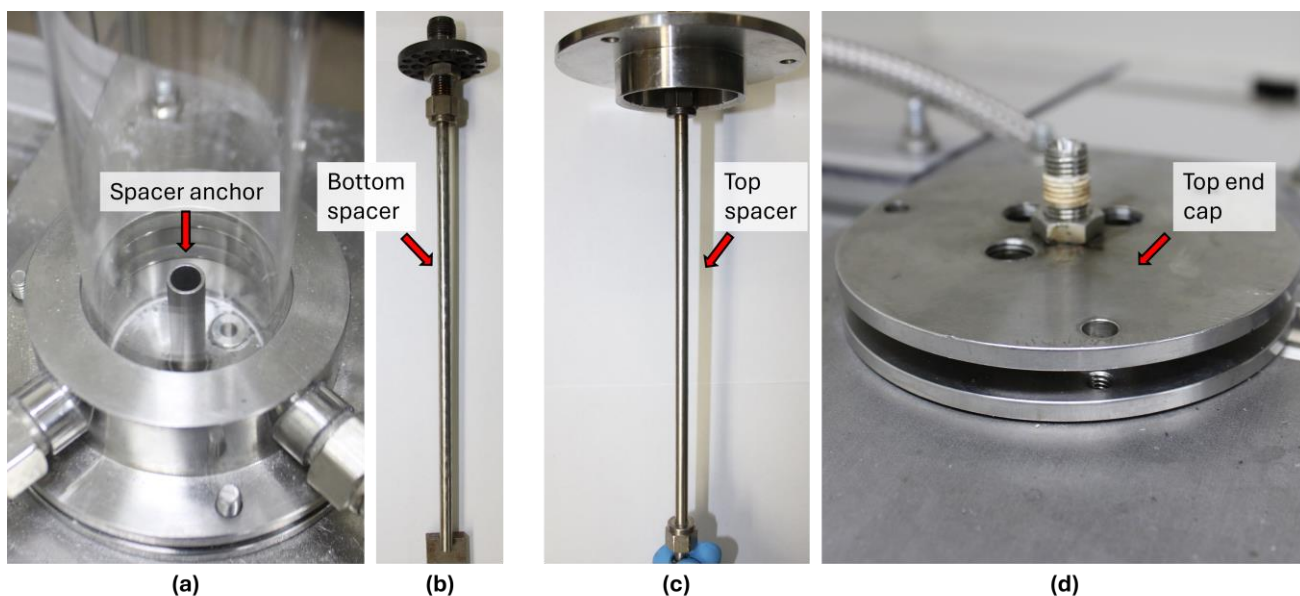


Figure 30. Images of cladding spacers and spacer mounts. (a) anchor for the bottom spacer (b) bottom spacer fitted to bulkhead (c) top spacer with end cap (d) top end cap.

With the assembly in place, the air-tight seals were tested for any potential leaks by pressurizing a fixed amount of gas in the system and observing any drops in internal pressure over a period of ten minutes. The gas plenum line contains a pressure transducer that outputs signal into a LabVIEW program. Any sustained pressure drop during a ten-minute period is likely an indicator of a leak. Snoop fluid was applied to all possible points of leakage as it bubbles at points of gas leakage. The potential leak points are shown in Figure 31. If a leak was found, the assembly was removed from the test facility and tightened again before performing another leak test. Leak testing concluded when no drop in pressure is measured by the transducer.

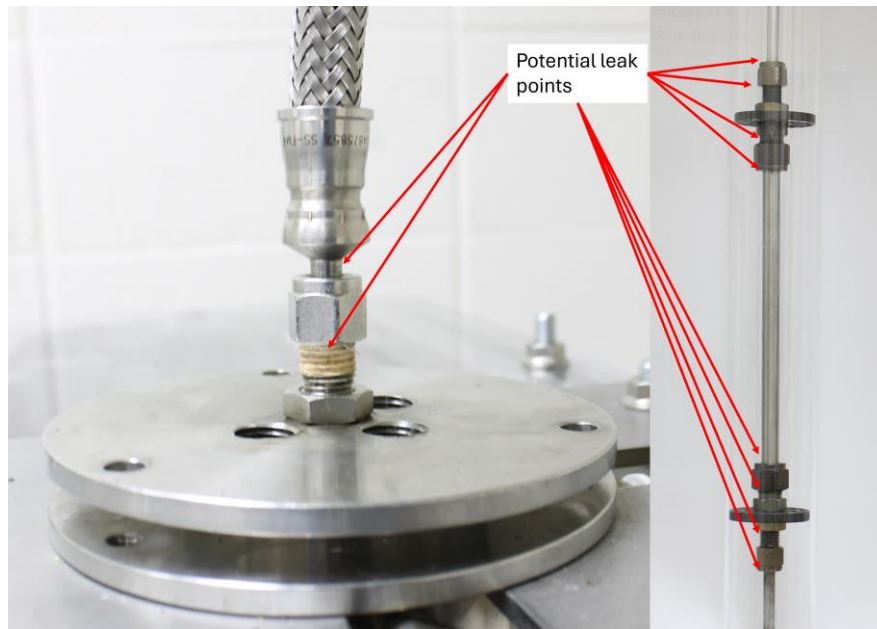


Figure 31. Potential leak points on the cladding assembly that were tested with Snoop fluid.

Burst testing was conducted when the cladding was airtight and deemed safe to be fully pressurized. The atmospheric argon gas lines were connected, and the thermocouple was inserted to approximately half the length of the cladding. An external power supply unit was used to supply power to the pressure transducer. To begin the test, the argon gas tank for pressurizing the cladding was opened. Regulator valves in-line with the transducer were progressively opened and the cladding pressure was set to a static initial value of 6, 8, or 10 MPa. When the target pressure was reached, the regulator valves were closed such that the gas was sealed inside the cladding. The primary argon tank was then isolated from the system, and the argon escape lines are connected to the end cap shown earlier in Figure 30d. The atmospheric argon gas flows from the base of the test facility upward into the escape lines and into a water tank to safely cool the gas. This water tank was also used to determine the flow rate of the atmospheric argon (i.e., the Ar flowing in the gap between the quartz tube and the cladding). A satisfactory flow rate was deemed to be achieved when large but infrequent bubbles were visible in the tank. Roughly 8-10 bubbles per second are necessary to maintain consistency between tests. With every system in place, the furnace was closed around the quartz tube and heating commenced. The furnace was set to a target temperature of 1200 °C with a linear heating rate of 10 °C/s. Cladding rupture

typically occurs under the 800 °C range, so the 1200 °C target temp is to ensure the furnace heating rate does not slow down towards the end of the test. The furnace was turned on, and data collection began when the cladding reaches a temperature of 50 °C to ensure consistency between tests. Data collection ends when the cladding has ruptured, and the furnace is turned off. Argon gas still flows through the quartz tube to aid in cooling and to prevent post-burst oxidation.

The cladding was removed when the facility reached room temperature. Both spacers as well as the surrogate fuel pellets were also removed. A low-speed diamond saw operating at 300 RPM was used to cut the ½ inch off each end of the cladding to remove the Swagelok bulkheads. The cladding was rinsed with DI water and left to dry.

### 2.3.7 Test Matrix

Burst tests were conducted for the uncoated and Cr-coated Zr-alloy cladding sections using three coating deposition approaches, totaling 14 ruptured cladding rods. The initial internal pressure and type of cladding were the two experimental variables. Various internal pressures represent the various fuel burnup since higher fuel burnup increases the internal cladding pressure due to an increase in fission gas production [33]. For ATF burnups between 62 and 80 GWd/MTU, the typical internal cladding pressure ranges between 6-10 MPa, thus this range was chosen to conduct burst tests targeting the high burnup fuel.

Table 3. Test matrix of the single rod (7.6” length) burst test facility for burst testing of Zr-alloy. \* denotes a reproducibility test.

<b>Surface</b>	<b>Initial Pressure (MPa)</b>
<b>Uncoated</b>	6
	8*
	10

<b>CS (He)</b>	6
	8
	10
<b>CS (N2)</b>	6
	8*
	10
<b>PVD</b>	6
	8
	10

### 3 Results and Discussion

#### 3.1 Post-quench Ductility

##### 3.1.1 Ring Compression Testing

Ring Compression Testing (RCT) was performed to assess the post-quench ductility and strength of uncoated and Cr-coated Zr-alloy cladding tubes. Figure 32 shows the samples taken from PVD Cr coated cladding sections after quenching from 1200 °C. An example cross-sectional SEM image of a through-wall failure is shown in Figure 33, which was quenched uncoated Zr-alloy cladding at 1200 °C.

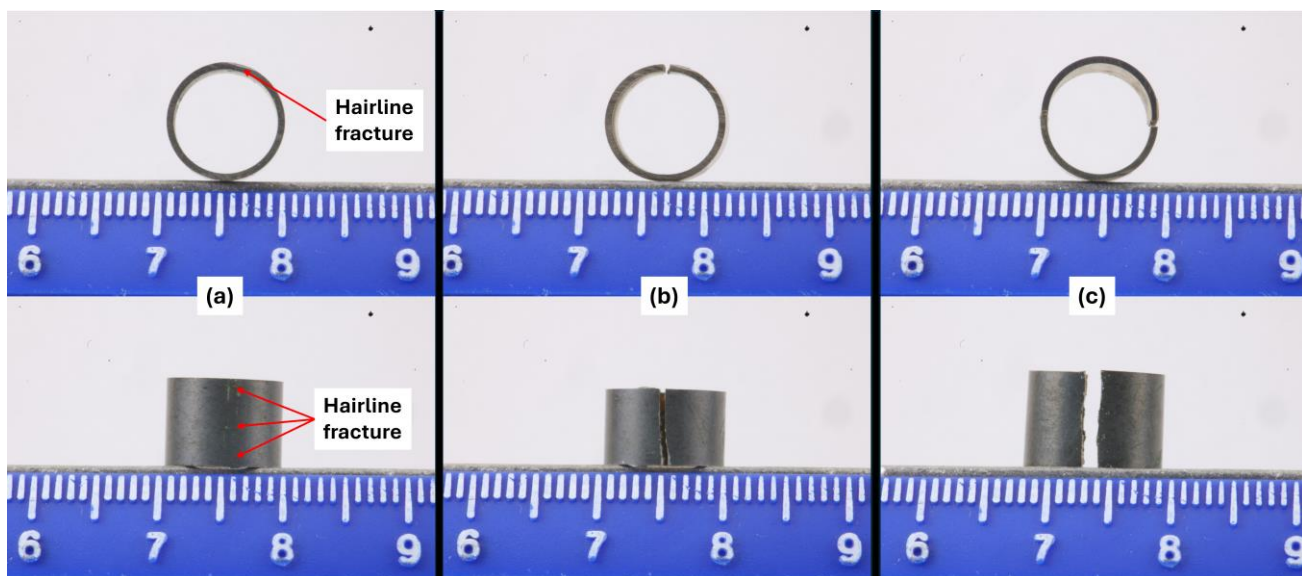


Figure 32. Intensity of cracking behavior of 1200 °C post-quench PVD Cr-coated Zr-alloy. (a) Section 3, thin closed hairline fracture across entire wall (b) section 2, open fracture (c) section 4, split fracture.

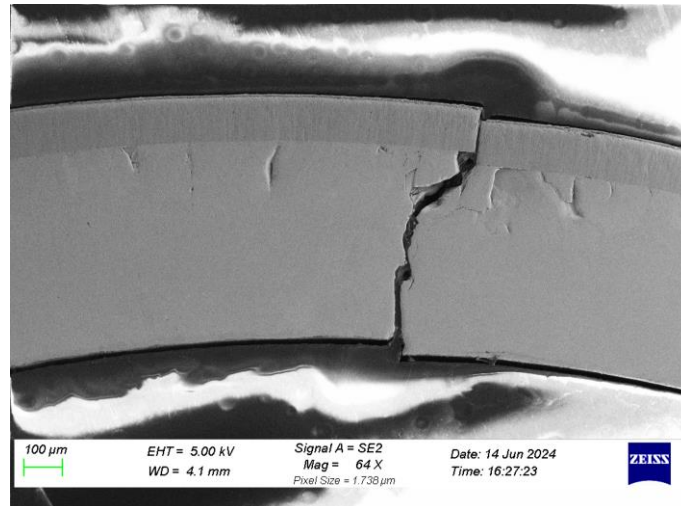


Figure 33. Cross-sectional SEM image of a post-RCT through-wall fracture in an uncoated Zr-alloy cladding that was quenched during the reflood test from a temperature of 1200 °C.

The load-displacement behavior was generally similar for the Cr-coated and uncoated cladding samples quenched from the temperatures in the range of 600C-1000 °C with the maximum load in the range of 350 – 400 N, as shown in Figure 34. However, drop in maximum load compared to their untested (unquenched) counterparts varied. For PVD Cr-coated cladding, the drop was about 200N and for cold spray Cr coated cladding it was 400N, however for the uncoated cladding sample the drop was quite small and in the range of 50 to 100N. This decrease is attributed to microstructural changes induced during the high temperature exposures. The high load for the CS Cr coated sample at 780 N is particularly noteworthy and is indicative of the constraining effect of these coatings through compressive pre-stress. The focus of this discussion will be mainly on the samples quenched after reflood test at 1200 °C, the criteria for activation of emergency core cooling system (ECCS) during the LOCA accident.

For uncoated cladding samples quenched at 1200 °C, the loading was terminated prematurely due to through wall failure at ~220N. This sample experienced severe oxidation during reflood testing as shown in the cross-sectional SEM image in Figure 35, and through-wall cracking at the point of contact with the loading platen as shown in Figure 33. In addition, the loading slope during elastic deformation for this sample was 1.6 times higher than the loading curves for the sample subjected to other

temperature conditions of reflood tests. This is likely due to significant diffusion of oxygen into the cladding which significantly changed the composition of the Zr-alloy over a significant thickness of the cladding, and consequently a change in elastic modulus. In addition to the oxygen-induced embrittlement, the reduction in effective wall thickness due to the consumption of the metal by the growing oxide layer may be another contributing factor in the premature failure of the cladding.

As shown in Figure 34b, the presence of a 30  $\mu\text{m}$  thick (5% of the original cladding thickness) CS Cr-coating notably increased the maximum sustainable load compared to the uncoated cladding before the quenching (i.e., in the as-received and as-deposited conditions). The post-quench sample results can be explained based on oxidation which induces brittleness and reduces the effective wall thickness and the constraining effect of the cladding imparted by the coating. Again, for cladding samples quenched from reflood tests at 1200  $^{\circ}\text{C}$ , the CS Cr-coated cladding fails at a significantly higher load ( $\sim 780$  N) and displacement ( $\sim 1.5$  mm) compared to the uncoated sample. This effect is largely attributable to the dramatic reduction in the oxidation of the underlying Zr-alloy cladding due to the presence of the Cr coating in the context of both effective wall thickness and the oxygen-induced embrittlement of the substrate. It is also interesting to note in Figure 34b that the untested CS Cr-coated cladding also shows a similar maximum load at 2 mm displacement than its counterpart quenched from 1200  $^{\circ}\text{C}$ , even though it did not fail. This is again evidence to the constraining ability of the CS Cr-coating which also is in a state of high compressive stress inherent to cold spray deposition process, in the as-deposited condition.

The effectiveness of Cr coating in dramatically mitigating oxygen ingress into the cladding is also borne out in SEM-EDS analysis of the cross-sections of the samples that show the diffusion profile of oxygen into the cladding (Figure 36). The results show EDS line scan from the outer (OD) to the inner (ID) diameter of the cladding samples with the total scan length of 600  $\mu\text{m}$ . Fifty points along the scan path were measured with a dwell time of 65 seconds each. Uncoated Zr-alloy (Figure 36a) showed extensive oxidation during reflood testing and developed a thick oxide layer of about 110  $\mu\text{m}$  in thickness. Minor oxidation was observed at the ID boundary due to the internal cladding air environment, but this surface was not in contact with water during the test and thus did not exhibit an

appreciable oxide layer. At the interface of the stoichiometric oxide layer and metallic Zr-alloy, the oxygen concentration dropped from the stoichiometric value of about 66% oxygen to about 30% oxygen. This marks the onset of the region where oxygen is dissolved as a solid solution in the Zr-alloy. In this solid solution region, oxygen penetrated an additional 200  $\mu\text{m}$  (i.e., internal oxidation layer) before stabilizing between 15-20%. The ID interface did allow some oxygen to diffuse through but was not considered to be a contributing factor to the ductility of the substrate. In contrast, the CS Cr-coated Zr-alloy (Figure 36b) exhibited excellent resistance to oxidation and practically eliminated oxygen diffusion into the underlying Zr-alloy. Of the 30  $\mu\text{m}$  Cr-coating thickness, approximately 10  $\mu\text{m}$  was oxidized to  $\text{Cr}_2\text{O}_3$ . A Cr-Zr interdiffusion layer  $\sim 3$   $\mu\text{m}$  in thickness was observed at the interface of the CS Cr coating and the Zr-alloy substrate. PVD Cr-coating on Zr-alloy (Figure 36c) conferred oxidation resistance as well, but there was penetration of oxygen into the Zr-alloy to a depth of about 25  $\mu\text{m}$ . The majority of the 9  $\mu\text{m}$  thick Cr PVD layer was consumed by the formation of  $\text{Cr}_2\text{O}_3$ .

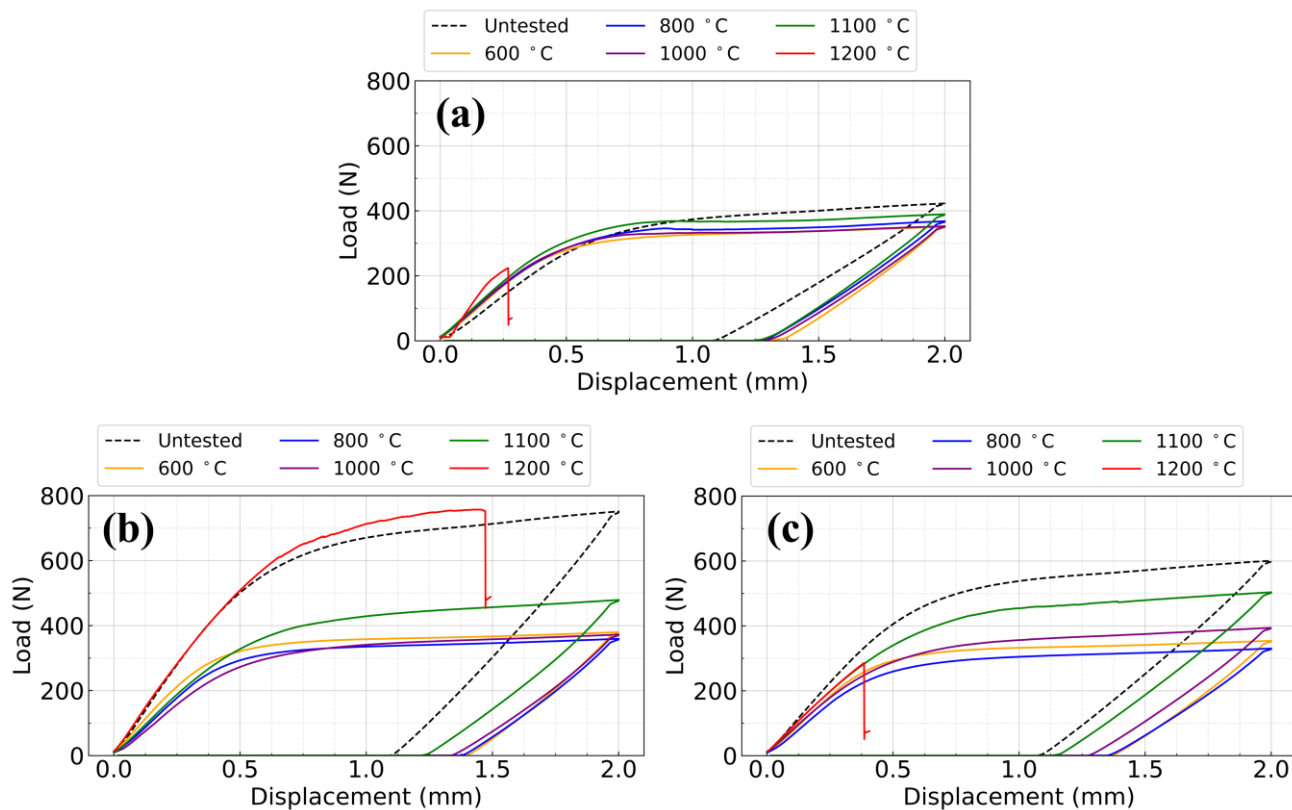


Figure 34. Load-displacement curves for (a) uncoated (b) CS (He) Cr-coated and (c) PVD Cr-coated ZIRLO.

Each plot contains five loading curves for temperatures between 600-1200 °C.

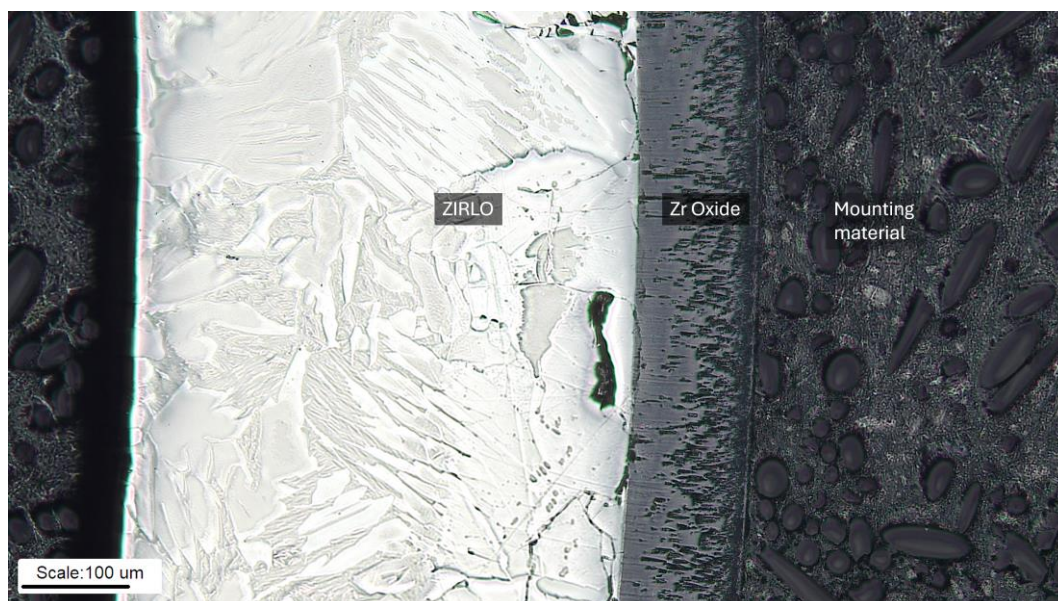
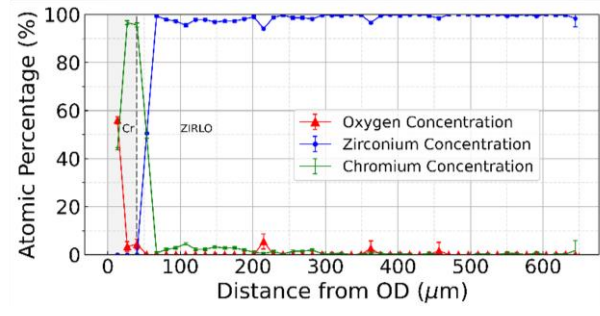
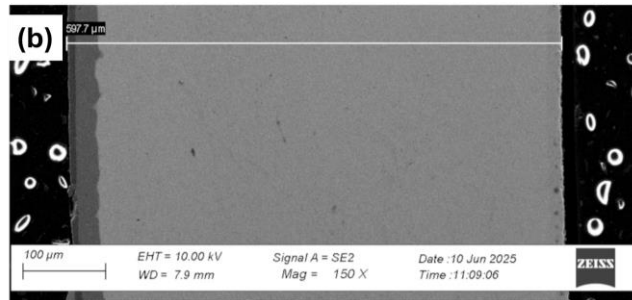
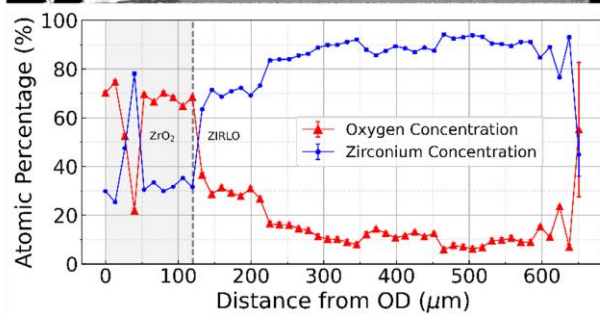
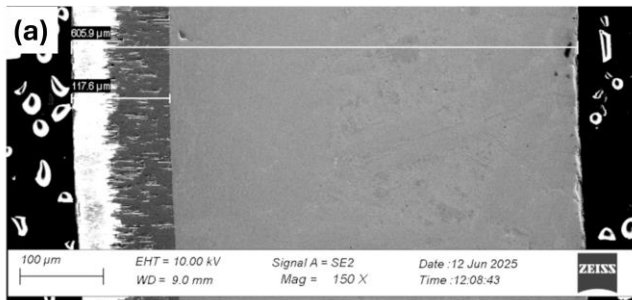


Figure 35. Cross-sectional optical microscopy image of an uncoated ZIRLO cladding sample quenched at 1200 °C. A thick stoichiometric Zr oxide layer is observed.



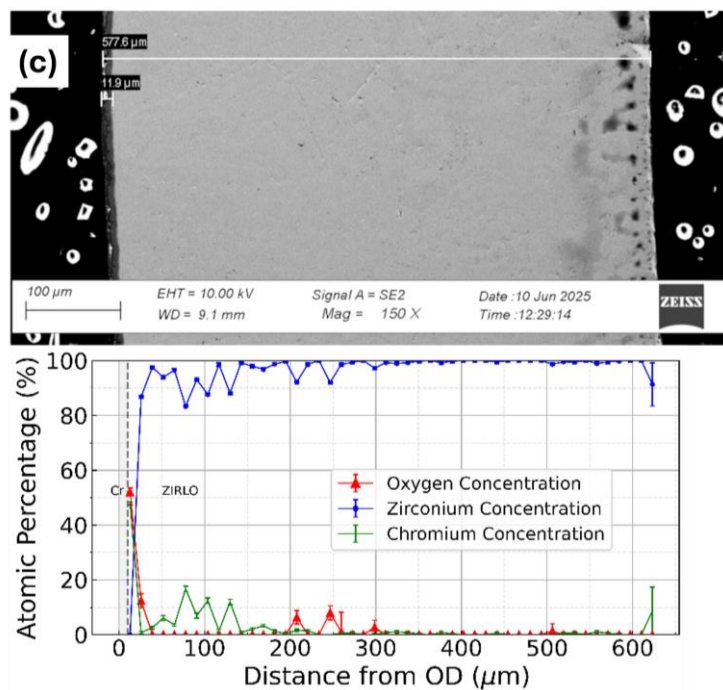


Figure 36. Cross-sectional SEM images and EDS line scans of samples after quenching from reflow tests at 1200 °C (a) uncoated Zr-alloy, (b) CS Cr-coated Zr-alloy, and (c) PVD Cr coated Zr-alloy.

As shown in Figure 37, for PVD Cr coated (10 μm) cladding with a drastically different coating microstructure compared to the cold spray coating, the results of RCT for samples quenched from 1200 °C showed a behavior quite similar to the uncoated cladding, with premature through-wall failure occurring at a load of about 300 N (compared to about 220 N for the uncoated cladding). The PVD coatings have a columnar microstructure, which may tend to separate out at the intercolumnar boundaries under the application of a hoop stress by the thermal expansion at 1200 °C. These intercolumnar regions may also act as pathways for oxygen diffusion supplying the oxygen to the underlying Zr-alloy substrate. This combined with the relatively fragile nature of the PVD coatings and lower adhesion strength compared to cold spray coatings provide little benefit in post-quench mechanical behavior for samples exposed to 1200 °C. However, it still retained a higher maximum load and displacement than uncoated Zr-alloy. Figure 37 summarizes the results of the load-displacement plots for the Cr coated and uncoated cladding tubes after quenching from 1200 °C reflow experiments.

It should be noted that all cladding types exhibited through wall cracking, but at different loads and displacement levels, showing the best post-quench ductility with the CS Cr-coated Zr-alloy cladding.

Similar effects are observed for CS Cr-coated cladding tested at 1100 °C, where the maximum load increased while still maintaining wall integrity without through-wall cracking. The presence of a Cr coating mitigated the diffusion of oxygen into the Zr-alloy substrate as shown in Figure 36. In addition, the 1200 °C test case failed much later than the PVD Cr-coated and uncoated Zr-alloy as shown in Figure 37. It was possible that Cr diffused through the Cr-Zr interdiffusion layer and hardened the Zr substrate [34]. For samples tested at temperatures in the range of 600-1000 °C, the behavior of the uncoated and CS Cr-coated samples is quite similar.

PVD Cr-coated Zr-alloy had a much lower Cr coating thickness (10 µm) than the CS Cr-coated Zr-alloy and thus did not appreciably benefit from mechanical reinforcement of the Cr-coating. The average untested loading curve was ~600 N lower than the CS Cr-coated Zr-alloy test cases, and the 1200 °C sample did not reach the same maximum load before failing due to the brittleness. The maximum loads for the 1100C and 1200C test cases were both slightly higher than the equivalent temperature cases for uncoated Zr-alloy.

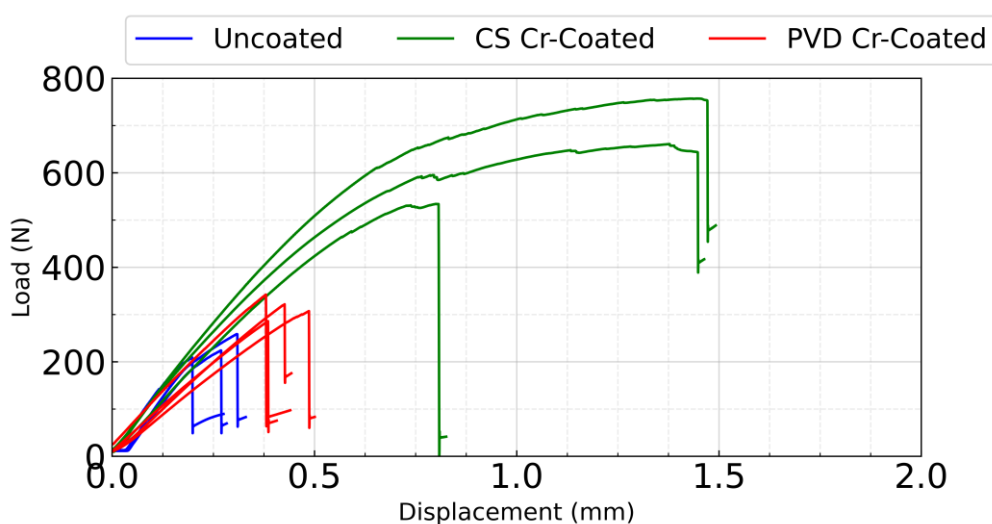
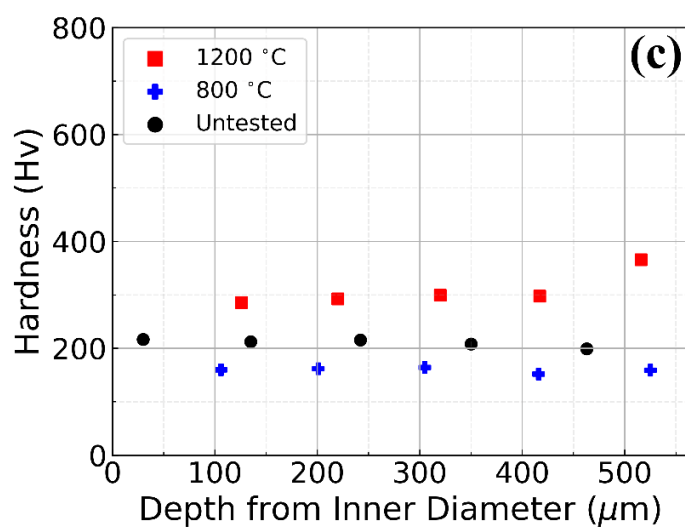
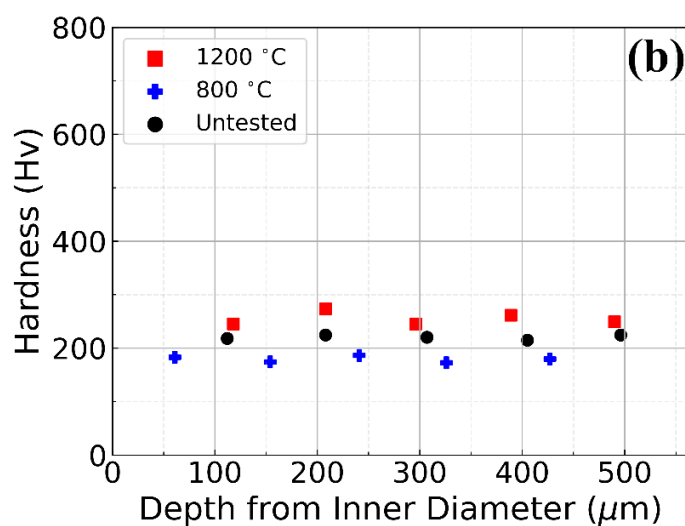
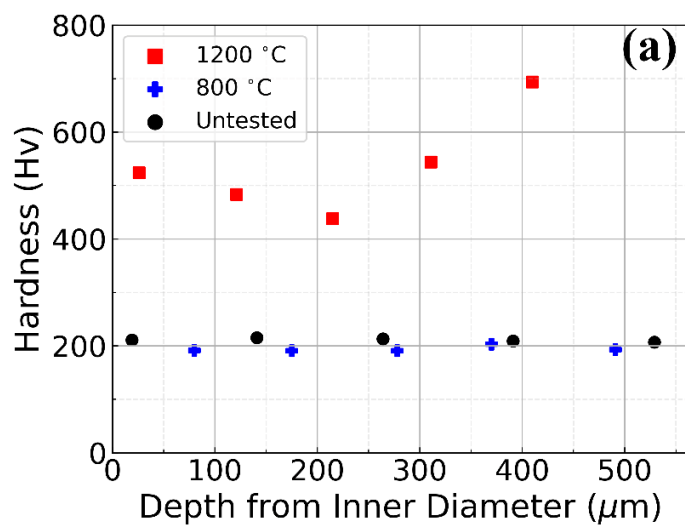


Figure 37. Load-displacement curve of uncoated and Cr-coated ZIRLO quenched in the reflood tests from a temperature of 1200 °C.

To gain additional insights into the mechanical behavior displayed in the RCT, microhardness testing (Vickers hardness at 50g load) was performed on each cladding type (uncoated, Cr cold spray coated, and PVD coated) as a function of distance along the cladding wall thickness, after mounting and polishing the samples in cross-section. The results are shown in Figure 38, where the hardness measurements are shown for (a) uncoated, (b) cold spray Cr-coated, and (c) PVD Cr-coated. Each figure shows hardness data for samples in the following conditions: untested, after quenching from 800 °C , and after quenching from 1200 °C . The hardness of the Zr-alloy substrate does not change after the 800 °C quench as inferred by comparison with the untested sample in each case. At 800 °C quench temperature condition and exposure time during reflood test, the oxygen diffusion into the Zr-alloy substrate was not significant to change the hardness to any significant depth. It is also important to note that the untested samples in each case show similar hardness for the Zr-alloy substrate, suggesting the coating process itself did not alter the hardness (and microstructure) of the underlying substrate. However, for the sample quenched from reflood tests at 1200 °C, the hardness of the underlying substrate increases significantly due to the diffusion of oxygen into the cladding. This is supported by the observation that hardness in the region close to the ID of the cladding is high and decreases as one proceeds into the cladding and once again increases in the regions closer to the OD of the cladding (Figure 38 (a)). In short, the hardness profile matches or mimics the oxygen diffusion profile. For the CS Cr-coated cladding, the hardness does not change significantly across the cladding wall thickness given that the Cr coating serves as a diffusion barrier to any ingress of oxygen into the underlying Zr-alloy cladding (this is also borne out in the oxygen diffusion profile for this sample discussed earlier). For the PVD coated samples, there is a slight elevation in hardness particularly in the regions closer to the OD. This is also consistent with some diffusion or permeation of oxygen through the PVD Cr-coating's columnar structure and its accumulation in the Zr-alloy cladding just below the Cr coating-substrate interface. Thus, the higher sustainable loads observed in the 1200 °C quenched CS Cr-coated samples appear to come from the constraining effect of the coating and the oxidation-resistance of the coating. This is not the case for the PVD Cr coating and obviously non-existent for the uncoated

cladding samples. Figure 38d summarizes the hardness profiles for the three types of samples after the 1200 °C quench test.



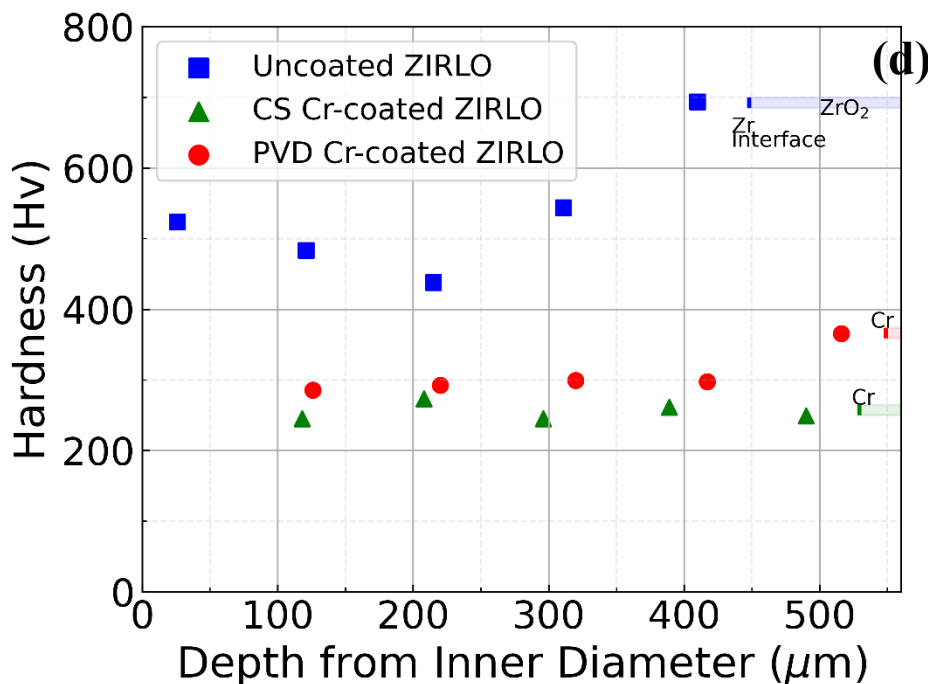


Figure 38. Vickers microhardness measurements across the cross-section of the cladding wall thickness: (a) uncoated, (b) Cr cold spray coated, (c) Cr PVD coated, (d) compilation of data for the 1200 °C quench samples for the three types of cladding samples.

## 3.2 Burst Behavior of the Cr-coated Zr-alloy Cladding

### 3.2.1 Burst Temperature and Pressure

Burst tests were conducted for the Zr-alloy in uncoated condition and after being Cr-coated with three processes (2 cold spray types and 1 PVD), totaling 12 ruptured claddings (three replicates each cladding type at 8 MPa). The initial internal pressure and type of cladding were two experimental variables in these burst test experiments. Each test began with an initial heating phase that warmed the heating furnace until it reached a stable heating rate. Pressure and temperature measurements were initiated when the temperature inside the furnace reached 50°C. Testing was concluded upon cladding rupture, as determined by the sudden drop in the internal pressure rapidly to atmospheric pressure. The temperature associated with cladding rupture (i.e., perforation) is defined as the burst temperature and the corresponding pressure at the time of the burst is defined as the burst pressure in this study. For example, Figure 39 shows a typical data for uncoated Zr-alloy where the burst temperature of ~ 700 °C

and the burst pressure of  $\sim 8.4$  MPa were measured. The results show that burst pressure can be lower than the peak pressure due to the ballooning phenomenon.

Heating rate was maintained constant during the test, as shown in Figure 39. The interval between 0-2000 seconds for the pressure curve was characterized by a mostly constant heating rate. During this period, the internal free volume remained constant, and pressure increased at a constant rate. After approximately 2000 seconds, the pressure increased at a slower rate due to the ballooning of the cladding which provides more volume and is associated with plastic deformation of the cladding.

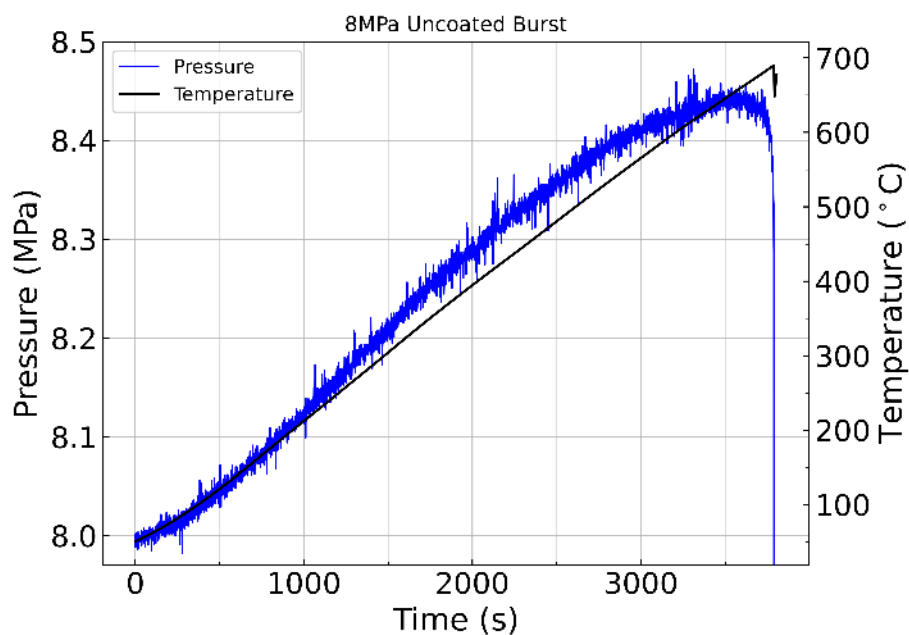


Figure 39. Pressure and temperature curves of an 8 MPa uncoated Zr-alloy burst test.

The burst test results were also examined in the context of values reported in literature, however such a comparison should be viewed in the context of differences in the experimental characteristics of each facility, with the foremost influential factor being the furnace heating rate, and in the case of coated claddings, and the parameters used for the coating process. Rapid heating introduces non-uniform thermal distribution along the cladding surface, creating hotspots that may preferentially rupture relative to the surrounding material. The Chapman correlation was developed to explain the scatter in burst temperatures between different test facilities considering the heating rate and the hoop stress. It is an

empirical correlation bridging the engineering hoop stress of the tested cladding and its heating rate to the burst temperature [30]. The conversion from differential pressure ( $\Delta P$  (MPa)) to hoop stress ( $\sigma$  (MPa)) utilized the thin-wall approximation to eliminate geometry-dependent stresses. The mid-wall diameter ( $d$  (mm)) and the wall thickness ( $t$  (mm)) were used in the approximation as shown in Eq. (2).

$$\sigma = \frac{d}{2t} \Delta P \quad (2)$$

A compilation of burst test data from Oak Ridge National Laboratory, Battelle Columbus Laboratories, Kernforschungszentrum Karlsruhe (Germany), and the Japan Atomic Energy Research Institute is shown in Figure 40 [30]. There was notable variation in burst temperature for similar hoop stresses between each laboratory's data, although a visible trend was that the burst temperature decreased with increasing hoop stress. The difference in burst temperatures between different tests was mainly due to the different heating rates used in these various experimental facilities, which ranged from 28 °C/s to ~1 °C/s [30].

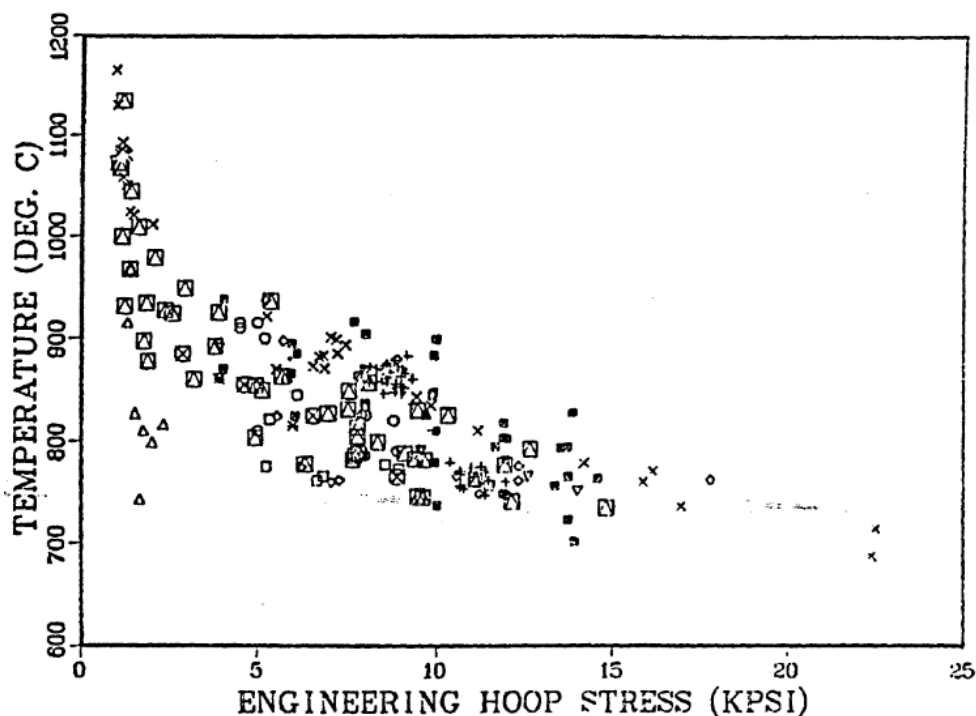


Figure 40. Rupture temperature as a function of engineering hoop stress for Zircaloy cladding taken from various sources: Oak Ridge National Laboratory, Battelle Columbus Laboratories, Kernforschungszentrum Karlsruhe (Germany), and the Japan Atomic Energy Research Institute [6].

The Chapman correlation (Eq. 3) was developed based on the data in Figure 40. This correlation incorporates the effect of the heating rate. The variable “H” was introduced as the ratio between the actual heating rate to the reference heating rate of 28 °C/s. It was assumed that the heating rate saturated at 28 °C/s such that “H” varied between 0 and 1. The burst temperature depends only on the heating rate and the engineering hoop stress in Chapman’s correlation without consideration of the cladding material. Thus, this motivated us to investigate the effect of ATF cladding designs on the burst behavior.

$$T = 3960 - \frac{20.4\sigma}{1 + H} - \frac{8,510,000\sigma}{100(1 + H) + 2790\sigma} \quad (3)$$

The heating rate used in the single rod test facility in the present study was 0.16 °C/s. While such a low heating rate is not typical of in-reactor heating rates [24], it still warranted investigation as the later

phase of heating during a LOCA drops to a rate of 2-5 °C/s. Using 0.16 °C/s, “H” was calculated to be 0.00595. Figure 41 shows the results of this study’s burst testing for the three initial pressures at 6 MPa, 8 MPa, and 10 MPa with the Chapman’s correlation at 28 °C/s and 0.16 °C/s. This data is plotted alongside burst test data from ORNL with a heating rate of 28 °C/s [30]. Chapman only utilized uncoated Zr-alloy in the correlation, and thus comparison to Cr-coated cladding was not considered for goodness-of-fit. Burst temperatures for uncoated Zr-alloy at a heating rate of 0.16 °C/s was overestimated by the Chapman correlation by a maximum 10%. Stochastic variance in burst temperature between tests at the same initial pressure was expected. Deviation from the Chapman correlation did not appear to offer behavior vastly different from other experiments. With such a low ramp rate, it was possible that the additional time allowed for stress relaxation in the cladding which led to larger ballooned regions and longer times until rupture. Chapman accounted for ramp rates below 10 °C/s but 0.16 °C/s of heating rate is below the applicable range of the Chapman correlation. In addition, many of the experiments in the correlation utilized different Zr-alloys (e.g., Zircaloy-4) than the Zr-alloy used in the present study. Thus, while the Chapman correlation shows overprediction of the burst temperatures of uncoated Zr-alloy, it is still showing a relatively good agreement with our uncoated Zr-alloy data even with very low heating rate. Nonetheless, this exercise provided the groundwork for other models to predict burst temperatures.

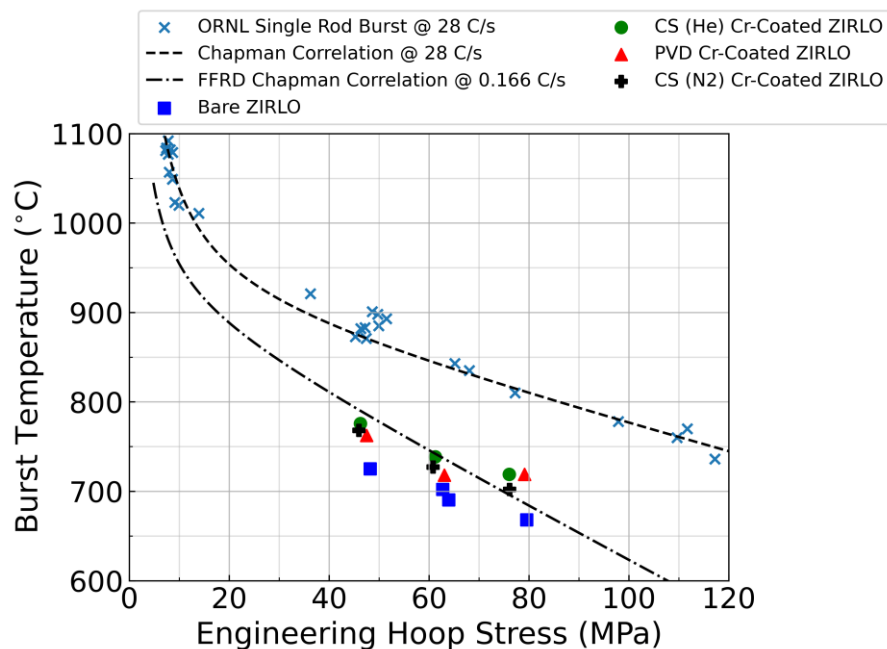


Figure 41. Burst temperatures of all four cladding types: uncoated Zr-alloy, CS (He), CS (N<sub>2</sub>), and PVD Cr coated Zr-alloy. The burst pressures of each cladding were converted into hoop engineering stress.

It was hypothesized that Cr-coatings can affect the failure mechanism of the cladding. It has been noted, for example, that in ring tensile testing (RTT), the coatings provided mechanical reinforcement that delayed plastic deformation of the cladding [35]. Studying the behavior of Cr-coated cladding in a simulated LOCA scenario introduces the added complexity of thermo-mechanical interactions and annealing effects. Pressurizing cladding and rupturing it under increasing temperature allowed for a relatively more prototypical examination of how CS and PVD Cr-coatings constrained the deformation of the Zr-alloy cladding.

### 3.2.2 Burst Temperature

Based on our burst test results (Figure 42), the presence of a Cr-coating, regardless of coating type, enhanced the burst temperature of cladding across all ranges of initial pressures relative to uncoated Zr-alloy cladding. CS (He) shows the highest burst temperatures across all pressure ranges averaging a rise of ~50 °C when compared to uncoated cladding. CS (N<sub>2</sub>) and PVD followed a similar trend for 6 and

8 MPa, respectively, although PVD exhibited a comparable burst temperature to CS (He) for 10 MPa, as shown in Table 4.

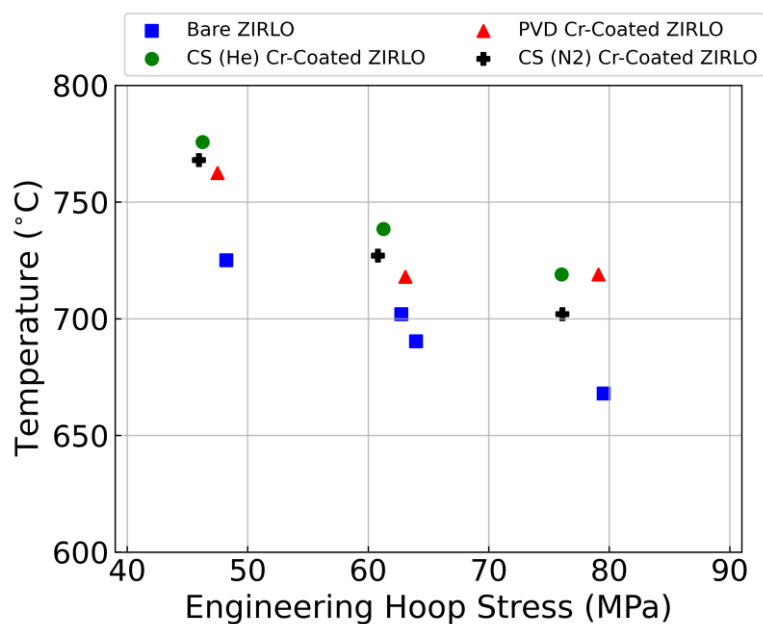


Figure 42. Burst temperature of uncoated and Cr-coated cladding as a function of the engineering hoop stress.

Table 4. Measured burst temperature and engineering hoop stress of the four types of claddings tested: uncoated, CS (He), CS (N<sub>2</sub>), and PVD Cr-coated Zr-alloy.

Coating Type	Engineering Hoop Stress (MPa)	Burst Temperature (°C)
Uncoated	48.23	725
	63.97	690
	79.55	668
CS (He) Cr-coated	46.26	775
	61.27	738
	76.05	719
CS (N <sub>2</sub> ) Cr-coated	45.96	768

	60.82	727
	76.12	702
PVD Cr-coated	47.50	762
	63.08	718
	79.11	719

Cr-coatings can provide some degree of mechanical reinforcement to the Zr-alloy cladding, however, the mechanism and degree of reinforcement is dependent on the nature of the coating and its deformation and rupture behavior. CS Cr-coatings use high velocity particle impact solid-state deposition to induce both mechanical and metallurgical bonding of the Cr particles to a substrate, resulting in mechanical interlocking and a work-hardened coating. Additionally, helium carrier gas yields higher particle velocities than nitrogen carrier gas and accentuates these phenomena. For this reason, the nitrogen cold spray coatings exhibit higher ductility. The interfacial bonding in cold spray coatings is sufficiently high and did not result in any delamination from the substrate even after the ballooning and burst. Typically, CS coatings need to be deposited thicker than their final target depth, followed by polishing to a lower thickness. CS (He) was deposited to thickness of  $\sim 75 \mu\text{m}$  while CS (N<sub>2</sub>) was deposited to thickness between 50-60  $\mu\text{m}$ . A deposited layer thickness of 60  $\mu\text{m}$  or higher for either CS coating yields a stronger adhered coating when polished down to 30  $\mu\text{m}$ . Polishing also removes the weakly adhered top layer of CS coating, which is an intrinsic feature of the CS process. PVD Cr-coatings used vapor deposition to deposit a thin layer ( $\sim 9 \mu\text{m}$ ) of Cr onto the surface of the Zr-alloy, creating a columnar grain structure. Interfacial adhesion occurs by energetic ion induced mixing at the interface which extends to a maximum of few tens of nanometers. Figure 43 shows cross-sectional SEM images of Cr coating deposited by CS and PVD processes.

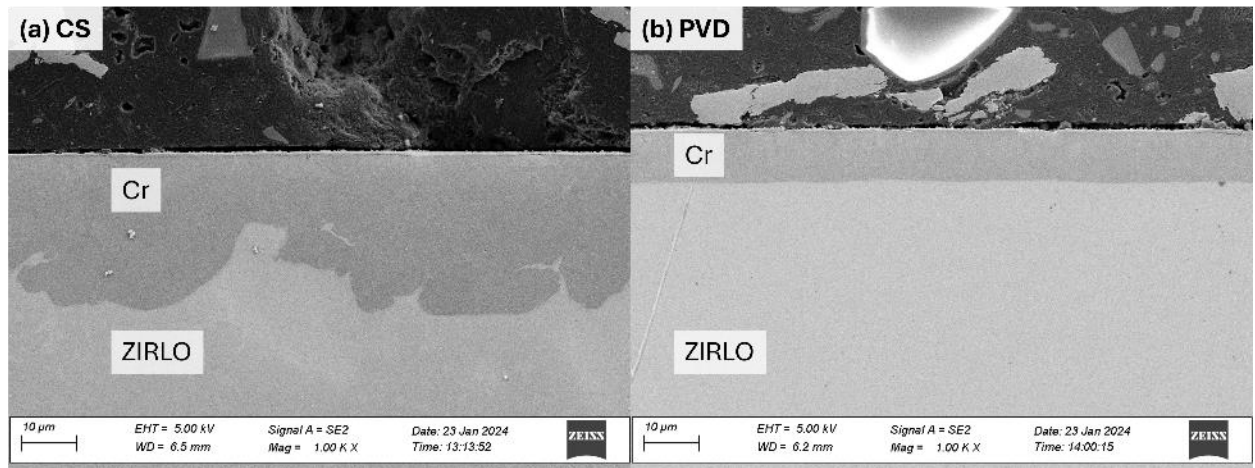


Figure 43. Cross sectional SEM of (a) CS (He) and (b) PVD Cr-coated Zr-alloy cladding.

### 3.3 Cr-coating Deformation and Rupture Behavior

Stress relief of the Zr-alloy substrate occurred through cracking of the Cr-coatings during the heating phase of the burst test. Above 400 °C, the Zr-substrate and Cr-coatings start to experience annealing effects as seen in previous post-quench ductility analysis after reflood testing. With increasing temperature, Zr-alloy cladding wall became softer the internal pressure also increases. Additionally, the stress on the Cr-coating from the expanding Zr-substrate also increased due to the difference in the thermal expansion coefficient between the Zr and Cr. This fracture behavior can cause coatings to crack, creating “islands” of Cr. Figure 44 compiles images of the twelve distinct burst tests across the three pressure ranges. The burst opening morphology varies depending on the Cr deposition method as shown in Figure 45, and the frequency of the cracks, width and smoothness of the Cr-island edges varies depending on the Cr deposition method as shown in Figure 44. Cladding ruptured with an initial pressure of 6, 8, and 10 MPa. Coating cracking was most visible in the CS Cr-coated cladding. Striation patterns were clearly visible around the burst region of the CS (He) and CS (N<sub>2</sub>). Cracking was also present on the PVD Cr-coated claddings but was not readily seen because of the finer size scale of cracks. Of particular note is the small rupture size observed for the CS N<sub>2</sub> coating likely caused by the formation of a network of micro-scale cracks propagating along the inter-particle boundaries.

Cladding oxidation was mitigated by purging the test facility with argon gas during testing. However, some oxidation was present as evidenced by mild changes in the color of the surfaces of cladding samples. Given the duration of the test (~1.5 hrs), only a very thin oxide layer formed at the surface as confirmed by cross-sectional SEM imaging, but too thin ( $< 1 \mu\text{m}$ ) to measure accurately. It was therefore reasonable to assume that the burst temperature of rupture was not appreciably affected by outer surface oxidation

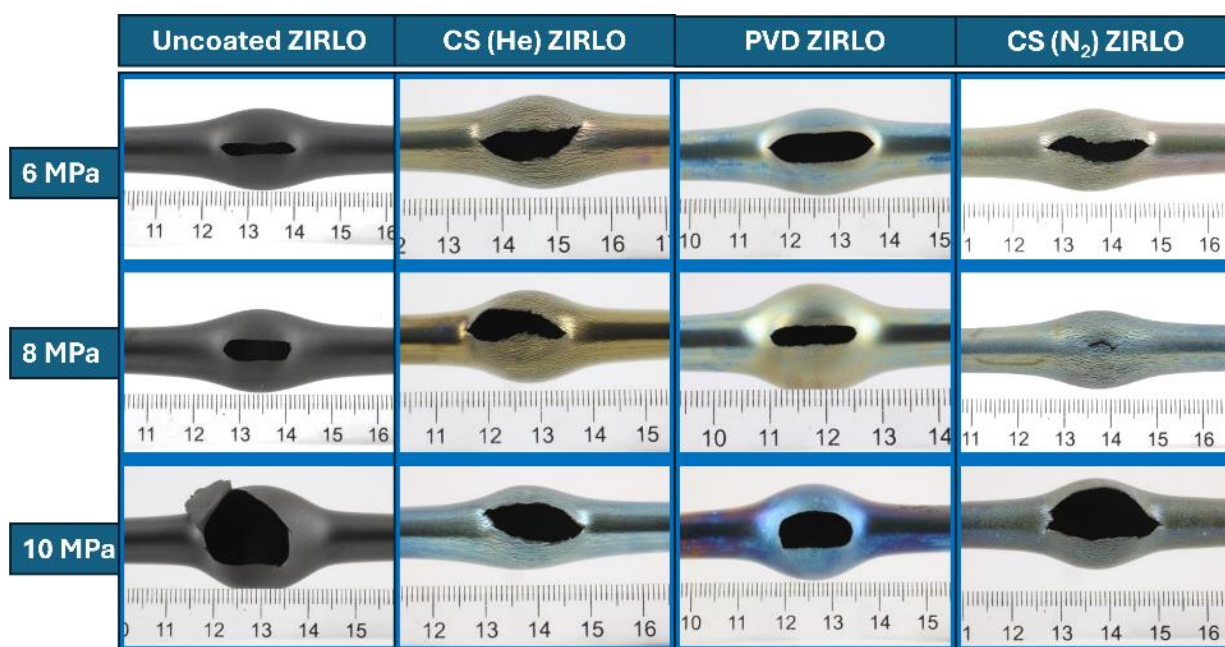


Figure 44. Cladding ruptured with an initial pressure of 6, 8, and 10 MPa of Cr-coated and uncoated Zr-alloy.

Closer examination of the coating surface revealed distinct differences in deformation and cracking behavior. As shown in Figure 45, the Cr-islands on the CS samples are further spaced from each other than in the PVD claddings. While the cracking pattern alone does not explain the difference in burst behavior, measurements of burst area and diametric strain provided an insight into how each Cr-coating constrained the Zr-alloy substrate.

As shown in Figure 46, the total area of each burst opening was measured using the image analysis software ImageJ. The width and length were measured as straight-line distance from one end of the rupture to the other. For primarily symmetric cases this process was straightforward, but more asymmetric rupture the total length of the burst and the widest section along that burst was used. The

area was measured by converting the brightness values of each pixel to a binary mask according to a manually set intensity threshold. The total number of pixels in the rupture was then totaled and converted to  $\text{cm}^2$  using a known pixel/cm ratio.

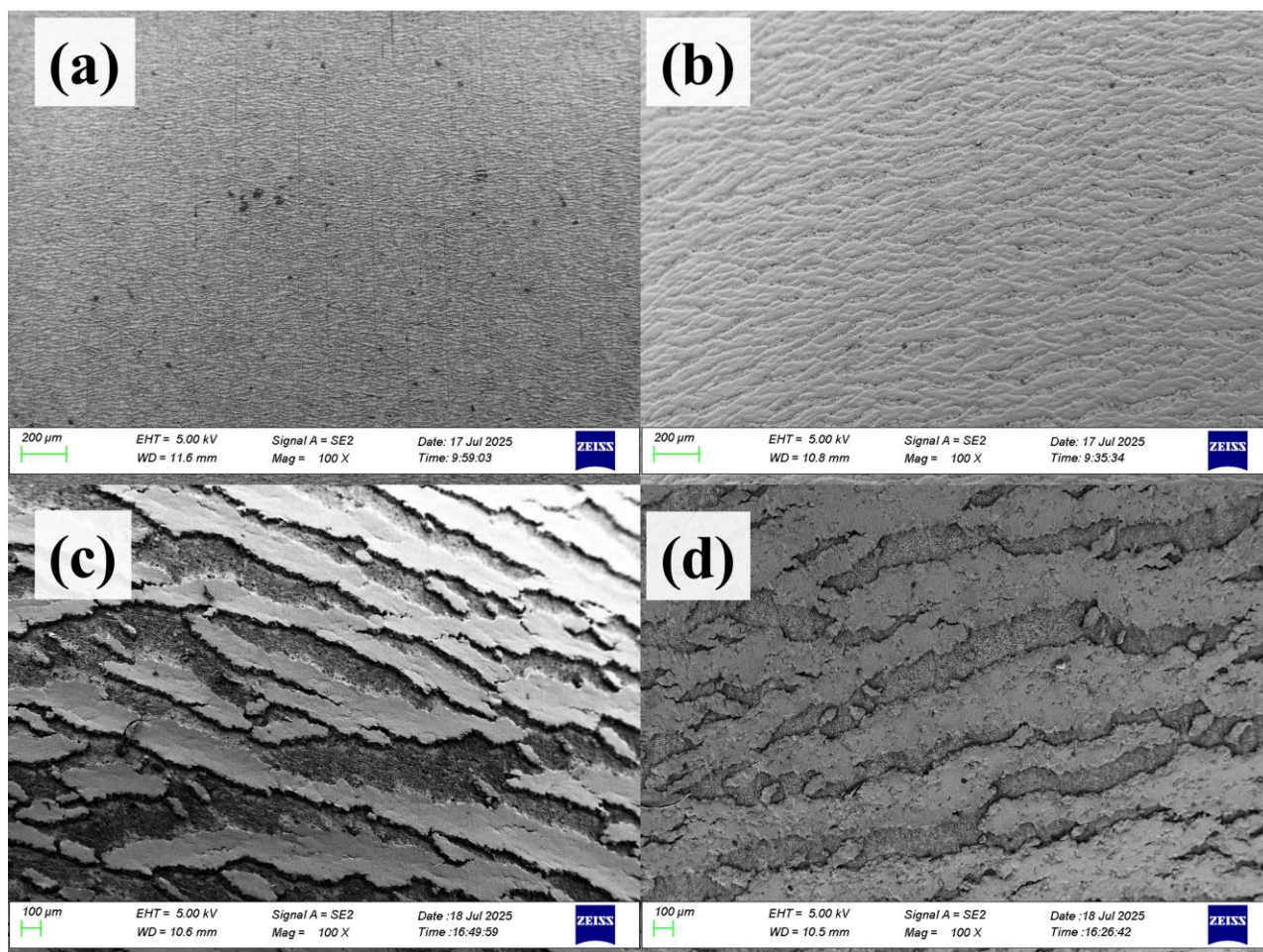


Figure 45. SEM plan-view images of (a) uncoated (b) PVD (c) CS (He) (d) CS (N<sub>2</sub>)

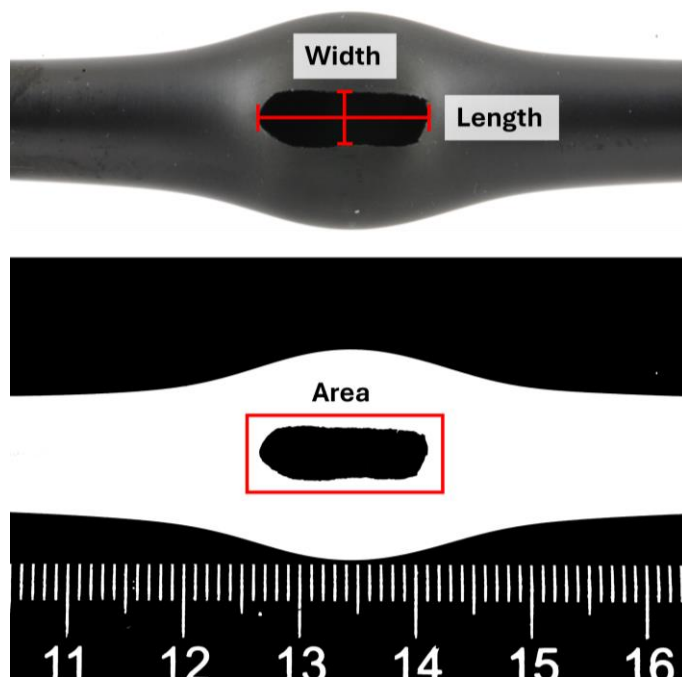


Figure 46. Method used to calculate the burst length, width, and area using ImageJ.

### 3.3.1 Burst Opening and Ballooning Behavior

Analysis of the burst areas for the four types of cladding at the three initial cladding pressures shows interesting behavior in the Cr-coated samples. As shown in Figure 47 at the 45-50 MPa hoop stress range, all Cr-coated samples have a larger burst area than uncoated cladding. This trend begins to reverse in the 60-65 MPa range and fully reverts at the 75-80 MPa range. The burst areas for uncoated cladding rapidly increases with increasing hoop stress.

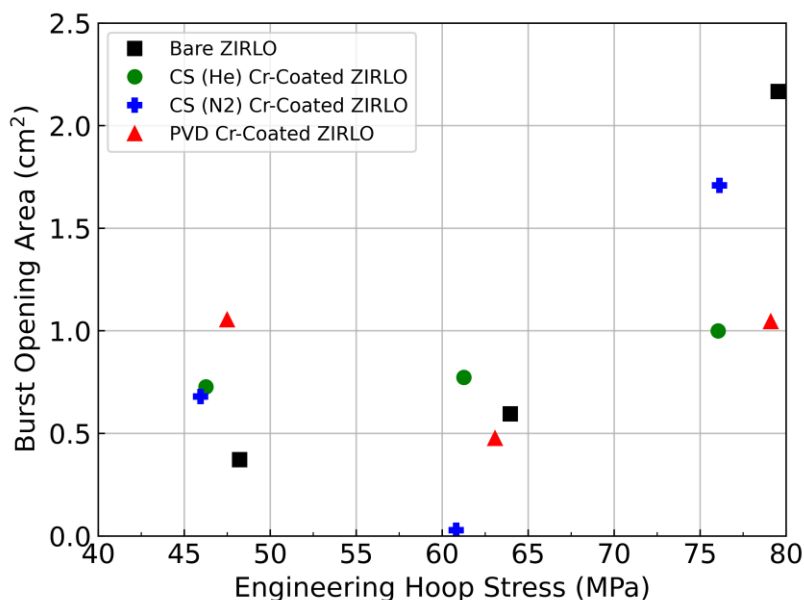


Figure 47. Burst area of uncoated and Cr-coated Zr-alloy.

Diametric strain across the axial length of the cladding was measured using ImageJ image analysis software. Each coating type was analyzed with a single head-on photo. The balloon region was not isolated to only around the burst region. Radial deformation occurred across the entire axial length of uncoated and Cr-coated cladding across all hoop stresses. Comparing the strain profile among the various cladding types revealed that Cr-coatings constrained radial deformation further out from the burst location than in the uncoated case, even though the peak strain at the burst location is similar regardless of coating types except for the CS N<sub>2</sub>, which showed slightly lower strain (Figure 48). Diametric strain of CS (He) and CS (N<sub>2</sub>) reduced by as much as ~13 and 20% compared to the uncoated cladding, respectively, to a distance of 20 mm from the center of the burst. In addition, CS (He) fully constrained Zr-alloy deformation to a distance of 40 mm from the burst center, however the strain of other cladding types did not approach zero until a distance of 80 mm from the burst center. CS (N<sub>2</sub>) also shows a smaller strain compared to the uncoated sample. The low diametric strain is beneficial from the standpoint of restricting the axial fuel relocation, reducing the movable fuel fragments for the dispersal. This will be a benefit of CS Cr-coating in terms of FFRD, which was not observed in PVD Cr-coating showing almost identical diametric strain profile with the uncoated cladding.

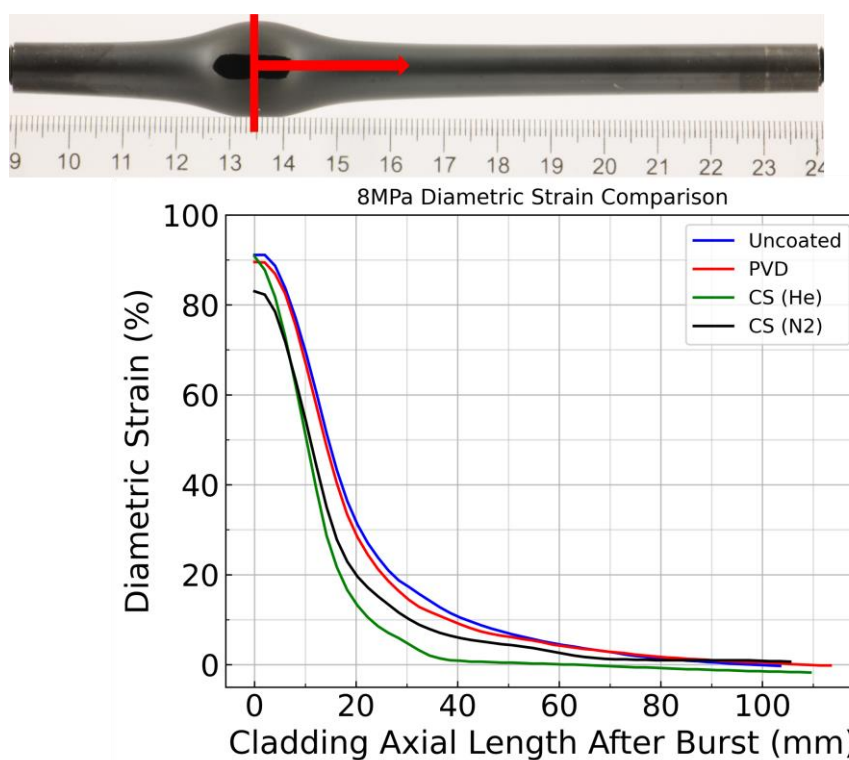


Figure 48. Diametric strain measurements from the 8MPa cladding rupture to the end of the cladding. Strain measurements started at the maximal strain directly in the center of the burst.

### 3.3.2 Wall Thickness Measurement after Burst Tests

In addition to the diametric strain measurements, cross-sections were cut out of the 8 MPa tested cladding sections for uncoated, CS (He), CS (N<sub>2</sub>), and PVD Cr-coated Zr-alloy for wall thickness measurements around the circumference. Radial expansion occurred at majority of burst locations, with some small substrate sections expanding at slower or faster rates due to local non-uniformities in temperature. Anisotropies in deformation were present directly at the burst location in the form of a “flap”, where the pressure was vented out from the cladding and bent the wall outwards as shown in Figure 49 and Figure 50. Different Cr-coatings induced different flap geometries. Uncoated Zr-alloy was symmetrical in its burst opening, maintaining a rectangular burst shape from 6-8 MPa tests and uniform flaps. CS Cr-coated samples exhibited the most asymmetric openings, likely due to the coating

constraining the Zr-substrate until sudden failure. CS (He) yielded a large burst opening and the most protruded flaps of any of the Cr-coated samples.

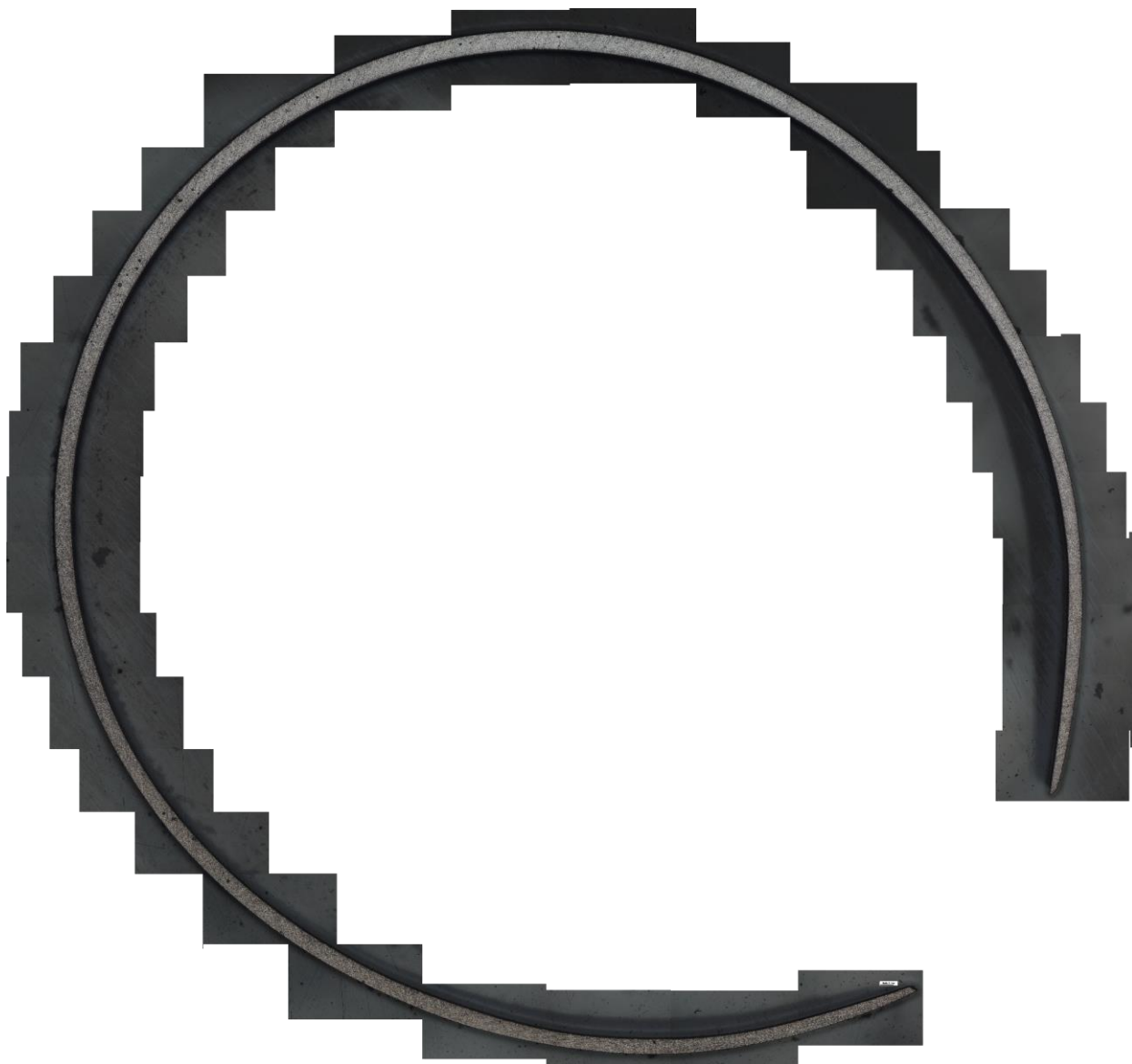


Figure 49. Optical microscopy of a cross section of an uncoated Zr-alloy sample tested at 8 MPa.

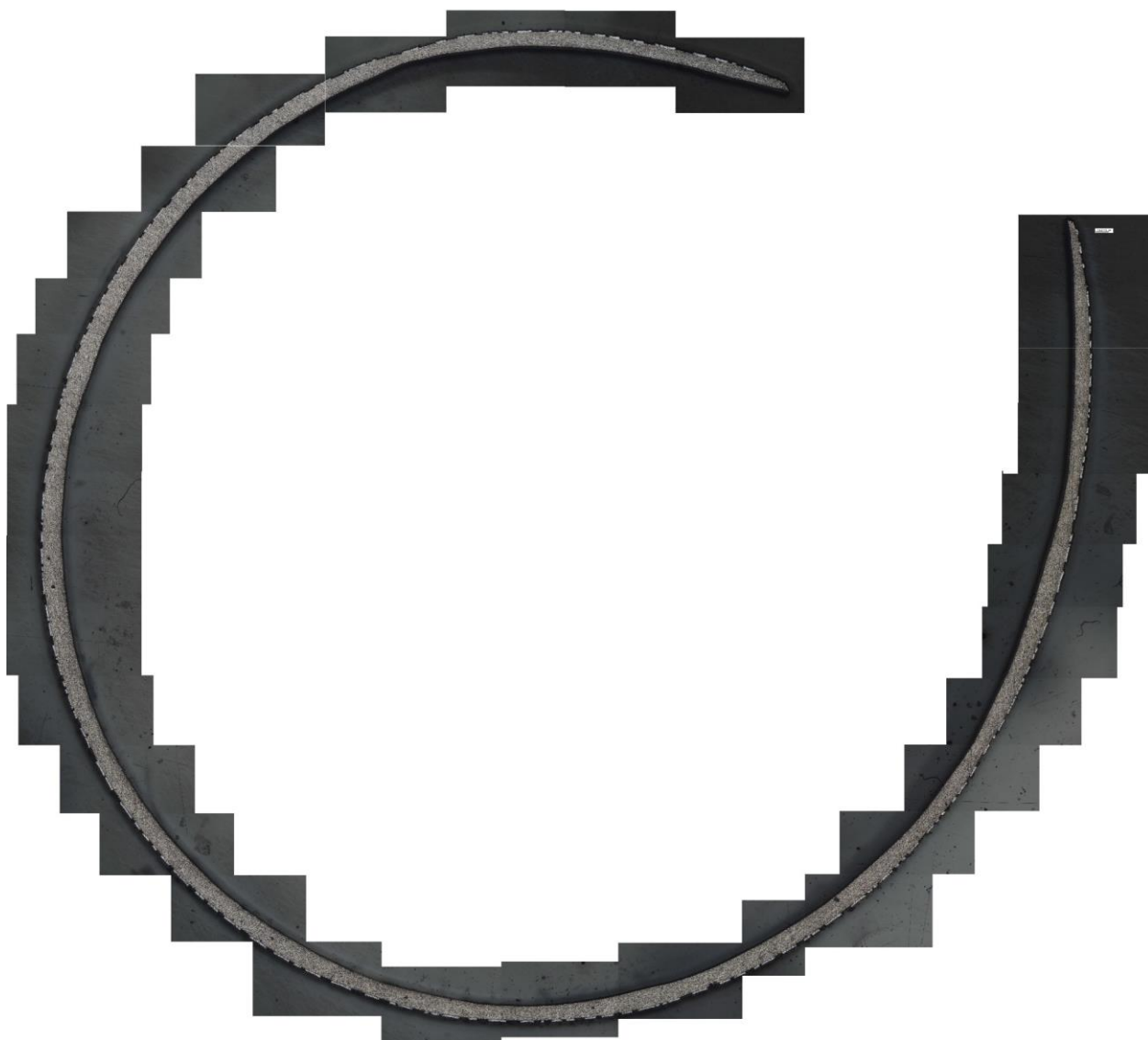


Figure 50. Optical microscopy of a cross section of a CS (He) Cr-coated Zr-alloy sample tested at 8 MPa.

### 3.3.3 Benefits of Cr-coating in the Context of Ballooning and Burst Behavior

CS (He) appeared to perform well as its burst temperature was the highest, diametric strain was the lowest, and the burst area was relatively independent of the initial pressures. This supports the hypothesis that CS Cr-coatings constrain the Zr-cladding substrate, in effect contributing to accident tolerance. Moreover, CS (N<sub>2</sub>) performed similarly while being a more ductile and cost-effective coating. CS (N<sub>2</sub>) also exhibited interesting burst area phenomena (very small burst area at 8 MPa) which likely related to how that coating relieves stress through microfractures at interparticle boundaries. This

information, combined with the examination of surfaces of the coating near the burst regions, suggests that CS (N<sub>2</sub>) would be a better option of the two types of CS coatings. PVD Cr-coated cladding sections showed an enhancement on the burst temperature but did not constrain diametric strain across its axial length, almost matching that of uncoated Zr-alloy. PVD coatings exhibit a characteristic columnar structure which was prone to separation under tension which limits its ability to constrain diametric strain. It exhibited a higher frequency of cracking, possibly leading to a smaller opening as failure was not as sudden as the CS coatings. In addition, interfacial bonding in PVD is derived from atomic mixing at the interface during the early stages of the deposition process. Thus, the PVD coatings may not be strongly adhered to the Zr-alloy substrate to resist radial deformation.

Diametric strain measurements were performed by two methods, ImageJ analysis and circumferential measurements using a string. Figure 48 shows the diametric strain measured at a single camera angle with ImageJ. Cr-coated samples reduced diametric strain across the axial length compared to uncoated Zr-alloy. In particular, CS (He) coating almost fully resisted plastic deformation beyond 40 mm from the burst site. CS (N<sub>2</sub>), being a more ductile coating, constrained deformation after 80 mm from the burst site. PVD Cr-coated and uncoated Zr-alloy were comparable in their deformation along the entire axial lengths of ~110 mm.

## 4 Concluding Remarks

As the high burnup of the nuclear fuel is getting an interest by nuclear industry, the investigation on the FFRD of the high burnup fuel with ATF designs is required. Zr-alloy cladding coated with Cr using cold spray technology with two carrier gases (helium and nitrogen) and using PVD-HiPIMS technology were subjected to LOCA conditions in a single rod reflood and burst test facility designed and built to study the various facets of the development of ATF cladding.

For the reflood tests, uncoated and Cr-coated (CS-He and PVD) Zr-alloy claddings of axial length of 16" were heated to a temperature in the range of 600 to 1200 °C before being quenched by bottom reflooding with subcooled RO water (subcooling: 20 K). At the highest cladding temperature, 1200 °C, the water rapidly oxidized the Zr-alloy, resulting in a thick stoichiometric ZrO<sub>2</sub> layer ~110 μm for uncoated Zr-alloy cladding. Cross-sectional SEM-EDS analysis revealed substantial oxygen diffusion into the cladding wall underneath the oxide layer over ~200 μm. For CS-He Cr-coated Zr-alloy cladding where a 30 μm thick Cr was deposited, a Cr<sub>2</sub>O<sub>3</sub> layer of only 9 μm in thickness formed at 1200 °C, and oxygen diffusion into the cladding was negligible. There was no undercoating oxidation of the Zr-alloy in this case. The absence of oxygen diffusion was further established by microhardness indentation testing across the wall thickness showing no noticeable change in Zr-substrate hardness across the cladding wall thickness, which otherwise would have suggested the formation of hard oxygen-stabilized α-Zr alloy. The relatively thinner ~9 μm PVD Cr-coated Zr-alloy also exhibited similar protective behavior, however SEM-EDS analysis and microhardness testing revealed some oxygen diffusion into the underlying Zr-alloy substrate via the diffusion of oxygen through the PVD Cr-coating's columnar structure. The thin Cr coating was almost entirely consumed by oxidation showing ~1-2 μm of Cr coating layer beneath.

The post-quench ductility of the cladding was examined through RCT tests, and the result of RCT were consistent with the results of oxidation and oxygen diffusion outlined above. The uncoated Zr-alloy, when quenched from 1200 °C, exhibiting brittle behavior and through-wall cracking at vertical displacements as low as 0.25 mm. The thick oxide layer led to a reduction in effective cladding thickness

and contributed to early cladding failure. The Cr-coating was beneficial in improving both post-quench ductility and maximum load before failure due to the aforementioned oxidation resistance of Cr-coating. CS (He) cladding after quenching from 1200 °C yielded a higher maximum load of ~780 N during RCT, while the uncoated cladding's maximum load before failure was only ~220 N. Moreover, the untested samples of the CS (He) Cr-coated cladding reached a similar maximum load as the 1200 °C post-quench sample, suggesting that the CS-He Cr-coating constrains and provides a mechanical reinforcement to the cladding. PVD Cr-coated Zr-alloy showed only a minor improvement in maximum load to failure (~300 N) compared to uncoated Zr-alloy, quenching from 1200 °C.

Uncoated and Cr-coated (CS-He, CS-N<sub>2</sub>, PVD) Zr-alloy claddings were subjected to single rod burst testing at three initial pressures of 6, 8, and 10 MPa. CS (He) and CS (N<sub>2</sub>) All Cr-coatings increased the burst temperature at each of the initial pressures by 20-50 °C. CS (He) provided the highest improvement on burst temperature relative to uncoated Zr-alloy, averaging 49.6 °C higher across all initial pressures. In comparison, CS (N<sub>2</sub>) and PVD averaged 38.0 °C and 38.7 °C increases in burst temperature over the uncoated Zr-alloy, respectively.

After the burst tests, the burst opening size and ballooning profile were characterized. Both these metrics have a profound effect on fuel dispersal into the coolant and relocation in the cladding. As expected, as initial pressure increases, the greater force imparted on the cladding wall would increase burst size. For uncoated Zr-alloy, the burst area increased by a factor of 1.5x as the pressure was increased from 6 and 8 MPa, but by a factor of 4x when the pressure was increased from 8 to 10 MPa. Cr-coated Zr-alloy exhibited a variety of burst opening geometries depending on the Cr deposition method and initial pressure. While there was no discernable pattern in burst opening for the different types of Cr coating, CS (N<sub>2</sub>) Cr coated cladding tested at 8 MPa showed a significantly smaller burst area. The smaller burst size for CS (N<sub>2</sub>) Cr-coated cladding may be attributed to cracks propagating as micro-fractures along interparticle boundaries which promote energy dissipation by a network of smaller cracks than single or a few large cracks, a theory also supported by the examination of the surface of the claddings in the burst region, where a more homogeneous fracture surface is observed for

the CS (N<sub>2</sub>) Cr-coated cladding. The PVD Cr coated cladding showed the most homogeneous coating surface with a large network of very fine cracks. The burst area for the 10 MPa initial pressure for all Cr-coated cladding sections were all lower than for the uncoated Zr-alloy. This suggests that at higher pressures the Cr-coatings may impart a mechanically constraining effect on the deformation of the underlying Zr-alloy substrate.

Characterization of the ballooning behavior by analysis of the diametric strain profiles and cladding wall thickness measurements further demonstrated the constraining effect Cr coating on the deformation of the Zr-alloy. The diametric strain of uncoated Zr-alloy was the largest along the axial length of the cladding, peaking at the center of the rupture. The improvements in performance of cladding imparted by Cr coating were much more pronounced in the diametric strain profiles than in burst area measurements. PVD Cr-coated Zr-alloy had the least constraint on the Zr-alloy cladding, nearly matching the strain of uncoated Zr-alloy along the cladding length. Both CS (He) and CS (N<sub>2</sub>) Cr coatings imparted more notable constraint to the ballooning of the underlying cladding further away from the burst center. The diametric strain of the CS (He) Cr coated cladding dropped to zero just 40 mm away from the rupture site, which is almost half of what was with uncoated cladding (~ 80 mm to drop to zero), CS (N<sub>2</sub>), and PVD Cr-coated cladding. Furthermore, the cladding wall thickness measurements of the CS (He) 8 MPa sample revealed large variation in wall thickness compared to the relatively smooth deformation profile of uncoated Zr-alloy, indicative of both constraint that it exerts on the deformation of Zr-alloy cladding substrate and forced brittle failure of the coating in localized regions. For the case of CS (N<sub>2</sub>) the coatings failed in a more uniform and ductile manner. The enhancement of the ballooning and burst behavior of the Cr-coated, especially by cold spray technology, cladding indicates the reduced risk of the FFRD using the ATF cladding designs even with the higher burn up limit. The decrease in the diametric strain can result in the reduced fuel relocation with the less chance of bursting due to the hot spot effect and with less mobile fuel fragments after the burst. The extremely small burst opening observed in 8MPa CS (N<sub>2</sub>) shows a potential benefit of the Cr-coating minimizing the burst opening itself, but further investigation will be conducted to confirm the benefit.



## References

- [1] N. Belyakov, "Modern Nuclear Power Plant," in *Sustainable Power Generation*, Elsevier, 2019, pp. 291-325.
- [2] C. Azevedo, "Selection of fuel cladding material for nuclear fission reactors," *Engineering Failure Analysis*, vol. 18, no. 8, pp. 1943-1962, 2011.
- [3] A. Oizumi, H. Akie, N. Iwamoto and T. Kugo, "Evaluation of neutron economical effect of new cladding materials in light water reactors," *Journal of Nuclear Science and Technology*, vol. 51, no. 1, pp. 77-90, 2014.
- [4] I. G. Ritchie and A. Atrens, "The diffusion of oxygen in alpha-zirconium," *Journal of Nuclear Materials*, vol. 67, no. 3, pp. 254-264, 1977.
- [5] T. R. Allen, R. Konings and A. Motta, "Corrosion of Zirconium Alloys," in *Comprehensive Nuclear Materials*, Elsevier, 2012, pp. 49-68.
- [6] C. Lemaignan and A. T. Motta, "Zirconium Alloys in Nuclear Applications," in *Materials Science and Technology*, Wiley, 2006.
- [7] M. Steinbrück, "Oxidation of Zirconium Alloys in Oxygen at High Temperatures up to 1600 °C," *Oxidation of Metals*, vol. 70, no. 5-6, pp. 317-329, 2008.
- [8] R. Krishnan and M. K. Asundi, "Zirconium alloys in nuclear technology," *Proceedings of the Indian Academy of Sciences Section C: Engineering Sciences*, vol. 4, no. 1, pp. 41-56, 1981.
- [9] A. M. Garde, R. J. Comstock, G. Pan, R. Baranwal, L. Hallstadius, T. Cook and F. Carrera, "Advanced Zirconium Alloy for PWR Application," *Journal of ASTM International*, vol. 7, no. 9, 2010.
- [10] M. Holt, R. J. Campbell and M. B. Nikitin, "Fukushima Nuclear Disaster," Congressional Research Service, 2012.
- [11] C. McCombie and M. Jefferson, "Renewable and nuclear electricity: Comparison of environmental impacts," *Energy Policy*, vol. 96, pp. 758-769, 2016.
- [12] P. Rudling, R. Adamson, B. Cox, F. Garzatolli and A. Strasser, "High Burnup Fuel Issues," *Nuclear Engineering and Technology*, vol. 40, no. 1, pp. 1-8, 2008.
- [13] OECD, Nuclear Fuel Safety Criteria Technical Review (Second Edition), OECD Publishing, 2012.

- [14] EPRI, "Scoping Calculation of the Impact of Increased Burnup Limits on Spent Fuel Pool Inventory Management," EPRI, 2023.
- [15] U.S.N.R.C, "Higher Burnup," U.S.N.R.C, June 2023. [Online]. Available: <https://www.nrc.gov/reactors/power/atf/technologies/burnup>. [Accessed November 2025].
- [16] M. Bales, A. Chung, J. Corson and L. Kyriazidis, "Interpretation of Research on Fuel Fragmentation, Relocation, and Dispersal at High Burnup," United States Nuclear Regulatory Commission, 2021.
- [17] U.S.N.R.C, *EVALUATION OF FUEL FRAGMENTATION, RELOCATION AND DISPERSAL UNDER LOSS-OF-COOLANT ACCIDENT (LOCA) CONDITIONS RELATIVE TO THE DRAFT FINAL RULE ON EMERGENCY CORE COOLING SYSTEM PERFORMANCE DURING A LOCA (50.46c)*, 2015.
- [18] K. Terrani, "Accident tolerant fuel cladding development: Promise, status, and challenges," *Journal of Nuclear Materials*, vol. 501, pp. 13-30, 2018.
- [19] K. Field, Y. Yamamoto, B. Pint, M. Gussev and K. Terrani, "Accident Tolerant FeCrAl Fuel Cladding: Current Status Towards Commercialization," in *Proceedings of the 18th International Conference on Environmental Degradation of Materials in Nuclear Power Systems – Water Reactors*, Cham, Springer International Publishing, 2019, pp. 1381-1389.
- [20] H. Pham, M. Kurata and M. Steinbrueck, "Steam Oxidation of Silicon Carbide at High Temperatures for the Application as Accident Tolerant Fuel Cladding, an Overview," *Thermo*, vol. 1, no. 2, pp. 151-167, 2021.
- [21] U.S.NRC, *Supplemental Guidance Regarding the Chromium-Coated Zirconium Alloy Fuel Cladding Accident Tolerant Fuel Concept*, U.S.NRC, 2020.
- [22] K. Kane, S. Bell, N. Capps, B. Garrison, K. Shapovalov, G. Jacobsen, C. Deck, T. Graening, T. Koyanagi and C. Massey, "The response of accident tolerant fuel cladding to LOCA burst testing: A comparative study of leading concepts," *Journal of Nuclear Materials*, vol. 574, p. 154152, 2023.
- [23] S. Bell, T. Graening, A. Evans, P. Kelly, B. Pint and K. Kane, "Burst and oxidation behavior of Cr-coated Zirlo during simulated LOCA testing," *Journal of Nuclear Materials*, vol. 564, p. 153679, 2022.
- [24] N. Capps, C. Jensen, F. Cappia, J. Harp, K. Terrani, N. Woolstenhulme and D. Wachs, "A Critical Review of High Burnup Fuel Fragmentation, Relocation, and Dispersal under Loss-Of-Coolant Accident Conditions," *Journal of Nuclear Materials*, vol. 546, p. 152750, 2021.

- [25] A. Yamauchi, "Study on the relationship between fuel fragmentation during a LOCA and pellet microstructure," *Journal of Nuclear Science and Technology*, vol. 58, no. 12, pp. 1330-1342, 2021.
- [26] L. O. Jernkvist and A. Massih, "Models for axial relocation of fragmented and pulverized fuel pellets," *Strålsäkerhetsmyndigheten (SSM)*, 2015.
- [27] R. Montgomery and R. Morris, "Sister Rod Destructive Examinations (FY20) Appendix C: Rod internal Pressure, void volume, and gas transmission tests," 2020.
- [28] T. K. Sawarn, S. Banerjee, K. Pandit and S. Anantharaman, "Study of clad ballooning and rupture behavior of fuel pins of Indian PHWR under simulated LOCA condition," *Nuclear Engineering and Design*, vol. 280, pp. 501-510, 2014.
- [29] Z. Duan, B. Yuan, Q. Wen and K. Chen, "Preliminary Investigation on Burst Behaviors of Zr-Based Cladding Under Simulated LOCA Conditions," in *2024 31st International Conference on Nuclear Engineering*, 2024.
- [30] U.S Nuclear Regulatory Commission, "Cladding, swelling, and rupture models for LOCA analysis," *NUREG-0630*, 1980.
- [31] W. H. Jung, C. Dunbar, N. Fox, T. Demo, M. Corradini, K. Sridharan and H. Yeom, "Quenching behavior of high temperature Cr-coated Zr-alloy cladding during bottom reflood condition," *International Journal of Heat and Mass Transfer*, vol. 232, p. 125942, 2024.
- [32] C. Grandjean, "A STATE-OF-THE-ART REVIEW OF PAST PROGRAMS DEVOTED TO FUEL BEHAVIOR UNDER LOCA CONDITIONS Part One. Clad Swelling and Rupture Assembly Flow Blockage," *ISRN*, 2005.
- [33] R. Reis and A. T. e. Silva, "ANALYSIS OF THE BEHAVIOR UNDER IRRADIATION OF HIGH BURNUP NUCLEAR FUELS WITH THE COMPUTER PROGRAMS FRAPCON AND FRAPTRAN," in *International Nuclear Atlantic Conference*, Belo Horizonte, 2017.
- [34] K. Dongju and L. Youho, "Development and Validation of Cr Diffusion Model for Coated Zircaloy Accident Tolerant Fuel Cladding," in *Korean Physical Society Spring Meeting*, 2022.
- [35] X. Li, Y. Lie, Y. Cui, J. Zhang and J. Fu, "Mechanical property and cracking mechanism of Cr-coated Zr alloy under tensile and compressive loading," *Materials Today Communications*, vol. 41, p. 110422, 2024.
- [36] M. Ho, E. Obbard, P. A. Burr and G. Yeoh, "A Review on the Development of Nuclear Power Reactors," *Energy Procedia*, vol. 160, pp. 459-466, 2019.

- [37] H. Bairiot and J. Vliet, "Behavior of Fuel Cladding Under Accident Conditions," *Cladding Interaction*, p. 189, 1985.
- [38] A. T. Motta, A. Couet and R. J. Comstock, "Corrosion of Zirconium Alloys Used for Nuclear Fuel Cladding," *Annual Review of Materials Research*, vol. 45, no. 1, pp. 311-343, 2015.
- [39] A. Zielinski and S. Sobieszczyk, "Hydrogen-enhanced degradation and oxide effects in zirconium alloys for nuclear applications," *International Journal of Hydrogen Energy*, vol. 36, no. 14, pp. 8619-8629, 2011.
- [40] Y. Guanjie, Š. Martin, C. David, P. Dula, R. Robert and L. Dong, "Investigation of the temperature-dependent failure processes in PVD Cr-coated ZIRLO nuclear fuel cladding using in situ X-ray micro-tomography imaging," *Surface and Coatings Technology*, vol. 512, p. 132376, 2025.
- [41] "Zirconium alloys in nuclear technology," *Proceedings of the Indian Academy of Sciences Section C: Engineering Sciences*, vol. 4, no. 1, pp. 41-56, 1981.
- [42] INTERNATIONAL ATOMIC ENERGY AGENCY, Safety and Performance Aspects in the Development and Qualification of High Burnup Nuclear Fuels for Water Cooled Reactors, INTERNATIONAL ATOMIC ENERGY AGENCY, 2024.